

# Towards Accurate and Robust Modelling of Fluid-Driven Fracture

by

Andre Macieira Braga Costa

Department of Mechanical Engineering and Materials Science  
Duke University

Date: \_\_\_\_\_

Approved:

---

John Dolbow, Advisor

---

Manolis Veveakis

---

Wilkins Aquino

---

New Member

Dissertation submitted in partial fulfillment of the requirements for the degree of  
Doctor of Philosophy in the Department of Mechanical Engineering and Materials  
Science  
in the Graduate School of Duke University  
2023

## ABSTRACT

### Towards Accurate and Robust Modelling of Fluid-Driven Fracture

by

Andre Macieira Braga Costa

Department of Mechanical Engineering and Materials Science  
Duke University

Date: \_\_\_\_\_

Approved:

---

John Dolbow, Advisor

---

Manolis Veveakis

---

Wilkins Aquino

---

New Member

An abstract of a dissertation submitted in partial fulfillment of the requirements for  
the degree of Doctor of Philosophy in the Department of Mechanical Engineering  
and Materials Science  
in the Graduate School of Duke University  
2023

Copyright © 2023 by Andre Macieira Braga Costa  
All rights reserved

# Abstract

Example text

The research presented in this dissertation aims at addressing the aforementioned challenges. A variational framework is proposed to describe fracture in general dissipative solids. In essence, the variational statement is extended to account for large deformation kinematics, inelastic deformation, dissipation mechanisms, dynamic effects, and thermal effects. The proposed variational framework is shown to be consistent with conservations and laws of thermodynamics, and it provides guidance and imposes restrictions on the construction of models for coupled field problems. Within the proposed variational framework, several models are instantiated to address practical engineering problems. A brittle and quasi-brittle fracture model is used to investigate fracture evolution in polycrystalline materials; a cohesive fracture model is applied to revisit soil desiccation; a novel ductile fracture model is proposed and successfully applied to simulate some challenging benchmark problems; and a creep fracture model is developed to simulate the spallation of oxide scale on high temperature heat exchangers.

# Contents

<b>Abstract</b>	<b>iv</b>
<b>List of Tables</b>	<b>viii</b>
<b>List of Figures</b>	<b>ix</b>
<b>Acknowledgements</b>	<b>xii</b>
<b>1 Introduction</b>	<b>1</b>
1.1 Motivation . . . . .	1
1.2 Background . . . . .	3
1.3 Research contributions . . . . .	6
1.4 Organization of the dissertation . . . . .	8
1.5 Notation . . . . .	9
<b>2 Revisiting the Pressure Loading of Phase-Field Fractures</b>	<b>10</b>
2.1 Introduction . . . . .	10
2.2 Model . . . . .	13
2.2.1 Quasi-static derivation . . . . .	13
2.2.2 Derivation using the maximum dissipation principle . . . . .	20
2.2.3 Constitutive choices of the phase-field formulation . . . . .	23
2.3 A J-Integral for pressurized cracks in a phase-field setting . . . . .	25
2.4 Finite Element Implementation . . . . .	30
2.5 Results . . . . .	33

2.5.1	Uniaxial bar under traction in a pressurized environment . . . . .	34
2.5.2	Crack nucleation from a pressurized hole . . . . .	37
2.5.3	Stable propagation of a pre-existing crack . . . . .	40
2.6	Concluding Remarks . . . . .	45
2.7	Acknowledgments . . . . .	45
2.8	Equivalence to SIF condition . . . . .	46
<b>3</b>	<b>A Multi-Resolution Approach for Hydraulic Fracture Simulation</b>	<b>51</b>
3.1	Introduction . . . . .	51
3.2	Model formulation . . . . .	55
3.2.1	Governing equations for hydraulic fracture . . . . .	55
3.2.2	The phase-field method for fracture . . . . .	60
3.3	Multi-resolution method . . . . .	63
3.3.1	General overview . . . . .	63
3.3.2	Global problem discretization . . . . .	65
3.3.3	Local problem initialization . . . . .	66
3.3.4	Local problem discretization . . . . .	69
3.3.5	Crack propagation: translating local damage updates into global crack extensions . . . . .	71
3.3.6	Algorithm summary . . . . .	74
3.4	Numerical Results . . . . .	76
3.4.1	KGD problems . . . . .	76
3.4.2	Poroelastic problem with coupled matrix-fracture flow . . . . .	84
3.4.3	Propagation around an inclusion . . . . .	89
3.5	Summary and conclusions . . . . .	92
<b>4</b>	<b>Extending the Multi-Resolution Approach to Three Dimensions</b>	<b>94</b>
4.1	Introduction . . . . .	94

4.2	Theory . . . . .	98
4.3	Verification . . . . .	98
	<b>Bibliography</b>	<b>99</b>
	<b>Biography</b>	<b>114</b>

# List of Tables

2.1	Material properties for uniaxial bar . . . . .	35
2.2	Material properties, geometric parameters and applied loads for crack initiation problem . . . . .	38
2.3	Parameters used for pressurized crack propagation problem . . . . .	42
2.4	Absolute error in $J$ vs. $G_c^{eff}$ for the pressurized crack propagation problem, as a function of regularization length. . . . .	44
3.1	Material properties and problem parameters for the toughness-dominated KGD problem . . . . .	78
3.2	Effect of subdomain size on the relative error in the crack length. . .	81
3.3	Material properties and problem parameters for the viscosity-dominated KGD problem . . . . .	82
3.4	Material properties for poroelastic problem . . . . .	86
3.5	Problem settings . . . . .	86
3.6	Material properties for inclusion problem . . . . .	90
3.7	Problem settings . . . . .	90

# List of Figures

2.1	Generic body containing cracks loaded in pressure. . . . .	14
2.2	(a) Unloaded virtual crack. (b) Pressure loaded virtual crack; . . . . .	17
2.3	(a) The contour paths $\zeta_{in}$ and $\zeta_{out}$ and subdomain $\Lambda$ , in the vicinity of a regularized crack.; (b) Color contour plot indicating the assumed variation in the function $q$ . . . . .	27
2.4	Uniaxial cohesive bar. . . . .	34
2.5	Traction-separation curves for pressurized uniaxial cohesive bar problem, obtained with various phase-field models: (a) (LVC) with linear indicator function; (b) (LVC) with quadratic indicator function; (c) (LVC) with $2d - d^2$ indicator function; and (d) Proposed approach (UVC) with linear indicator function. . . . .	36
2.6	(a) Problem schematic; (b) Mesh used in the computations, exploiting symmetry. . . . .	38
2.7	(a) Final crack pattern using proposed model; (b) Damage field using the model from [1]. . . . .	40
2.8	(a) Geometry and boundary conditions for pressurized crack propagation problem; (b) J-Integral domain function $q$ . . . . .	41
2.9	Reference results with the LVC formulation. Curves with $\ell = a/160$ are not shown, as they are almost identical to the ones with $\ell = a/80$ . (a) $I(d) = d$ ; (b) $I(d) = d^2$ ; (c) $I(d) = 2d - d^2$ . . . . .	43
2.10	Results with the proposed formulation (UVC) (a) $I(d) = d$ ; (b) $I(d) = d^2$ ; (c) $I(d) = 2d - d^2$ . . . . .	43
2.11	Convergence of the proposed formulation with $I(d) = d$ . . . . .	44
3.1	Schematic of a poroelastic rock with a fracture, inspired by [? ]. . . . .	56

3.2	Global domain $\Omega$ on the left and local domain $\Omega_L$ on the right. The surface corresponding to the local domain boundary $\partial\Omega_L$ is indicated within the global domain with the dashed red lines. The local domain is magnified to highlight the phase-field representation of the global crack $\Gamma$ . . . . .	63
3.3	Global domain $\Omega$ on the left and local domain $\Omega_L$ on the right. The nodes in the subset $\mathcal{K}$ , where $d$ is set to 1 are colored in yellow. . . . .	67
3.4	Illustration of global cells (in gray) in the neighborhood of a local element, indicated in pink. The matrix pressure at a quadrature point in the local element is calculated using an average of global pressures from neighboring cells $\{i\}$ , with weights corresponding to the distances $r_i$ between the quadrature point and the cell center. . . . .	68
3.5	(a): Illustration of the global crack tip and global tip element. (b) Case when the local tip falls inside the tip element. (c) Case when the local tip falls outside the tip element. . . . .	72
3.6	(a): Construction of the segment connecting global and local tips. (b) New crack segment to be added. (c) Update of the global crack tip and global tip element. . . . .	73
3.7	Multi-resolution solution algorithm. . . . .	76
3.8	(a) Schematic of the KGD problem, inspired by [2]. (b) Computational domain for the KGD problem (not to scale). . . . .	77
3.9	Comparison of numerical results and analytical solution for the toughness-dominated KGD problem: (a) crack length vs. time and (b) pressure vs. time. . . . .	80
3.10	Study of the effects of subdomain size on the results of the toughness-dominated KGD problem: (a) influence on predicted crack length and (b) predicted pressure. . . . .	81
3.11	Numerical results and analytical solution for the viscosity-dominated KGD problem: (a) crack length vs. time; and (b) inlet pressure vs. time. . . . .	84
3.12	Geometry and notation for the coupled poroelastic-fracture problem.	85

3.13 Results from the fully coupled poroelastic-fracture problem for the multi-resolution method (with and without driving pressures) and a standard phase-field model: (a) crack size over time, (b) inlet pressure. The time for crack propagation ( $t_{ref}$ ) in the phase-field model and the corresponding inlet pressure ( $p_{ref}$ ) are used as references for the dimensionless charts above. . . . .	87
3.14 Fields from the coupled poroelastic-fracture problem, taken at the end of the simulation, contrasting results from the multi-resolution scheme without the driving pressures (top row) to those obtained using a standard phase-field model of fracture in poroelastic media (bottom row). (a) Contour plots of the damage field. (b) Contour plots of the pressure field. . . . .	88
3.15 Geometry for the inclusion problem. . . . .	89
3.16 Crack paths for the inclusion problem: (a) 2X stiffer inclusion; (b) 7X stiffer inclusion; and (c) 15X stiffer inclusion. . . . .	91
3.17 Inlet pressure as a function of time for the three inclusion problems, corresponding to inclusions with different stiffnesses. The reference values of the pressure $p_{ref}$ and time $t_{ref}$ were defined as the minimum pressure that led to fracture growth and the associated time, considering the simulated injection rate. . . . .	92

# Acknowledgements

I want to thank Professor Philip Bayly, my undergraduate advisor, for his patient guidance in my first research project. I want to thank Professor John Dolbow, my advisor, for his valuable advice, barbecues and Thanksgiving dinners, and for proofreading several poorly written drafts of mine. I want to thank Dr. Benjamin Spencer, my technical advisor at Idaho National Laboratory, and Dr. Wen Jiang for two great summer internship experiences at INL, many helpful conversations, and their time reviewing my pull requests. I want to thank Professors Wilkins Aquino, Johann Guilleminot, Manolis Veveakis for their time and service as my committee members. Most of the work in this dissertation originated from their course projects. I want to thank Dr. Brandon Talamini, Dr. Andrew Stershic, and Dr. Michael Tupek from the Sandia National Laboratories for many enlightening discussions. I want to thank my colleagues Dr. Yingjie Liu and Dr. Rudy Geelen for babysitting me during my first semesters as a graduate student. I want to thank the Dolbow family for their sweet potato pie recipe which helped me navigate through some difficult times during the pandemic. Finally, I am most thankful for my wife Peiyi and my puppy Rudy.

# 1

## Introduction

### 1.1 Motivation

Hydraulic fracturing, commonly known as fracking, is a complex process that involves the initiation and/or propagation of fractures resulting from the application of hydraulic pressure by pressurized fluid. This technique finds extensive applications, particularly in the field of geology. [CITE ADACHI]

In the realm of oil and gas production, fracking is used to stimulate tight shale reservoirs, creating pathways for the extraction of shale gas. Since the pioneering field test at the Hugoton field in 1947, advancements in fracking technology, such as multi-stage hydraulic fracturing and horizontal drilling, have significantly enhanced productivity in these reservoirs. In fact, recent data from the US Energy Information Administration reveals that a significant portion, around 66% of oil and 80% of gas, produced in the United States comes from wells that undergo hydraulic fracturing.

Hydraulic fracturing also plays a crucial role in geothermal energy, which offers a promising avenue for generating renewable, carbon-free electricity. However, geothermal systems face challenges due to the low permeability of most suitable hot rock formations, which limits the productivity of these systems in their natural state. By

employing hydraulic fracturing techniques, the permeability, and consequently the efficiency of geothermal systems can be improved. These specially treated systems are commonly referred to as Enhanced Geothermal Systems (EGS). Advances in fracking science and technology are thus one of the key steps towards making EGS a viable and reliable clean energy source.

Another significant geological process that addresses the global CO<sub>2</sub> problem is Carbon Storage and Sequestration, where CO<sub>2</sub> is injected and trapped in tight rock formations deep beneath the surface, preventing its release into the atmosphere. In the context of CO<sub>2</sub> sequestration, caprock fracturing, which can happen during injection or through long-term thermo-chemo-mechanical processes may lead to CO<sub>2</sub> leakage. This consists thus of case where, in contrast of the previous ones, hydraulic fracture must be prevented.

Hydraulic fracturing also finds applications in various other fields, including the disposal of waste drill cuttings underground [5 - adachi], measurement of in situ stresses [108,9 - adachi], goafing and fault reactivation in mining operations[7,8 - adachi], and stimulation of groundwater wells (Banks et al., 1996; Less and Andersen, 1994 - heider).

Hydraulic fracturing, despite its significant economic benefits, has raised concerns among critics regarding potential seismic events, especially in the context of O&G and EGS applications. Additionally, objections center around the environmental impact, including air and noise pollution, as well as the risk of groundwater and surface water contamination when chemicals are introduced into the injection fluids.

Given the importance of these applications and the associated risks, it is evident that a comprehensive understanding of fracture processes is crucial for the well-being of our planet and society. However, obtaining sufficient experimental data for deep subsurface processes is challenging due to the depths involved and the difficulty in replicating true rock conditions in laboratory experiments. Consequently, there

has been a growing focus on computational modeling and simulation of fluid-driven fractures. These computational approaches provide a cost-effective means to gain insights into the intricate physical processes associated with hydraulic fracturing.

## 1.2 Background

In this dissertation, four types of fracture are of interest: brittle fracture, quasi-brittle fracture, cohesive fracture, and ductile fracture. Brittle and quasi-brittle fracture center around the Griffith-type description of fracture, in the sense that the stress field at the crack tip is singular. In particular, brittle fracture is characterized with the complete loss of tensile strength upon crack nucleation. Under displacement-controlled uni-axial tension, a brittle specimen forms a through crack immediately after crack nucleation. Quasi-brittle fracture, in contrast, shows a gradual decay of tensile stress which is often measured in the form of a traction-separation law. Although the celebrated Griffith theory of fracture captures the behavior of a wide range of brittle and quasi-brittle materials, it bears emphasis that most materials are not perfectly brittle in the Griffith sense. Cohesive fracture, for example, describes materials that possess a *fracture process zone* ahead of the crack tip. The fracture process zone (FPZ) is a lumped description of small-scale yielding, void coalescence, and micro-crack merging. Typically, the material inside the FPZ only partially loses its load-carrying capacity, and therefore cohesive fracture also displays a gradual decay of tensile stress after crack initiation. The boundary between the definitions of quasi-brittle fracture and cohesive fracture is inherently vague. In this dissertation, cohesive fracture is assumed to have a substantially larger fracture process zone than quasi-brittle fracture, and at the engineering scale, numerical models for these two types of fracture are often used interchangeably. Lastly, ductile fracture describes the softening due to fracture after a stage of plastic hardening. Most metals and fiber-reinforced cementitious composites are ductile and are subject to ductile failure,

A number of models have been proposed to model fracture. What follows is a brief, non-comprehensive survey of numerical methods to model fracture. Particle-based and mesh-free discretization techniques, such as the discrete element method (DEM), lattice spring methods, and peridynamics, have been developed for fracture simulation. The key advantage of these methods lies in the fact that cracks can nucleate and grow in an unguided manner. However, the computational cost of these methods can be very high and the interface conditions are not straightforward to apply. Within the context of the finite element method (FEM), the most commonly used element techniques to model cracks are the extended finite element method (XFEM) and the cohesive zone method (CZM). Using XFEM, fracture are represented as discrete discontinuities and the solution space with discontinuities are enriched using the partition of unity method [3, 4]. Singularities associated with fracture can be represented using XFEM enrichment at relatively low cost. However, managing the data structure and tracking the evolution of complex fracture surfaces, particularly in 3D, are quite tedious. Using CZM, cracks are modeled by cohesive elements inserted between element boundaries, and softening is governed by a traction-separation law at crack surfaces [5, 6]. For polycrystalline material, it is convenient to use CZM to model intergranular crack initiation and propagation [7, 8]. Nonetheless, CZM suffers from mesh dependency because the representation of crack propagation is restricted to element boundaries.

The variational approach to fracture was proposed by Francfort and Marigo [9], and the phase-field implementation is attributed to Bourdin et al. [10]. Bourdin et al. [11] provides an overview. Pham and Marigo [12] used a crack geometric function that is linear in the phase-field variable, resulting in a purely elastic response prior to crack initiation. This fracture energy functional was subsequently referred to as the **AT-1** functional by Bourdin and co-workers (meant to evoke *Ambrosio* and *Tortorelli*, who initially introduced this and related functionals in the context of

image segmentation [13]). Wu [14] generalized the *Ambrosio-Tortorelli* functional [13] to a family of second-order polynomials with various phase-field profiles, with specific choices of recovering the widely adopted AT-1 and AT-2 models. In the variational approach, crack surfaces are represented by a surface density function in terms of an auxiliary phase field. This naturally gives rise to a regularization involving a length scale parameter. Recent works have illustrated the potential of phase-field models to be predictive for a wide range of fracture problems. Phase-field models for fracture have succeeded in capturing complex crack patterns, including branching and merging in both two and three dimensions [15, 16, 17, 18, 19].

The general variational framework was first proposed by Biot [20] in the context of thermoelasticity, followed by extensive investigations in coupled thermoelastic and thermoviscoelastic systems [21, 22, 23, 24, 25, 26]. Well-defined variational principles for dissipative solids with and without heat conduction also exist [6, 27]. However, the case of thermal-mechanical-fracture coupling in dissipative materials has received far less attention.

It is worth noting that there are fundamental differences between variational consistency and thermodynamic consistency. In fact, thermodynamically consistent models are not necessarily variational (and vice versa). To satisfy thermodynamics, the model *must* satisfy mass conservation, linear momentum conservation, angular momentum conservation, as well as the first and the second laws of thermodynamics. Violating any of the aforementioned conservations or thermodynamic laws results in a physically inadmissible model. However, since the second law of thermodynamics is an inequality statement, there are infinitely many ways to satisfy it when modeling a dissipative solid. In contrast, the variational approach (including, but not limited to, variational approaches to fracture) is based on the idea that, upon careful construction of a potential, its variational statements are thermodynamically consistent, implying that the dissipation attains its maximum at the solution corre-

sponding to the variational statements. In other words, the variational approach sets a more restrictive stage for model construction because it places more constraints on the constitutive behavior of the material. Most notably, if a potential is constructed within the variational framework to account for thermomechanical coupling, the heat generation due to its dissipation is directly predicted by the variational framework and cannot be specified arbitrarily.

The restrictions imposed by the variational approach lead to several beneficial aspects. First, the variational framework enables application of the tools of calculus of variations to the analysis of the solution. In particular, the direct method of calculus of variations informs conditions for the existence and uniqueness of solutions (e.g. [28]). Second, the localization of the fracture and the plastic zone can be studied within the framework of free-discontinuity problems [29, 30]. Third, in numerical methods, discretization of the variational statement of the problem leads to a symmetric operator, which can save storage and potentially accelerate the assembly process. Furthermore, energy-based line search methods can be directly applied to the system of equations; many powerful numerical optimization algorithms within standard linear algebra packages (e.g. PETSc [31], TAO [32], Trilinos [33], and Matlab [34]) can be utilized out-of-the-box; and the time-discretized variational problem leads to robust and efficient variational constitutive update algorithms [6].

### 1.3 Research contributions

This dissertation extends the existing variational framework to account for thermal-mechanical-fracture coupling. The proposed framework is able to account for large deformation, inelastic deformation, thermal effects (i.e. heat conduction, heat convection, and heat generation), viscous effects, and potentially dynamic effects. From a fracture mechanics point of view, the framework is flexible enough to model brittle, quasi-brittle, cohesive, and ductile fracture. The applicability to each type of

fracture is examined in the following chapters: a brittle/quasi-brittle instantiation is applied to model three-dimensional intergranular fracture and fission-gas-induced fragmentation in microstructures; a cohesive fracture model is applied to revisit the soil desiccation problem with a focus on random fracture properties; and a family of ductile fracture models are developed to simulate quasi-static ductile failure under isothermal conditions as well as thermal-induced oxide spallation.

- In Chapter 3, phase-field models for brittle/quasi-brittle fracture are employed to simulate intergranular fracture with multiple bubbles on the grain boundaries in 3D and over-pressurized fission-gas-induced fragmentation at microscale. To account for pressurized crack surfaces, we present an extension of the quasi-brittle model by including regularized external work done by pressure into the total energy of the system. We demonstrate that the prediction of the dependence of the critical fracture strength on porosity based on 3D simulations is better than the 2D prediction. The effects of multi-bubble interaction and partial recrystallization in high-burnup structures are also investigated.
- In Chapter 4, a phase-field model for cohesive fracture is used to simulate pervasive cracking in thin films. A new strain energy split is proposed to enforce frictionless contact conditions in the vicinity of diffuse fracture surfaces. In contrast to existing splits that have been proposed, our approach completely prevents tractions from being transmitted across fully damaged surfaces that are loaded in tension. We construct a probabilistic model for the critical fracture energy and the fracture toughness, modeled as (potentially correlated) random fields, and demonstrate, through forward analysis and by solving an inverse problem, how crack network morphology can be influenced by stochastic spatially varying material properties.
- In ??, we present a variational model for ductile fracture, and demonstrate,

through numerical examples, that the model has the following properties: the elastic-plastic response and the plastic hardening law remains unmodified prior to crack initiation even when the plastic energy is degraded as a function of the phase-field variable; a regularization-length independent critical fracture strength and softening response can be obtained by a family of rational degradation functions; and a novel dual kinetic potential, termed with *the coalescence dissipation*, can be incorporated to introduce an alternative form of coupling between plasticity and fracture. Thermal effects are then incorporated to model spallation of the oxide scale in a high-temperature heat exchanger.

## 1.4 Organization of the dissertation

First, the variational framework is presented in Chapter 2. General kinematics and constraints assumed throughout this dissertation are summarized in ???. ?? provides a brief review of thermodynamic conservations and laws in their global and local forms. The proposed variational framework is presented in ??, and discretization of the governing equations is presented in ??.

The variational framework is applied to solve engineering problems in Chapters 3 and 4 and ???. Chapter 3 simulates intergranular fracture and fission-gas-induced fracture in microstructures. Chapter 4 revisits the soil desiccation problem and explores the effect of random fracture properties. ?? benchmarks the ductile fracture model with a three-point bending experiment and the Sandia Fracture Challenges, and models oxide spallation in high-temperature heat exchangers. Each chapter begins with a general introduction to provide context and an overview of state-of-the-art methods and models. Then, specific constitutive choices are made, and the resulting governing equations are presented. Each chapter concludes with verifications of the variational model and some concrete numerical examples.

## 1.5 Notation

In what follows, deterministic scalar, vectors, second-order tensors, and fourth-order tensors are denoted by  $a$  (or  $A$ ),  $\mathbf{a}$  (or  $\mathbf{A}$ ),  $\mathbf{A}$ , and  $\mathbb{A}$ , respectively.

Let  $\Omega$  be a collection of points  $\mathbf{X} \in \mathbb{R}^d$ ,  $d \in \{1, 2, 3\}$ . Scalar- and vector-valued random fields defined on the probability space  $(\Theta, \Sigma, P)$ , indexed by  $\Omega$ , are denoted as  $\{A(\mathbf{X}), \mathbf{X} \in \Omega\}$  and  $\{\mathbf{A}(\mathbf{X}), \mathbf{X} \in \Omega\}$ , respectively. At any fixed material point  $\mathbf{X} \in \Omega$ ,  $a(\mathbf{X})$  and  $\mathbf{a}(\mathbf{X})$  are random variables defined on the probability space  $(\Theta, \Sigma, P)$ . For any fixed  $\theta \in \Theta$ ,  $a(\theta)$  and  $\mathbf{a}(\theta)$  are realizations of the random variables. Similarly,  $\mathbf{X} \mapsto a(\mathbf{X}; \theta)$  and  $\mathbf{X} \mapsto \mathbf{a}(\mathbf{X}; \theta)$  are realizations of the random fields  $\{A(\mathbf{X}), \mathbf{X} \in \Omega\}$  and  $\{\mathbf{A}(\mathbf{X}), \mathbf{X} \in \Omega\}$ .

Einstein summations are assumed wherever applicable unless otherwise stated. For any vectors  $\mathbf{a}$  and  $\mathbf{b}$  of the same size, the inner product is defined as  $\mathbf{a} \cdot \mathbf{b} = a_i b_i$  where  $a_i$  and  $b_i$  are components of the vectors. The associated vector norm is  $\|\mathbf{a}\|^2 = \mathbf{a} \cdot \mathbf{a}$ . Similarly, for any second-order tensors  $\mathbf{A}$  and  $\mathbf{B}$  of the same size, the inner product is defined as  $\mathbf{A} : \mathbf{B} = \text{tr}(\mathbf{A}^T \mathbf{B})$ . The associated Frobenius norm reads  $\|\mathbf{A}\| = \sqrt{\mathbf{A} : \mathbf{A}}$ . Other matrix norms will be distinguished by subscripts. The outer (cross) product of two vectors is written as  $\mathbf{a} \otimes \mathbf{b} = a_i b_j$ .

The time derivative is denoted by an over-dot, e.g.  $\dot{a}$ . Partial derivative is denoted by a subscript starting with a comma, i.e.  $a_{,bc} \equiv \partial^2 a / \partial b \partial c$ . Macaulay brackets are denoted by triangle brackets  $\langle a \rangle_{\pm}$  and are defined as  $\langle a \rangle_{\pm} \equiv (a \pm |a|)/2$ .

# 2

## Revisiting the Pressure Loading of Phase-Field Fractures

### 2.1 Introduction

The propagation of pressurized fractures is a physical phenomena of interest or concern in many different fields of engineering. Some examples include hydraulic fracture (fracking) treatments in the oil and gas industry [35, 36], pressure vessel rupture [37], fracture in concrete dams [38] and fuel fracture in nuclear reactors [39, 40]. Therefore, predictive simulation tools for this phenomena have been intensively studied in recent years. One of these tools is the phase-field method for fracture [41]. Initially developed for traction-free cracks, the method has since been extended to account for pressure loading on the surfaces of cracks, as in [1, 42, 43, 44, 45]. These various formulations exhibit real differences in terms of their structure and form when it comes to how the pressure loads are incorporated. The objective of this work is to examine the impact of the various choices, and to compare them to a relatively new formulation for pressurized crack surfaces in a phase-field for fracture context [46].

The main contributions of this work are: (a) to show that established formu-

lations for pressure-driven fracture in the phase-field context have limitations when cohesive processes are involved; (b) to demonstrate that the new formulation, derived from variational principles, can address these limitations and be easily combined with phase-field models of cohesive fracture; and (c) to illustrate the advantages and disadvantages of the various models in terms of accuracy in obtaining various quantities of interest.

Phase-field methods for fracture regularize sharp crack representations through the use of a scalar phase or damage field whose evolution is governed by minimization principles. Such methods first appeared, in different forms, in the works of Bourdin et al. [41] and Karma et al. [47]. The model introduced in Bourdin et al. [41] was obtained by a regularization of the variational formulation of fracture developed in Francfort and Marigo [48], using ideas from Ambrosio and Tortorelli [13]. It has been widely adopted in the mechanics community and extended for use in a variety of fracture mechanics problems, such as ductile failure [49, 50, 51, 52, 53], hydraulic fracture [54, 55, 56, 57, 51], dessication problems [58, 59, 60, 61], dynamic fracture[62, 63, 64, 65, 66, 67, 68], fracture in biomaterials [69, 70, 71, 72, 73] and many more. Some recent reviews can be found in [74, 75, 76].

With regard to the use of the phase-field method for hydraulic fracture problems, one challenge concerns how best to incorporate surface loads that result from pressures on crack faces that are diffuse. One approach is to regularize the resulting surface tractions with an approach that is very similar to how the crack surface energy is regularized. Early work along these lines focused on crack surfaces loaded by constant pressures, as in Bourdin et al. [1] and Wheeler et al.[42]. Since these early developments, these models have been extensively used since then for the study of pressurized fractures, for example in [77, 78, 79, 80]. They were also extended and modified to account for fluid flow inside the fractures and poroelasticity in the surrounding medium [51, 56, 55, 54, 57, 81, 82]. The reader is referred to the recent

review by Heider [83] for additional works on phase-field methods for hydraulic fracture. The various models all employ some form of “indicator function” that assists in the regularization of the surface load itself. Despite several different indicator functions being proposed, the implication of the particular choice of indicator on the accuracy of the models has yet to be thoroughly examined.

In this manuscript, a new formulation for the study of pressurized fractures, first proposed in the thesis of Hu [46] is also examined. In particular, it is studied in combination with a cohesive version of the phase-field for fracture method, which was proposed in the recent works of [84, 85, 14]. This facilitates the study of pressurized fracture in quasi-brittle materials and reduces the sensitivity of the effective strength to the regularization length. To ensure that the cohesive fracture behavior is preserved, the implicit traction-separation law is evaluated for a simple one-dimensional problem and shown to be insensitive to the applied pressure with the new formulation. Fracture initiation and propagation examples are also examined to highlight advantages and limitations of the model.

As part of the analysis conducted to evaluate the various formulations, the J-integral is used to verify the extent to which mode-I crack propagation occurs when the energy release rate reaches the critical fracture energy. The contour form of the J-integral and its modifications for some common cases of phase-field fracture has been examined by others, see e.g. the work of [86], [87] and [88]. In the case of pressurized cracks, the contour version of the J-integral is not path independent. Many prior works have focused on developing domain forms of the J-integral for sharp cracks that are domain independent [89, 90]. In this work, a domain form of the J-integral that is suitable for pressurized phase-field cracks is developed for the first time.

The paper is organized as follows. In Section 2.2, a simple model for pressure-induced fracturing is presented and the new phase-field formulation is derived in

two different ways. Section 2.3 provides the derivation of the domain form of the J-Integral for pressurized phase-field cracks. In Section 2.4, the discretization scheme using finite elements is presented. Then, in Section 2.5 some fundamental examples involving crack nucleation and propagation are used to illustrate the performance of the various models and choices of indicator functions. Finally, some concluding remarks and directions for future work are discussed in the last section.

## 2.2 Model

The formulation for treating pressurized cracks in a phase-field setting, first introduced by Hu [46], can be derived in two different ways. In what follows, it is first derived based on energy minimization in quasi-static conditions in subsection 2.2.1. This illustrates the main difference in the underlying hypothesis for this new model compared to the widely used formulations of [1] and [43], for example. A second derivation based on a maximum dissipation principle is then provided in subsection 2.2.2.

The following assumptions are invoked for both derivations. A linear elastic body  $\Omega \in \mathbb{R}^n$  ( $n = 2$  or  $3$ ), containing cracks denoted by  $\Gamma$  is considered (Figure 2.1). The boundary  $\partial\Omega$  is partitioned as  $\partial\Omega = \partial\Omega_D \cup \partial\Omega_N$ , where  $\partial\Omega_D$  represents the portion of the boundary where displacements are prescribed and  $\partial\Omega_N$  the portion where tractions are applied. Deformations and rotations are assumed to be small, so that a small-strain formulation is appropriate. For simplicity, body forces are neglected.

### 2.2.1 Quasi-static derivation

The quasi-static derivation of the formulation begins by considering the potential energy of a body with cracks which are internally loaded with a pressure  $p$ . Crack propagation is associated with a critical fracture energy density,  $G_c$ . The total po-

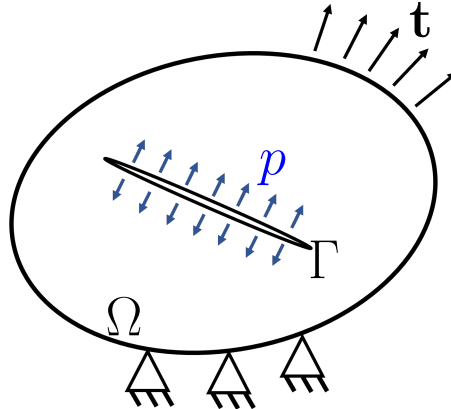


FIGURE 2.1. Generic body containing cracks loaded in pressure.

tential energy is given by

$$U(\boldsymbol{\epsilon}(\mathbf{u})) = \int_{\Omega} \psi_e(\boldsymbol{\epsilon}(\mathbf{u})) \, dV + \int_{\Gamma} G_c \, dA - \int_{\Gamma} p \mathbf{n} \cdot \mathbf{u} \, dA - \int_{\partial\Omega_N} \mathbf{t} \cdot \mathbf{u} \, dA, \quad (2.1)$$

in which  $\mathbf{u}$  are the displacements,  $\boldsymbol{\epsilon}(\mathbf{u}) = \nabla^s \mathbf{u}$  denotes the infinitesimal strain,  $\psi_e$  the strain energy density,  $\mathbf{t}$  the externally applied tractions and  $\mathbf{n}$  the unit normals of the crack set  $\Gamma$  (oriented outwards from  $\Omega$ ).

In a phase-field for fracture setting, the crack surface  $\Gamma$  is regularized with the aid of a scalar phase (or damage) field  $d(\mathbf{x}) \in [0, 1]$ . In this work,  $d = 0$  represents intact material (away from the crack surface) and  $d = 1$  fully-damaged material (inside the crack). The damage field is employed in the approximation of the surface integrals in (2.1) as volume integrals. For the energy associated with fracture, several common formulations are encapsulated by the approximation

$$\int_{\Gamma} G_c \, dA \approx \int_{\Omega} \frac{G_c}{c_0 \ell} \left( \alpha(d) + \ell^2 \nabla d \cdot \nabla d \right) \, dV, \quad (2.2)$$

where  $\alpha(d)$  denotes a local dissipation term,  $\ell$  is the regularization length, and  $c_0$  is a normalization constant given by  $c_0 = 4 \int_0^1 \sqrt{\alpha(s)} \, ds$ .

Such a regularization implies that the distinct crack surface  $\Gamma$  is no longer defined. As such, the second integral on the right of (2.1) also needs to be approximated as a volume integral in some manner. This is effected with the use of an indicator function  $I(d)$ . The surface integral involving the pressure is then approximated as

$$\int_{\Gamma} p \mathbf{n} \cdot \mathbf{u} dA \approx \int_{\Omega} p \left( -\frac{\nabla d}{\|\nabla d\|} \right) \cdot \mathbf{u} \|\nabla I(d)\| dV. \quad (2.3)$$

Note that the crack surface normal  $\mathbf{n}$  is approximated as  $-\nabla d/\|\nabla d\|$ , whereas the differential surface element  $dA$  becomes  $\|\nabla I\| dV$ . The indicator function must satisfy  $I(0) = 0$ ,  $I(1) = 1$  and be monotonically increasing. In Bourdin et al. [1],  $I(d) = d$  was firstly proposed. Wheeler et al. [42] provide a derivation that avoids an explicit approximation of the normal, such as (2.3), but is in fact equivalent to using the indicator function  $I(d) = 2d - d^2$ . In Peco et al. [44] and Jiang et al. [45],  $I(d) = d^2$  is used, with the motivation that  $I'(0) = 0$  is required to avoid the effects of pressure in undamaged areas.

Combining the approximation in (2.3) with the traditional phase-field approximation of fracture based on the Ambrosio-Tortorelli functional [41] and applying the chain rule, the regularized counterpart of (2.1) is given by

$$U(\boldsymbol{\epsilon}, d) = \int_{\Omega} \psi_e(\boldsymbol{\epsilon}, d) dV + \int_{\Omega} p \nabla d \cdot \mathbf{u} I'(d) dV + \int_{\Omega} \frac{G_c}{c_0 \ell} \left( \alpha(d) + \ell^2 \nabla d \cdot \nabla d \right) dV - \int_{\partial\Omega_N} \mathbf{t} \cdot \mathbf{u} dA, \quad (2.4)$$

where the explicit dependence of the strain on the displacements has been dropped.

Often, the strain energy density is split and part of it is degraded with the damage, i.e.

$$\psi_e(\boldsymbol{\epsilon}(\mathbf{u}), d) = g(d) \psi_e^+(\boldsymbol{\epsilon}(\mathbf{u})) + \psi_e^-(\boldsymbol{\epsilon}(\mathbf{u})), \quad (2.5)$$

where  $g(d)$  denotes the degradation function, and  $\psi_e^+(\boldsymbol{\epsilon}(\mathbf{u}))$  and  $\psi_e^-(\boldsymbol{\epsilon}(\mathbf{u}))$  denote the “active” and “inactive” parts of the energy. The above form encapsulates most of the strain decompositions used in the literature [91],[92] to introduce asymmetry in the fracture behavior in tension and compression.

Typically, a minimization principle is applied to (2.4) to extract the governing equations for the displacements  $\mathbf{u}$  and the damage  $d$ . According to this principle, a pair  $(\mathbf{u}, d)$  is a valid state if and only if all neighboring states  $(\mathbf{u} + \delta\mathbf{u}, d + \delta d)$  have a greater potential energy. In the case of pressurized cracks, a subtle consideration leads to the formulation proposed herein. Consider the two scenarios indicated in Figure 2.2. In the situation depicted in Figure 2.2b, the pressure load (applied in the areas colored in blue), is assumed to accompany any crack propagation. Therefore, in an energetic analysis, the virtual crack extension  $da$  is assumed pressurized. By contrast, in Figure 2.2a, the pressure load is assumed to remain confined to the original crack geometry during propagation. As a result, the virtual crack extension  $da$  is not subject to any surface load.

In terms of the resulting formulation, the difference between the two scenarios shown in Figure 2.2 translate into the question of whether or not the damage variation  $\delta d$  should enter the pressure work contribution (2.3).

For the family of formulations that derived from [1] and [42], the scenario depicted in Figure 2.2b is assumed as a consequence of including the damage variation  $\delta d$  in (2.3). The proposed model in this work, by contrast, assumes the case indicated by Figure 2.2a. Although these competing views are expected to give rise to negligible differences in results in the limit as  $da \rightarrow 0$ , in practice the two formulations do give rise to slightly different sets of governing equations. As we will demonstrate in the numerical examples in Section 2.5, in practice these differences can translate into fairly significant differences in the results.

In what follows, the formulation associated with Figure 2.2a will be referred to

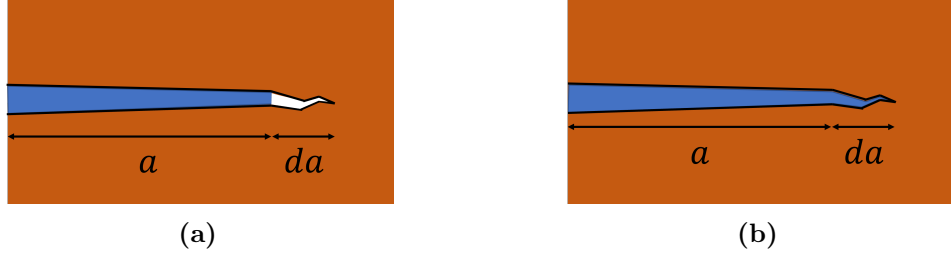


FIGURE 2.2. (a) Unloaded virtual crack. (b) Pressure loaded virtual crack;

as the Unloaded Virtual Crack formulation, or UVC for short. In the UVC, the variation of the pressure work is simply<sup>1</sup>,

$$\delta \left( \int_{\Omega} p \nabla d \cdot \mathbf{u} I'(d) dV \right) = \int_{\Omega} p \nabla d \cdot \delta \mathbf{u} I'(d) dV. \quad (2.6)$$

The variation of the potential energy  $\delta U$  can then be written as,

$$\begin{aligned} \delta U(\boldsymbol{\epsilon}, d) &= \int_{\Omega} \frac{\partial \psi_e}{\partial \boldsymbol{\epsilon}} : \delta \boldsymbol{\epsilon} dV + \int_{\Omega} p \nabla d \cdot \delta \mathbf{u} I'(d) dV - \int_{\partial \Omega_N} \mathbf{t} \cdot \delta \mathbf{u} dA \\ &\quad + \int_{\Omega} g'(d) \psi_e^+(\boldsymbol{\epsilon}) \delta d dV + \int_{\Omega} \frac{G_c}{c_0 \ell} \left( \alpha'(d) \delta d + 2\ell^2 \nabla d \cdot \nabla \delta d \right) dV, \end{aligned} \quad (2.7)$$

and, with the help of the divergence theorem,

---

<sup>1</sup> On the other hand, if the assumption of Figure 2.2b is chosen, as in [1], two additional terms have to be accounted for,

$$\delta \left( \int_{\Omega} p \nabla d \cdot \mathbf{u} I'(d) dV \right) = \int_{\Omega} p \nabla d \cdot \delta \mathbf{u} I'(d) dV + \underbrace{\int_{\Omega} p \nabla \delta d \cdot \mathbf{u} I'(d) dV + \int_{\Omega} p \nabla d \cdot \mathbf{u} \delta d I''(d) dV}_{\text{additional terms}}.$$

$$\begin{aligned}
\delta U(\boldsymbol{\epsilon}, d) = & \int_{\Omega} \left( -\nabla \cdot \frac{\partial \psi_e}{\partial \boldsymbol{\epsilon}} + pI'(d)\nabla d \right) \cdot \delta \mathbf{u} \, dV + \int_{\partial\Omega_N} \left( \frac{\partial \psi_e}{\partial \boldsymbol{\epsilon}} \cdot \mathbf{n} - \mathbf{t} \right) \cdot \delta \mathbf{u} \, dA \\
& + \int_{\Omega} \left( g'(d)\psi_e^+(\boldsymbol{\epsilon}) + \frac{G_c}{c_0\ell}\alpha'(d) - \nabla \cdot \frac{2G_c\ell}{c_0}\nabla d \right) \delta d \, dV + \int_{\partial\Omega} \frac{2G_c\ell}{c_0}(\mathbf{n} \cdot \nabla d)\delta d \, dA.
\end{aligned} \tag{2.8}$$

(2.9)

The local minimization principle requires the variation of the potential energy  $\delta U$  to be non-negative for any admissible state  $\mathbf{u}, d$ . In other words,  $\delta U(\boldsymbol{\epsilon}, d) \geq 0$ , giving rise to the following equation and boundary condition for  $\mathbf{u}$ , since the variation of the displacement field  $\delta \mathbf{u}$  is arbitrary:

$$-\nabla \cdot \boldsymbol{\sigma} + pI'(d)\nabla d = 0 \text{ on } \Omega, \tag{2.10}$$

$$\boldsymbol{\sigma} \cdot \mathbf{n} - \mathbf{t} = 0 \text{ on } \partial\Omega_N. \tag{2.11}$$

In the above,  $\boldsymbol{\sigma}$  denotes the Cauchy stress, defined as  $\boldsymbol{\sigma} = \frac{\partial \psi_e}{\partial \boldsymbol{\epsilon}}$ .

For the damage variable, it is assumed that the process is irreversible, such that  $\dot{d} \geq 0$ . As such, only positive variations in the damage are admissible, and  $\delta U(\boldsymbol{\epsilon}, d) \geq 0$  implies

$$g'(d)\psi_e^+(\boldsymbol{\epsilon}) + \frac{G_c}{c_0\ell}\alpha'(d) - \nabla \cdot \frac{2G_c\ell}{c_0}\nabla d \geq 0 \text{ on } \Omega, \tag{2.12}$$

$$\frac{2G_c\ell}{c_0}\mathbf{n} \cdot \nabla d \geq 0 \text{ on } \partial\Omega. \tag{2.13}$$

Equations (3.22) and (2.13) are identical to those in the standard phase-field model for traction-free cracks. This is the main difference between the new formulation and existing ones derived from deriving from [1] and [42], in which the governing equation for the damage field contains additional terms to account for the pressure loads on the virtual cracks. In what follows, we refer to that as the Loaded Virtual Crack formulation, or LVC. In the boxes below, the governing equations for the UVC are compared to those of the LVC.

### Unloaded Virtual Crack Formulation (UVC)

$$-\nabla \cdot \boldsymbol{\sigma} + pI'(d)\nabla d = 0 \text{ on } \Omega, \quad (2.14)$$

$$\boldsymbol{\sigma} \cdot \mathbf{n} - \mathbf{t} = 0 \text{ on } \partial\Omega_N. \quad (2.15)$$

$$g'(d)\psi_e^+(\boldsymbol{\epsilon}) + \frac{G_c}{c_0\ell}\alpha'(d) - \nabla \cdot \frac{2G_c\ell}{c_0}\nabla d \geq 0 \text{ on } \Omega, \quad (2.16)$$

$$\frac{2G_c\ell}{c_0}\mathbf{n} \cdot \nabla d \geq 0 \text{ on } \partial\Omega. \quad (2.17)$$

### Loaded Virtual Crack Formulation (LVC)

$$-\nabla \cdot \boldsymbol{\sigma} + pI'(d)\nabla d = 0 \text{ on } \Omega, \quad (2.18)$$

$$\boldsymbol{\sigma} \cdot \mathbf{n} - \mathbf{t} = 0 \text{ on } \partial\Omega_N. \quad (2.19)$$

$$g'(d)\psi_e^+(\boldsymbol{\epsilon}) + \frac{G_c}{c_0\ell}\alpha'(d) - \nabla \cdot \frac{2G_c\ell}{c_0}\nabla d - \nabla \cdot [p\mathbf{u} I'(d)] + p\nabla d \cdot \mathbf{u} I''(d) \geq 0 \text{ on } \Omega, \quad (2.20)$$

$$\mathbf{n} \cdot \left( \frac{2G_c\ell}{c_0}\nabla d + pI'(d)\mathbf{u} \right) \geq 0 \text{ on } \partial\Omega. \quad (2.21)$$

It is readily apparent that the governing equations for the displacements are identical in the UVC and the LVC. The main difference is in the absence of the additional pressure-dependent terms in the evolution for the damage field and the accompanying boundary condition.

In 2.8, an analytical study of the energy release rate of a crack propagating under an arbitrary pressure load  $p(x)$  is provided, under the assumptions of the UVC formulation and linear elastic fracture mechanics. The results of the study show that it is possible to recover the classic relationship between the energy release rate and the stress intensity factor with the UVC formulation. This ensures the consistency of the proposed formulation (UVC) with many theoretical works [93, 94, 95, 96, 97] in the field of hydraulic fracture, where the stress intensity factor is used as the propagation criteria

### 2.2.2 Derivation using the maximum dissipation principle

In this subsection, an alternative approach to derive the (UVC) formulation is presented. It is based on the construction of a total potential functional which depends on the rates of the internal variables  $\dot{\epsilon}, \dot{d}$  and accounts for the work of the pressure load as an external dissipation mechanism. This approach is described in more detail in [53] and [46], where it is used to derive a variationally consistent phase-field model for ductile fracture.

The total potential is postulated as,

$$L(\dot{\epsilon}, \dot{d}) = \int_{\Omega} \dot{u}(\dot{\epsilon}, \dot{d}) dV - \mathcal{P}^{ext}, \quad (2.22)$$

where  $u$  is the material internal energy, which relates to the Helmholtz free-energy  $\psi$  through  $\dot{u} = \dot{\psi} + \dot{T}s$ , where  $T$  is the temperature and  $s$  the entropy. In this work, only isothermal processes are considered, therefore,  $\dot{u} = \dot{\psi}$ . The term  $\mathcal{P}^{ext}$  denotes

the external power expenditure. If cracks were represented by internal boundaries  $\Gamma$  instead of a damage field, one could write,

$$\mathcal{P}^{ext} = \int_{\partial\Omega \cup \Gamma} \mathbf{t} \cdot \dot{\mathbf{u}} dA = \int_{\partial\Omega} \mathbf{t} \cdot \dot{\mathbf{u}} + \int_{\Gamma} p\mathbf{n} \cdot \dot{\mathbf{u}} dA. \quad (2.23)$$

However, in a regularized setting this integral over  $\Gamma$  is once again transformed into a volume integral over  $\Omega$ , as in (2.3),

$$\int_{\Gamma} p\mathbf{n} \cdot \dot{\mathbf{u}} dA \approx \int_{\Omega} p \left( -\frac{\nabla d}{\|\nabla d\|} \right) \cdot \dot{\mathbf{u}} \|\nabla I(d)\| dV = - \int_{\Omega} p \nabla d \cdot \dot{\mathbf{u}} I'(d) dV. \quad (2.24)$$

Recalling the equivalence between the internal energy and the Helmholtz free-energy, the Coleman-Noll procedure can be applied and, in combination with (2.23) and (2.24), leads to the following expression for  $L$  as a function of  $\psi$ :

$$L(\dot{\epsilon}, \dot{d}) = \int_{\Omega} \left( \frac{\partial \psi}{\partial \epsilon} : \dot{\epsilon} + \frac{\partial \psi}{\partial d} \dot{d} + \frac{\partial \psi}{\partial \nabla d} \cdot \nabla \dot{d} + p \nabla d \cdot \dot{\mathbf{u}} I'(d) \right) dV - \int_{\partial\Omega} \mathbf{t} \cdot \dot{\mathbf{u}} dA. \quad (2.25)$$

The evolution process is postulated to follow the minimizers of this total potential, with the supplemental conditions that damage is an irreversible process and that the displacements  $\mathbf{u}$  are prescribed over a subset  $\partial\Omega_D$  of the boundary. In other words,

$$\dot{\epsilon}, \dot{d} = \underset{\dot{\epsilon}, \dot{d}}{\operatorname{argmin}} L(\dot{\epsilon}, \dot{d}), \text{ subject to } \dot{d} \geq 0 \text{ and } \mathbf{u} = \mathbf{g} \text{ on } \partial\Omega_D. \quad (2.26)$$

Using the Euler-Lagrange equations, the following general evolution equations can then be obtained in terms of the free-energy function  $\psi$ :

$$\nabla \cdot \frac{\partial \psi}{\partial \epsilon} - pI'(d)\nabla d = 0 \text{ on } \Omega, \quad (2.27)$$

$$\nabla \cdot \frac{\partial \psi}{\partial \nabla d} - \frac{\partial \psi}{\partial d} \geq 0 \text{ on } \Omega, \quad (2.28)$$

with the boundary conditions

$$\frac{\partial \psi}{\partial \epsilon} \cdot \mathbf{n} - \mathbf{t} = 0 \text{ on } \partial \Omega \setminus \partial \Omega_D \quad (2.29)$$

$$\mathbf{n} \cdot \frac{\partial \psi}{\partial \nabla d} \geq 0 \text{ on } \partial \Omega. \quad (2.30)$$

To be consistent with the derivation in subsection 2.2.1, the Helmholtz free-energy is postulated as,

$$\psi(\epsilon, d) = \psi_e(\epsilon, d) + \frac{G_c}{c_0 \ell} \left( \alpha(d) + \ell^2 \nabla d \cdot \nabla d \right), \quad (2.31)$$

following the regularization based on the Ambrosio-Tortorelli functional. In this case, the general equations (2.27)-(2.30) take the form

$$-\nabla \cdot \boldsymbol{\sigma} + pI'(d)\nabla d = 0 \text{ on } \Omega, \quad (2.32)$$

$$g'(d)\psi_e^+(\epsilon) + \frac{G_c}{c_0 \ell} \alpha'(d) - \nabla \cdot \frac{2G_c \ell}{c_0} \nabla d \geq 0 \text{ on } \Omega, \quad (2.33)$$

with the boundary conditions

$$\boldsymbol{\sigma} \cdot \mathbf{n} - \mathbf{t} = 0 \text{ on } \partial \Omega_N, \quad (2.34)$$

$$\mathbf{n} \cdot \nabla d \geq 0 \text{ on } \partial \Omega. \quad (2.35)$$

By inspection, (2.32)-(2.35) are identical to (2.10)-(2.13).

### 2.2.3 Constitutive choices of the phase-field formulation

In the previous subsection, the proposed model for pressurized cracks was developed for a general phase-field regularization of the variational approach to fracture [48], with a free-energy of the form

$$\psi(\boldsymbol{\epsilon}, d) = \underbrace{g(d)\psi_e^+(\boldsymbol{\epsilon}) + \psi_e^-(\boldsymbol{\epsilon})}_{\psi_e} + \underbrace{\frac{G_c}{c_0\ell} \left( \alpha(d) + \ell^2 \nabla d \cdot \nabla d \right)}_{\psi_f}. \quad (2.36)$$

In what follows, the constitutive choices used in the example problems provided in Section 2.5 are described.

#### 2.2.3.1 Elastic energy and decomposition

First, in terms of the solid bulk response, an elastic energy of the type (2.5) is assumed. When the material is undamaged, it reduces to a purely linear elastic energy, that is,

$$\psi_e(\boldsymbol{\epsilon}(\mathbf{u}), 0) = \psi_e^+(\boldsymbol{\epsilon}(\mathbf{u}), 0) + \psi_e^-(\boldsymbol{\epsilon}(\mathbf{u}), 0) = \frac{1}{2} \boldsymbol{\epsilon}(\mathbf{u}) : \mathbb{C} : \boldsymbol{\epsilon}(\mathbf{u}), \quad (2.37)$$

where  $\mathbb{C}$  is the elasticity tensor.

When damage is present, a decomposition of the energy is often assumed. In many cases, when the applied load to a fracturing body is predominately tensile, the “no-split” case given by,

$$\psi_e^-(\boldsymbol{\epsilon}(\mathbf{u}), d) = 0 \rightarrow \psi_e(\boldsymbol{\epsilon}(\mathbf{u}), d) = \frac{1}{2} g(d) \boldsymbol{\epsilon}(\mathbf{u}) : \mathbb{C} : \boldsymbol{\epsilon}(\mathbf{u}), \quad (2.38)$$

is capable of correctly predicting the material response, while leading to a simpler set of governing equations. However, in a wide-range of scenarios, compressive forces are present, and an energy split is needed to prevent crack formation in zones of

high compression, as well as to allow for transmission of compressive forces across fractured faces.

In Section 2.5, one of the example problems will employ the spectral split of Miehe et al. [92], given by,

$$\psi_e^+(\boldsymbol{\epsilon}(\mathbf{u}), d) = \frac{1}{2}\lambda \langle \text{Tr } \boldsymbol{\epsilon} \rangle_+^2 + \mu \boldsymbol{\epsilon}^+ : \boldsymbol{\epsilon}^+ \text{ and } \psi_e^-(\boldsymbol{\epsilon}(\mathbf{u}), d) = \frac{1}{2}\lambda \langle \text{Tr } \boldsymbol{\epsilon} \rangle_-^2 + \mu \boldsymbol{\epsilon}^- : \boldsymbol{\epsilon}^-.$$
(2.39)

Here,  $\langle \cdot \rangle_+$  and  $\langle \cdot \rangle_-$  denote the positive and negative parts of a number respectively, while  $\boldsymbol{\epsilon}^+$  and  $\boldsymbol{\epsilon}^-$  are the positive and negative parts of an additive decomposition of the strain tensor based on the signs of its eigenvalues. A more detailed description, including the derivation of the stiffness matrix in this case, is provided by Jiang et al. [98].

#### 2.2.3.2 Brittle fracture

The first and more traditional phase-field model with an energy of the type (2.36) was proposed in [41]. It was developed to approximate the brittle fracture process of linear elastic materials in the limit of vanishing  $\ell$ . In its original form, the degradation function

$$g(d) = \xi + (1 - \xi)(1 - d)^2, \quad (2.40)$$

is used in combination with a quadratic local dissipation  $\alpha(d) = d^2$ , in what is now called the AT-2 formulation. However, the use of,  $\alpha(d) = d$ , (widely referred as the AT-1) comes with the advantage of a purely elastic response before the onset of damage and a compactly supported damage field. Therefore, it will be employed in the example in Section 2.5 where brittle fracture is investigated. The parameter  $\xi$  in

(2.40) is the residual stiffness, a very small numerical parameter that avoids the loss of ellipticity in fully damaged material.

### 2.2.3.3 Cohesive fracture

The phase-field model for cohesive fracture was first proposed by Lorentz et al. [84, 99]. In this model, the use of a quasi-quadratic degradation function, given by

$$g(d) = \xi + (1 - \xi) \frac{(1 - d)^2}{(1 - d)^2 + md(1 + pd)}, \quad (2.41)$$

is combined with a linear local dissipation function  $\alpha(d) = d$ . The parameter  $m$  is defined as  $m = \frac{G_c}{c_0 \ell \psi_c}$ , where  $\psi_c$  is the nucleation energy, below which no damage is expected to form. The parameter  $p$  is a shape parameter that can be used to adjust the traction-separation response. In this work,  $p = 1$  is used.

## 2.3 A J-Integral for pressurized cracks in a phase-field setting

This Section presents a modified J-integral, capable of retrieving  $G$  in the case of pressurized cracks in a phase-field for fracture setting. The resulting integral is then re-cast into a domain-independent form that is more amenable to finite-element calculations.

A common form of the J-integral, derived for phase-field fracture and applicable to traction-free cracks is given by [86, 87]

$$J = \mathbf{r} \cdot \int_{\zeta} \left( \psi(\boldsymbol{\epsilon}, d) \mathbb{I} - \nabla \mathbf{u}^T \boldsymbol{\sigma} - \nabla d \otimes \boldsymbol{\omega} \right) \mathbf{n} ds, \quad (2.42)$$

where  $\psi(\boldsymbol{\epsilon}, d)$  is given by equation (2.36). In the above, the vector  $\mathbf{r}$  denotes the crack propagation direction,  $\zeta$  is a closed path around the crack tip,  $\mathbb{I}$  is the second-order identity tensor,  $\mathbf{n}$  is the normal to the closed path  $\zeta$  and  $\boldsymbol{\omega} = \partial \psi / \partial \nabla d = (G_c \ell / c_0) \nabla d$ .

Compared to the original form of the J-integral proposed by Rice [100, 101], this expression contains additional terms to account for the phase-field parameter  $d$ .

Importantly, Sicsic and Marigo [86] show that, under certain conditions, the standard form of the J-integral widely employed for sharp cracks, viz.

$$J = \mathbf{r} \cdot \int_{\zeta} \left( \psi_e(\boldsymbol{\epsilon}, d) \mathbb{I} - \nabla \mathbf{u}^T \boldsymbol{\sigma} \right) \mathbf{n} ds, \quad (2.43)$$

can be used in a regularized phase-field setting. These conditions are:

**H1** : The regularization length is sufficiently small, so that a separation of scales between the solution in the damage band and the outer solution can be achieved;

**H2** : The path  $\zeta$  intersects the crack plane at a ninety-degree angle;

**H3** : The path  $\zeta$  intersects the crack plane sufficiently far from the crack tip, so that the damage field only varies in a direction perpendicular to the crack plane.

In what follows, these same conditions are assumed, as they facilitate a simpler derivation of a modified J-Integral capable of retrieving the energy release rate even in the presence of pressure loads on the crack faces. The main result of this section can then be stated in the following way.

**Claim:** Consider a domain  $\Omega \in \mathbb{R}^2$  with a straight phase-field crack and two closed, non-intersecting paths  $\zeta_{in}$  and  $\zeta_{out}$  around the crack tip, enclosing an area  $\Lambda$  as shown in Figure 2.3a. Let  $q(x)$  be a sufficiently smooth function satisfying  $q = 1$  on  $\zeta_{in}$  and  $q = 0$  on  $\zeta_{out}$ . Further, assume that  $q = 1$  for all points inside  $\zeta_{in}$  and  $q = 0$  for all points outside  $\zeta_{out}$ , as shown in Figure 2.3b. Finally, assume that the fracture is loaded by a constant pressure  $p$ , and that one of the formulations described in

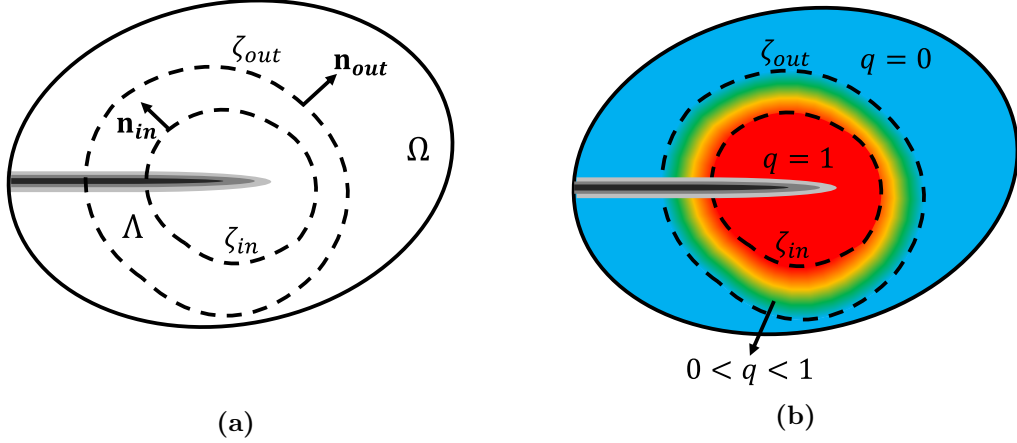


FIGURE 2.3. (a) The contour paths  $\zeta_{in}$  and  $\zeta_{out}$  and subdomain  $\Lambda$ , in the vicinity of a regularized crack.; (b) Color contour plot indicating the assumed variation in the function  $q$ .

Section 2.2 holds. Then, if conditions **H1**, **H2** and **H3** hold for  $\zeta_{in}$  and  $\zeta_{out}$ , the energy release rate can be approximated by the integral

$$J = \mathbf{r} \cdot \int_{\Lambda} \left( \psi_e(\boldsymbol{\epsilon}, d)\mathbb{I} - p\nabla d \cdot \mathbf{u} I'(d)\mathbb{I} - \nabla \mathbf{u}^T \boldsymbol{\sigma} \right) \cdot \nabla q \, dA, \quad (2.44)$$

with an error that vanishes as  $\ell \rightarrow 0$ . The proof can be established in three steps, as detailed below.

**Proof:** Define  $\mathbf{T}_p = \psi_e(\boldsymbol{\epsilon}, d)\mathbb{I} - p\nabla d \cdot \mathbf{u} I'(d)\mathbb{I} - \nabla \mathbf{u}^T \boldsymbol{\sigma}$ . Using the divergence theorem, one can show that

$$\int_{\Lambda} \nabla \cdot (q\mathbf{T}_p) \, dA = \int_{\zeta_{in} \cup \zeta_{out}} q\mathbf{T}_p \cdot \mathbf{n} \, ds = 0 - \int_{\zeta_{in}} \mathbf{T}_p \cdot \mathbf{n} \, ds, \quad (2.45)$$

because  $q$  vanishes on  $\zeta_{out}$  and the normal  $\mathbf{n}$  to  $\zeta_{in}$  points inward to  $\Lambda$ , as shown in Figure 2.3a. Multiplying both sides by the crack direction  $\mathbf{r}$  and applying the chain rule yields

$$-\mathbf{r} \cdot \int_{\Lambda} \left( \mathbf{T}_p \cdot \nabla q + q \nabla \cdot \mathbf{T}_p \right) \, dA = \mathbf{r} \cdot \int_{\zeta_{in}} \mathbf{T}_p \cdot \mathbf{n} \, ds, \quad (2.46)$$

which completes the first step of the proof.

The second step consists of showing that the term  $R = \mathbf{r} \cdot \int_{\Lambda} q \nabla \cdot \mathbf{T}_p \, dA$  is zero.

Expanding the expression for  $\mathbf{T}_p$  and using the chain rule yields

$$R = \mathbf{r} \cdot \int_{\Lambda} q \nabla \cdot \left( \psi_e(\boldsymbol{\epsilon}, d) \mathbb{I} - p \nabla d \cdot \mathbf{u} I'(d) \mathbb{I} - \nabla \mathbf{u}^T \boldsymbol{\sigma} \right) \, dA = \\ \int_{\Lambda} q \left( \frac{\partial \psi_e(\boldsymbol{\epsilon}, d)}{\partial \nabla^s \mathbf{u}} \cdot (\nabla(\nabla^s \mathbf{u}) \mathbf{r}) + \frac{\partial \psi_e(\boldsymbol{\epsilon}, d)}{\partial d} \nabla d \cdot \mathbf{r} - (\nabla \cdot \boldsymbol{\sigma}) (\nabla \mathbf{u} \mathbf{r}) - \boldsymbol{\sigma} (\nabla \cdot \mathbf{u}) \mathbf{r} \right) \, dA$$

Re-arranging some terms, one can write,

$$R = \int_{\Lambda} q \left[ \left( \frac{\partial \psi_e(\boldsymbol{\epsilon}, d)}{\partial \nabla^s \mathbf{u}} - \boldsymbol{\sigma} \right) \cdot (\nabla(\nabla^s \mathbf{u}) \mathbf{r}) - \left( \nabla \cdot \boldsymbol{\sigma} - p I'(d) \nabla d \right) \cdot (\nabla \mathbf{u} \mathbf{r}) + \frac{\partial \psi_e(\boldsymbol{\epsilon}, d)}{\partial d} \nabla d \cdot \mathbf{r} \right] \, dA. \quad (2.48)$$

For any elastic material, the definition of stress implies  $\frac{\partial \psi_e(\boldsymbol{\epsilon}, d)}{\partial \nabla^s \mathbf{u}} - \boldsymbol{\sigma} = 0$ , and due to equation (2.27),  $\nabla \cdot \boldsymbol{\sigma} - p \nabla d = 0$ , so, the expression above reduces to

$$R = \int_{\Lambda} q \left( \frac{\partial \psi_e(\boldsymbol{\epsilon}, d)}{\partial d} \nabla d \cdot \mathbf{r} - p \mathbf{u} \nabla(I'(d) \nabla d) \mathbf{r} \right) \, dA. \quad (2.49)$$

Assuming a separation of scales, the domain  $\Lambda$  can be separated into two regions: (i)  $\Lambda_{band}$ , which consists of the intersection between  $\Lambda$  and the support of the damage field representing the crack and (ii)  $\Lambda_{outer}$ , which denotes the remainder of  $\Lambda$ , outside of the damage band. In the asymptotic limit as  $\ell \rightarrow 0$ , the material in  $\Lambda_{outer}$  behaves as purely elastic. Within  $\Lambda_{outer}$ , one has  $d \approx \nabla d \approx 0$ , and therefore,

$$R_{outer} = \int_{\Lambda_{outer}} q \left( \frac{\partial \psi_e(\boldsymbol{\epsilon}, d)}{\partial d} \nabla d \cdot \mathbf{r} - p \mathbf{u} \nabla(I'(d) \nabla d) \mathbf{r} \right) \, dA \approx 0. \quad (2.50)$$

For the  $\Lambda_{band}$  region, by condition **H3**,  $\nabla d$  is purely perpendicular to the crack direction, so,  $\nabla d \cdot \mathbf{r} \approx 0$ . Therefore,

$$R_{band} = \int_{\Lambda_{band}} q \left( \frac{\partial \psi_e(\boldsymbol{\epsilon}, d)}{\partial d} \nabla d \cdot \mathbf{r} - p \mathbf{u} \nabla(I'(d) \nabla d) \mathbf{r} \right) dA \approx 0. \quad (2.51)$$

Since  $\Lambda = \Lambda_{band} \cup \Lambda_{outer}$ , we must have

$$R = R_{outer} + R_{band} \approx 0. \quad (2.52)$$

This completes the second step.

The final step of the proof begins by invoking the separation of scales to decompose the contour integral in (2.46) via

$$\mathbf{r} \cdot \int_{\zeta_{in}} \mathbf{T}_p \cdot \mathbf{n} ds = \mathbf{r} \cdot \left( \int_{\zeta_{in}^{band}} \mathbf{T}_p \cdot \mathbf{n} ds + \int_{\zeta_{in}^{outer}} \mathbf{T}_p \cdot \mathbf{n} ds \right). \quad (2.53)$$

On the  $\zeta_{in}^{outer}$  portion of the path, damage effects can be neglected and the integral simplifies to the standard (sharp) J-Integral. In the case of a uniformly pressurized crack [102], this gives

$$\int_{\zeta_{in}^{outer}} \mathbf{T}_p \cdot \mathbf{n} ds = G - pw, \quad (2.54)$$

where  $w$  denotes the crack aperture at the intersection of the crack and the contour  $\zeta_{in}$ .

The other portion of the integral can be re-written as

$$\mathbf{r} \cdot \int_{\zeta_{in}^{band}} \mathbf{T}_p \cdot \mathbf{n} ds = \mathbf{r} \cdot \int_{-B}^B (\psi_e \mathbb{I} - \nabla \mathbf{u}^T \boldsymbol{\sigma}) \cdot \mathbf{n} dx - \mathbf{r} \cdot \int_{-B}^B p(\nabla d \cdot \mathbf{u} I'(d)) \cdot \mathbf{n} dx, \quad (2.55)$$

where  $B$  is the half-length of the damage band and condition **H2** is used to transform the integral over  $\zeta_{in}^{band}$  to a simple real integral from  $-B$  to  $B$ . Here, both  $\mathbf{r}$  and  $\mathbf{n}$  are unit vectors that point in opposite directions, and therefore,  $\mathbf{r} \cdot \mathbf{n} = -1$ , so,

$$\mathbf{r} \cdot \int_{\zeta_{in}^{band}} \mathbf{T}_p \cdot \mathbf{n} \, ds = \int_{-B}^B (\psi_e \mathbb{I} - \nabla \mathbf{u}^T \boldsymbol{\sigma}) dx + p \int_{-B}^B (\nabla d \cdot \mathbf{u} I'(d)) dx. \quad (2.56)$$

Following [1], the second integral on the right approaches the crack aperture  $w$  as the regularization length decreases, while the first integrand on the right is bounded [86], and therefore this term is  $O(B)$ , so,

$$\mathbf{r} \cdot \int_{\zeta_{in}^{band}} \mathbf{T}_p \cdot \mathbf{n} \, ds = O(B) + pw = O(\ell) + pw, \quad (2.57)$$

since the damage band half-length  $B$  scales with the regularization length  $\ell$ . One can now go back to (2.53), and substitute (2.54) and (2.57) to obtain,

$$\mathbf{r} \cdot \int_{\zeta_{in}} \mathbf{T}_p \cdot \mathbf{n} \, ds = G + pw - pw + O(\ell). \quad (2.58)$$

Finally, combining (2.46), (2.52) and (2.58), one obtains

$$-\mathbf{r} \cdot \int_{\Lambda} \mathbf{T}_p \cdot \nabla q \, dA = G + O(\ell), \quad (2.59)$$

which concludes the proof.

## 2.4 Finite Element Implementation

In this Section, the details of the finite element discretization used to obtain approximations to the solution of the proposed model (UVC) are described. For analogous

equations for the model (LVC), the reader is referred to [45]. First, the strong form of the governing equations, derived from the general free-energy (2.36) using the KKT[103, 104] conditions is presented.

### Strong form

$$\text{Linear momentum balance: } \nabla \cdot \boldsymbol{\sigma} - p \nabla d + \mathbf{b} = 0, \quad \forall x \in \Omega,$$

$$\boldsymbol{\sigma} = \frac{\partial \psi_e}{\partial \epsilon}, \quad \forall x \in \Omega,$$

$$\boldsymbol{\sigma} \cdot \mathbf{n} = \mathbf{t}, \quad \partial_t \Omega,$$

$$\mathbf{u} = \mathbf{u}_g, \quad \partial_u \Omega,$$

$$\text{Fracture evolution: } \dot{d} \left( \nabla \cdot \frac{2G_c \ell}{c_0} \nabla d - \frac{G_c}{c_0 \ell} \alpha'(d) - g'(d) \psi_e^+(\boldsymbol{\epsilon}) \right) = 0, \quad \forall x \in \Omega,$$

$$\nabla \cdot \frac{2G_c \ell}{c_0} \nabla d - \frac{G_c}{c_0 \ell} \alpha'(d) - g'(d) \psi_e^+(\boldsymbol{\epsilon}) \leq 0, \quad \forall x \in \Omega,$$

$$\dot{d} \geq 0, \quad \forall x \in \Omega,$$

$$\nabla d \cdot \mathbf{n}_0 = 0, \quad \partial \Omega,$$

$$d(0, \mathbf{x}) = d_0, \quad \Omega. \tag{2.60}$$

$$(2.61)$$

$$(2.62)$$

$$(2.63)$$

$$(2.64)$$

$$(2.65)$$

$$(2.66)$$

$$(2.67)$$

$$(2.68)$$

For the derivation of an equivalent weak form, trial spaces for  $\mathbf{u}$  and  $d$  are first defined. Although the derivation is confined to quasi-static loadings, the spaces are indexed by a discrete load step parameter  $t$ . The trial spaces are given by

$$\mathcal{U}_t = \{\mathbf{u} \in \mathcal{H}^1(\Omega)^d \mid \mathbf{u} = \bar{\mathbf{u}}_t \text{ on } \partial_u \Omega\}, \quad (2.69)$$

$$\mathcal{D}_t = \{d \in \mathcal{H}^1(\Omega) \mid d_{t-1}(x) \leq d_t(x) \leq 1, \forall x \in \Omega\}, \quad (2.70)$$

and the accompanying weighting spaces  $\mathcal{V}$  and  $\mathcal{C}$  are

$$\mathcal{V} = \{\mathbf{w} \in \mathcal{H}^1(\Omega)^d \mid \mathbf{w} = \mathbf{0} \text{ on } \partial_u \Omega\}, \quad (2.71)$$

$$\mathcal{C} = \{c \in \mathcal{H}^1(\Omega) \mid c(x) \geq 0, \forall x \in \Omega\}. \quad (2.72)$$

The condition of monotonicity in the space  $\mathcal{D}_t$  is used to prevent damage healing and is the weak enforcement of the condition  $\dot{d} \geq 0$ , in a time discrete setting. Denoting the inner product in  $\mathcal{H}^1(\Omega)$  and  $\mathcal{H}^1(\Omega)^d$  by  $(\cdot, \cdot)$  and its restriction in the boundary by  $\langle \cdot, \cdot \rangle$ , the weak form of the problem can be written as

### Weak form

Find  $\mathbf{u} \in \mathcal{U}_t$  and  $d \in \mathcal{D}_t$ , such that  $\forall \mathbf{w} \in \mathcal{V}$  and  $\forall c \in \mathcal{C}$ ,

$$(\nabla \mathbf{w}, \boldsymbol{\sigma}) - (\mathbf{w}, p \nabla d) - (\mathbf{w}, \mathbf{b}) - \langle \mathbf{w}, \mathbf{t} \rangle_{\partial_t \Omega} = 0, \quad (2.73)$$

$$\frac{2\ell}{c_0} (\nabla c, G_c \nabla d) + \frac{1}{c_0 \ell} (c, G_c \alpha'(d)) + (c, g'(d) \psi_e^+(\boldsymbol{\epsilon}(\mathbf{u}))) = 0, \quad (2.74)$$

with the initial damage condition,

$$(c, d(0, \mathbf{x}) - d_0) = 0. \quad (2.75)$$

Observe that (2.74) is an equality rather than an inequality, such as (2.65). This reflects a view ahead, toward discretization, where in the present work the irreversibility constraint is enforced with an active-set strategy. The active set strategy effectively partitions the domain into active (where  $\dot{d} = 0$ ) and inactive (where  $\dot{d} > 0$ ) parts. Only the inactive part requires a discretization of the damage condition (2.65), where it is indeed treated as an equality. A detailed description of this constrained optimization algorithm is given by Heister et al. in [105], and some additional details pertinent to phase-field for fracture discretizations can be found in Hu et al. [106].

Finally, these function spaces can be discretized over a finite element mesh, that give rise to the discrete function spaces  $\mathcal{U}_t^h \subset \mathcal{U}_t$ ,  $\mathcal{V}^h \subset \mathcal{V}$ ,  $\mathcal{D}_t^h \subset \mathcal{D}_t$ ,  $\mathcal{C}^h \subset \mathcal{C}$ . These are then used to construct the discrete form of the problem using the Galerkin method:

### Spatially discretized form

Find  $\mathbf{u}^h \in \mathcal{U}_t^h$  and  $d^h \in \mathcal{D}_t^h$ , such that  $\forall \mathbf{w}^h \in \mathcal{V}^h$  and  $\forall q^h \in \mathcal{C}^h$ ,

$$(\nabla \mathbf{w}^h, \boldsymbol{\sigma}^h) - (\mathbf{w}^h, p \nabla d^h) - (\mathbf{w}^h, \mathbf{b}) - \langle \mathbf{w}^h, \mathbf{t} \rangle_{\partial_t \Omega} = 0, \quad (2.76a)$$

$$\frac{2\ell}{c_0} (\nabla c^h, G_c \nabla d^h) + \frac{1}{c_0 \ell} (c^h, G_c \alpha'(d^h)) + (c^h, g'(d^h) \psi_e^+(\boldsymbol{\epsilon}(\mathbf{u}^h))) = 0, \quad (2.76b)$$

with the initial damage condition,

$$(c^h, d^h(0, \mathbf{x}) - d_0) = 0. \quad (2.77a)$$

In this work, bilinear finite elements are used to approximate the damage and displacement fields. The coupling between the two discrete equations 3.31 and 2.76b is handled by an alternating minimization scheme. A detailed description of this scheme is given in [106]. This solution scheme is implemented using RACCOON [107], a massively parallel finite element code specializing in phase-field fracture problems. RACCOON is built upon the MOOSE framework [108, 109] developed at the Idaho National Laboratory.

## 2.5 Results

We now present results for a set of problems that highlight the advantages, as well as some limitations, of the various models for pressurized cracks in a phase-field for fracture setting. In the first problem, the cohesive fracture of an uniaxial specimen in a pressurized environment is analyzed. We then consider the problem of crack nucleation from a pressurized hole in a media subjected to far-field, biaxial compression. Finally, a crack propagation example is studied to verify that in the limit

of a vanishing regularization length Griffith-like behavior is recovered with the new model. In all cases, plane-strain conditions are assumed to hold.

In the course of explaining the results obtained with the cohesive phase-field model, it will be useful to characterize the effective cohesive strength  $\sigma_c$  of the material. To that end we will rely on the following relationship between the cohesive strength and the nucleation energy:

$$\sigma_c = \sqrt{\frac{2E\psi_c}{(1-\nu^2)}}, \quad (2.78)$$

where  $E$  denotes Young's modulus and  $\nu$  Poisson's ratio. This equation results from the analysis of a one-dimensional system subjected to uniaxial loading [85], and should be viewed as an approximation to the cohesive strength in more general loading conditions.

### 2.5.1 Uniaxial bar under traction in a pressurized environment

We consider the fracture behavior of a cohesive material with pressure loading on the crack faces. The example is intended to examine the extent to which the pressure loading can artificially influence the apparent traction-separation law on the crack surface.

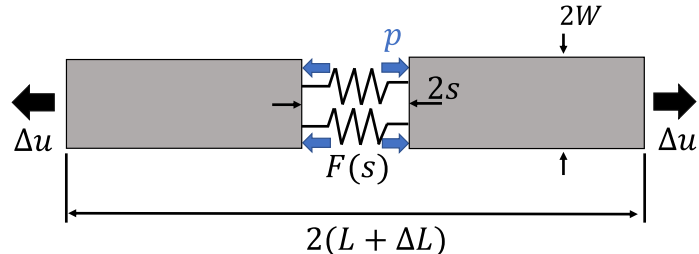


FIGURE 2.4. Uniaxial cohesive bar.

The problem consists of a bar under a displacement controlled load in a pressurized chamber, as shown in Figure 2.4. The bar is assumed to be made of a

**Table 2.1.** Material properties for uniaxial bar

	Value	Unit
Young's modulus ( $E$ )	$4.0 \times 10^5$	MPa
Poisson's ratio ( $\nu$ )	0.2	—
Nucleation energy ( $\psi_c$ )	$5.6 \times 10^{-5}$	$\text{mJ mm}^{-3}$
Critical fracture energy ( $G_c$ )	0.12	$\text{mJ mm}^{-2}$
Residual stiffness ( $\xi$ )	$1.0 \times 10^{-8}$	—

linear elastic material that undergoes cohesive fracture, with a traction-separation law  $F(s)$ . The bar has an undeformed length  $2L = 400$  mm and width  $2W = 2$  mm. The material properties are given in Table 2.1. Symmetry boundary conditions are invoked to reduce the computational domain to the top-right quarter of the bar. The applied load is modeled as a displacement boundary condition on the right end of the domain. The mesh consists of rectangular elements of size  $h$  along the length direction and size 1 mm in the width direction. The initial applied displacement increment is  $\Delta u = 5 \times 10^{-4}$  mm. The displacement increment is adaptively refined when convergence is not obtained within a fixed set of iterations. A more detailed description of the adaptive stepping procedure is provided in [108, 109, 110].

Damage localization is triggered by introducing a small initial defect ( $d = \mathcal{O}(\epsilon)$ ) on the left side of the domain. In what follows, results are reported using  $\ell = L/20 = 10$  mm and  $h = \ell/10 = 1$  mm. This choice of regularization length and mesh spacing was found to yield spatially-converged results. Different values of pressure, ranging from 0 to  $\sigma_c/3$  are considered.

The problem is simulated using discretized versions of both the UVC and (LVC) formulations. For the indicator function  $I(d)$ , results are reported for: (1)  $I(d) = d$ , used for example in [1]; (2)  $I(d) = d^2$ , used in [45] and (3)  $I(d) = 2d - d^2$ , used in [42]. The effective traction-separation laws extracted from the set of simulations are shown in Figure 2.5. To generate these curves, the traction is computed as the internal force measured in the center of the bar. The separation  $s$  is the opening of

the crack, calculated as  $s = - \int_{-\infty}^{\infty} \mathbf{u} \cdot \nabla I(d) dx$  [1].

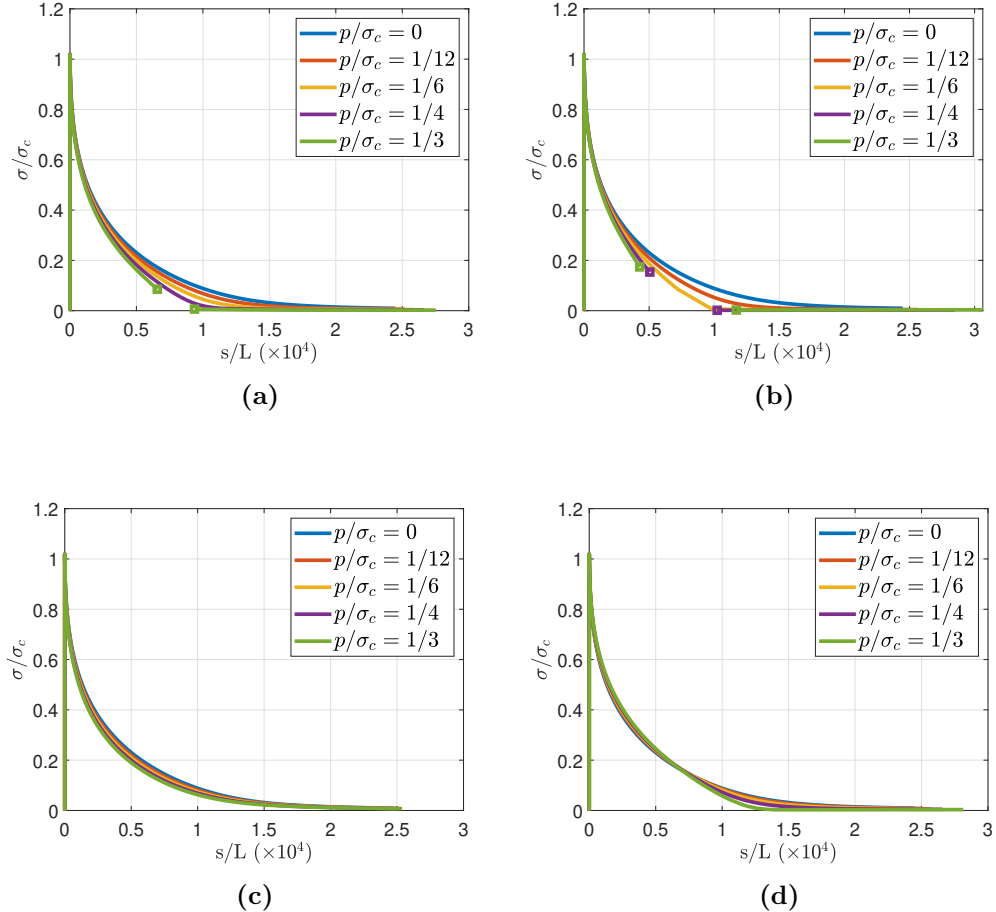


FIGURE 2.5. Traction-separation curves for pressurized uniaxial cohesive bar problem, obtained with various phase-field models: (a) (LVC) with linear indicator function; (b) (LVC) with quadratic indicator function; (c) (LVC) with  $2d - d^2$  indicator function; and (d) Proposed approach (UVC) with linear indicator function.

The results for the various models are shown in Figure 2.5, with tractions and pressures normalized by the critical stress  $\sigma_c$  from (2.78). As shown in Figure 2.5, the proposed model (UVC) exhibits minimal sensitivity to the pressure magnitude in the traction-separation behavior. By contrast, with the (LVC) formulation, only the case with  $I(d) = 2d - d^2$  exhibits comparable results. In the other two cases (Figures

2.5a and 2.5b), the apparent traction-separation law shows a spurious dependence to the applied pressure. This is evident in the variations in the results as well as the presence of jumps in the aperture at sufficiently high pressures. The latter occur due to an instability of the partially damaged solutions as  $d$  approaches 1. More precisely, shortly after the damage at the center of the bar reaches  $d \approx 0.8$ , it jumps to  $d = 1$ , which in turns lead to a jump in the aperture. This jump is indicated via the squares that appear on selected curves in Figures 2.5a and 2.5b. The use of smaller displacement increments was not observed to significantly impact these results. By contrast, such instabilities were not observed for the simulations reported in Figures 2.5c and 2.5d.

### 2.5.2 Crack nucleation from a pressurized hole

Consider a square plate of dimensions  $L \times L$ , with a circular hole in the center subjected to an internal pressure  $p$ , as shown in Figure 2.6a. This problem is motivated by oil and gas wellbore systems. Far field stresses  $\sigma_V$  and  $\sigma_H$  are applied as tractions on the boundaries as shown. The pressure is increased until it reaches a “break-down pressure”  $p_b$ . When that happens, cracks initiate in the direction parallel to the maximum *in-situ* stress. Assuming  $\sigma_H > \sigma_V$ , this is expected to occur along a horizontal axis passing through the center of the hole. In this work, the pressure in the hole is assumed to follow the crack faces as the fracture grows into the interior of the domain.

The material properties selected for this problem, along with the dimensions and loading parameters are listed in Table 2.2. The material properties are taken to be representative of a Bebertal sandstone, as inspired by the experiments of [111]. The symmetry of the problem is exploited to reduce the computational domain to the top-left quarter. An unstructured triangular mesh is used, with local refinement along the  $x$ -axis, as shown in Figure 2.6b. The element size in the refined area is 10mm,

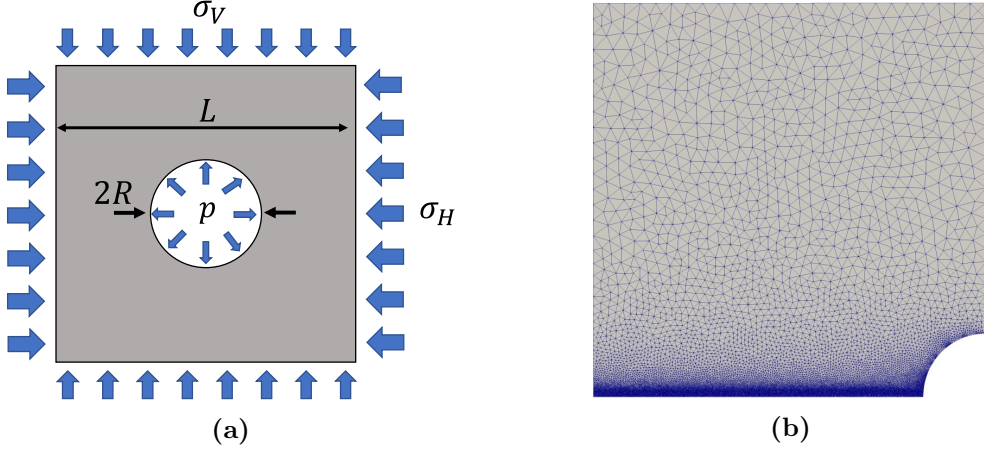


FIGURE 2.6. (a) Problem schematic; (b) Mesh used in the computations, exploiting symmetry.

**Table 2.2.** Material properties, geometric parameters and applied loads for crack initiation problem

	Value	Unit
Young's modulus ( $E$ )	$19.0 \times 10^3$	MPa
Poisson's ratio ( $\nu$ )	0.2	—
Nucleation energy ( $\psi_c$ )	$7.96 \times 10^{-4}$	$\text{mJ mm}^{-3}$
Critical fracture energy ( $G_c$ )	$7.70 \times 10^{-2}$	$\text{mJ mm}^{-2}$
Cavity radius ( $R$ )	400	mm
Specimen length ( $L$ )	$5.0 \times 10^3$	mm
Horizontal stress ( $\sigma_H$ )	5.0	MPa
Vertical stress ( $\sigma_V$ )	2.5	MPa

whereas the phase-field regularization length is  $\ell = 40\text{mm}$ . For the results reported in this section, the phase-field model employs the cohesive formulation[84, 85] using the degradation function (2.41) and the spectral split of [92].

Intuitively, the magnitude of the pressure load required to initiate fracture in this problem is expected to be independent of whether or not the pressure follows the crack evolution. After initiation, the pressure effects become important and the fracture propagates unstably. Due to this unstable behavior, it is very difficult to numerically capture the crack path after the pressure  $p_b$  is reached. In order to have a glimpse into what this path looks like, a viscous term  $\eta \dot{d}$  is added to the phase-field

equation, as in [92], with  $\eta = 10^{-3} \text{ mJ} \cdot \text{mm}^{-3} \cdot \text{s}$ .

It bears emphasis that the equations (2.10) and (3.22) indicate that, in the absence of any damage, the proposed model for pressurized cracks reduces to the standard phase-field fracture model for traction-free cracks. Therefore, one should expect the proposed model to capture fracture initiation properly in this scenario. On the other hand, for the (LVC) formulation, this only occurs if the indicator function satisfies  $I'(0) = 0$ . Among the many works which use the (LVC) formulation, only a few such as [45, 44] used an indicator function satisfying this condition. In [45], the authors were indeed able to predict fracture initiation from pressurized holes. To highlight the implications of having  $I'(0) \neq 0$  in the model (LVC), the results for this problem will also be presented using the (LVC) formulation with the indicator function  $I(d) = d$ .

The final damage patterns obtained using the (UVC) formulation and the (LVC) formulation are shown in Figure 2.7. With the (UVC) formulation, damage localizes along the midplane when the hoop stress is approximately 85% of  $\sigma_c$ . This is not unexpected, as the expression (2.78) is based on a one-dimensional state of stress and strain which differs significantly from the state near the corner of the hole. The same comparison is not performed for the simulation using the model (LVC), since damage forms only on the boundary in the first steps leading to spurious rigid body motion.

The main takeaway is that the proposed model (UVC) allows one to study crack nucleation and subsequent propagation under a pressure load, whereas formulation (LVC) leads to spurious damage formation if  $I'(0) \neq 0$ . The presence of the term  $p\nabla \cdot \mathbf{u}I'(d)$  in the damage equation (2.20) drives crack formation in areas which are not stressed. For this specific problem, this issue can be circumvented using for example  $I(d) = d^2$ , as shown in [45], but this option introduces a spurious dependence of the cohesive response of the material on the applied pressure, as indicated in the

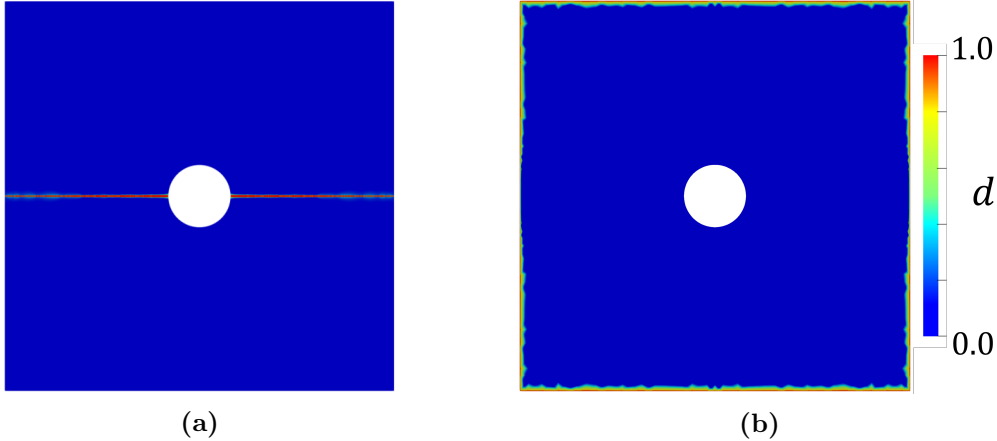


FIGURE 2.7. (a) Final crack pattern using proposed model; (b) Damage field using the model from [1].

last section (Figure 2.5b).

### 2.5.3 Stable propagation of a pre-existing crack

Consider a strip of material with a pressurized crack, as shown in Figure 2.8a. The rectangular strip has a width  $W$ , height  $H$  and a crack with initial size  $a$  (values provided in Table 2.3), and is loaded by the “surfing” boundary condition  $\widetilde{U}_y(x, y, t)$  on its top and bottom surfaces [88]. The boundary condition is given by

$$\widetilde{U}_y(x, y, t) = U_y(x - Vt, y), \quad (2.79)$$

where

$$U_y(x, y) = \hat{U}_y(r, \theta) = \frac{\sqrt{G_c E'}}{2\mu} \sqrt{\frac{r}{2\pi}} (\kappa - \cos \theta) \sin \frac{\theta}{2}, \quad (2.80)$$

and where  $r$  and  $\theta$  are polar coordinates with respect to the origin, taken to be the midpoint of the left edge of the domain. The constant  $V > 0$  is the target crack speed, prescribed by moving the boundary condition following (2.79). The Kolosov constant is defined as  $\kappa = 3 - 4\nu$  in plane strain and the shear modulus  $\mu = E/(2 + 2\nu)$ . The pressure  $p$  applied to the crack faces as the crack evolves is

given by

$$p = \frac{1}{2} \sqrt{\frac{G_c E'}{\pi a}}, \quad (2.81)$$

in which  $a$  denotes the initial crack length. This value corresponds to half the critical pressure for an infinite plate with a pressurized crack of size  $a$ . This magnitude ensures that the applied pressure is considerably large, but not so large as to drive the problem beyond the stable propagation regime.

To calculate the energy release rate, the domain form of the J-integral (2.44) developed in Section 2.3 is used. The function  $q$  is constructed by taking advantage of the finite element interpolation. In essence, the domain for the J-integral is taken to be a single rectangular region of dimensions  $a \times H/2$ , centered on the initial crack tip. The value of  $q$  for all nodes outside of this region is set to 0, while  $q = 1$  for all nodes inside. Using the finite element interpolation, this gives rise to a  $q$  function whose value changes continuously from 0 to 1 on the elements cut by the rectangular path. This function is illustrated in Figure 2.8b<sup>2</sup>.

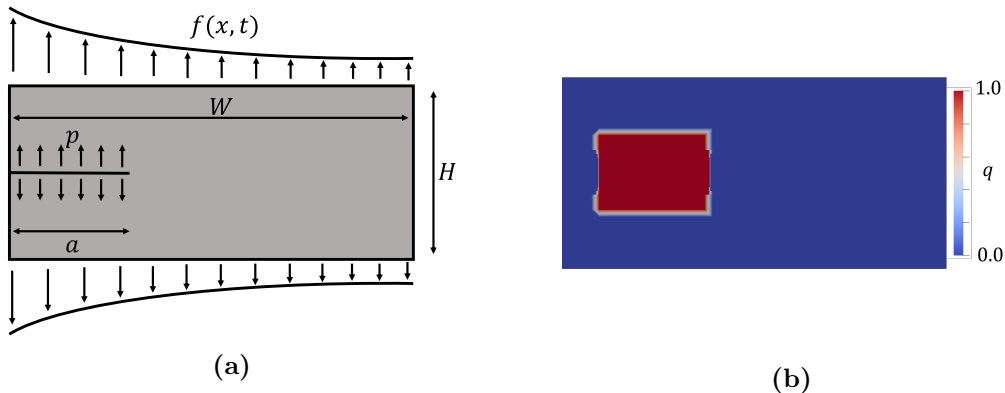


FIGURE 2.8. (a) Geometry and boundary conditions for pressurized crack propagation problem; (b) J-Integral domain function  $q$ .

---

<sup>2</sup> Due to mesh refinement near the crack surface, the width of the band where  $0 < q < 1$  diminishes near the horizontal centerline of the domain.

**Table 2.3.** Parameters used for pressurized crack propagation problem

	Value	Unit
Young's modulus ( $E$ )	$3.0 \times 10^4$	MPa
Poisson's ratio ( $\nu$ )	0.2	—
Critical fracture energy ( $G_c$ )	0.12	$\text{mJ mm}^{-2}$
Initial crack length ( $a$ )	1.6	m
Specimen width ( $W$ )	8.0	m
Specimen height ( $H$ )	4.0	m
Target crack speed ( $V$ )	0.4	m/s

In order to verify that Griffith's law is approached as  $\ell \rightarrow 0$ , simulations are performed for this problem using a sequence of decreasing regularization lengths, ranging from  $\ell = a/20$  to  $\ell = a/160$ . The mesh is locally refined along the  $x$ -axis, where the element size is set to  $h = \ell/4$ . The symmetry of the problem is exploited and only the response in the top half of the domain is simulated. In terms of constitutive choices of the phase-field model, the AT-1 formulation is employed without any decomposition of the strain. As in the previous examples, this problem is analyzed using the formulations (LVC) and (UVC), and the following choices of indicator function  $I(d)$ :

- $I(d) = d$
- $I(d) = d^2$
- $I(d) = 2d - d^2$

To evaluate how well the models approach Griffith's law, the ratio between the energy release rate measured by the J-Integral and the effective critical fracture energy  $G_c^{eff} = (1 + 2h/c_0\ell)G_c$ <sup>3</sup> is plotted in Figures 2.9 and 2.10. In all figures, the time is scaled by a characteristic time  $\tau$ , defined as  $\tau = a/V$ . The results

---

<sup>3</sup> in fact, phase-field cracks actually dissipated a slightly larger energy per unit length in numerical models. A correction factor of  $\left(1 + \frac{2h}{c_0\ell}\right)$  is then applied to  $G_c$ , following [80]. The factor of 2 here comes from the symmetry boundary condition employed.

using the traditional (LVC) formulation are presented in Figure 2.9. They indicate convergence towards  $J/G_c^{eff} = 1$  as the regularization length is reduced, especially when the indicator function  $I(d) = d$  is used. This is expected given the results obtained in [1]. Nevertheless, these results serve to verify the implementation of the J-Integral presented in Section 2.3. They also provide an estimate for how small the regularization length has to be in order to achieve a certain level of accuracy with these types of phase-field models.

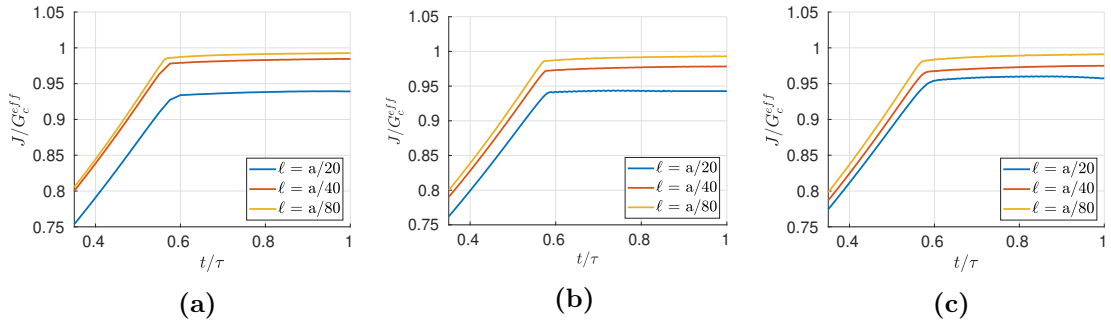


FIGURE 2.9. Reference results with the LVC formulation. Curves with  $\ell = a/160$  are not shown, as they are almost identical to the ones with  $\ell = a/80$ . (a)  $I(d) = d$ ; (b)  $I(d) = d^2$ ; (c)  $I(d) = 2d - d^2$

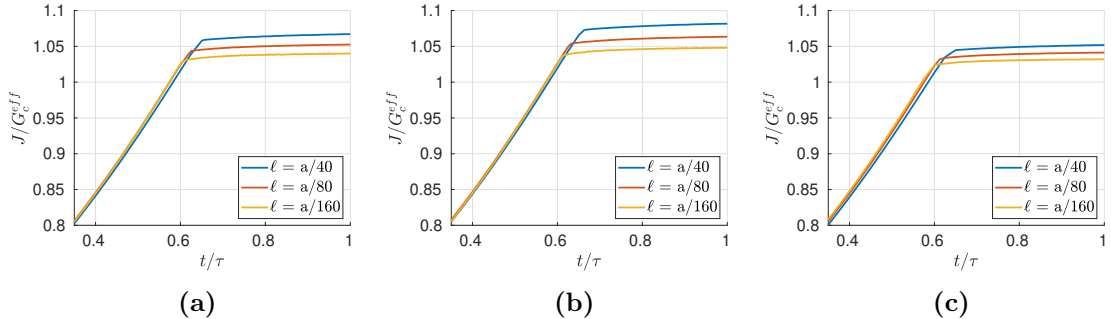


FIGURE 2.10. Results with the proposed formulation (UVC) (a)  $I(d) = d$ ; (b)  $I(d) = d^2$ ; (c)  $I(d) = 2d - d^2$

For the case of proposed formulation (UVC), the results shown in Figure 2.10 indicate a slower convergence towards a  $J/G_c^{eff} = 1$  response. In contrast with

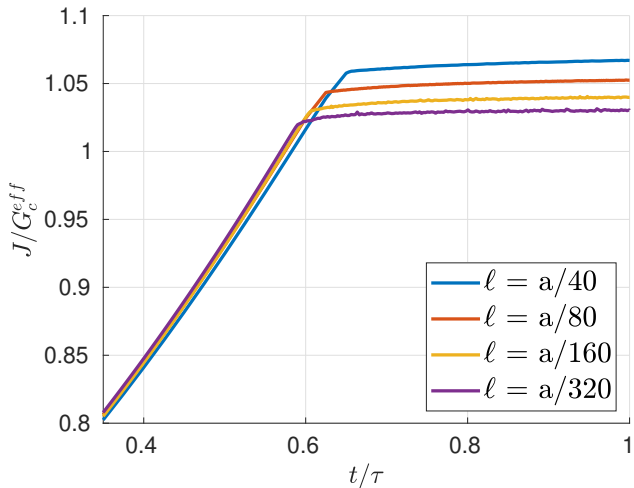


FIGURE 2.11. Convergence of the proposed formulation with  $I_{\text{problem}}$ , as a function of regularization length.

$\ell/a$	Error	$\text{Error}_{k+1}/\text{Error}_k$
1/40	0.067	—
1/80	0.052	0.78
1/160	0.040	0.77
1/320	0.031	0.77

the (LVC) formulation, the curves converge from above, and therefore, the fracture toughness is slightly overestimated when larger regularization lengths are used. Nevertheless, they all seem to approach a Griffith-like response in the limit  $\ell \rightarrow 0$ . In Figure 2.11, an even finer result, using (UVC) with  $I(d) = d$  and  $\ell = a/320$  is added, to ensure that the convergence rates indicated in Figure 2.10 persist. In Table 2.4, the relative errors are provided, indicating a convergence rate of approximately 0.4 with respect to  $\ell$ .

One potential explanation for the slower convergence rate is related to the different assumptions regarding the trial cracks, as discussed in Section 2.2. Although the different assumptions converge to the same propagation rule in the limit of an infinitesimal crack increment, in the discretized case, the minimal crack increment is finite and related to the mesh spacing  $h$  and regularization length  $\ell$ . In this case, a slightly different propagation behavior, resulting in slower convergence rates towards  $J/G_c^{eff} = 1$  is not surprising.

## 2.6 Concluding Remarks

This manuscript examines various models for phase-field fracture incorporating pressure loads on diffuse crack faces. This includes the analysis of a new formulation that can be obtained by considering the presence of the pressure load in the virtual extension of a crack, or alternatively through a careful accounting in the minimization procedure. The new formulation is referred to as the “unloaded virtual crack formulation” (UVC). In order to verify the accuracy of the various models for propagating cracks, a new form of the J-Integral for pressurized cracks in the phase-field context is derived.

The (UVC) formulation proposed herein allows for a unified treatment of crack nucleation and propagation in scenarios involving either brittle or cohesive fracture, and provides for better accuracy in some problems compared to existing formulations of the (LVC) type. As it allows for the use of the same governing equation for the damage parameter, its computational implementation within existing phase-field solvers is also simpler. In future work, its applicability to problems involving plastic deformation and strength-based fracture nucleation will be studied. In addition to that, modifications to accelerate the convergence of the model with respect to the phase-field parameter  $\ell$  will also be considered.

## 2.7 Acknowledgments

The partial support of A. Costa and J.E. Dolbow by the National Science Foundation, through grant CMMI-1933367 to Duke University, is gratefully acknowledged. Author T. Hu gratefully acknowledges the support of Argonne National Laboratory. Argonne National Laboratory is managed and operated by UChicago Argonne LLC. for the U.S. Department of Energy under Contract No. DE-AC02-06CH11357.

## 2.8 Equivalence to SIF condition

In this appendix, the energy release rate for a single, straight crack under an arbitrary pressure load  $p(x)$  is computed, assuming that infinitesimal crack increments are traction-free, as shown in Figure 2.2a. Griffith's criteria states that propagation should happen whenever this energy release rate, which will be denoted by  $G$ , reaches  $G_c$ . This will give rise to a condition for propagation based on the pressure distribution  $p(x)$ , the crack size  $a$  and Young's modulus  $E'$ <sup>4</sup>. The purpose of the following derivation is to demonstrate that this condition is equivalent to the stress intensity factor criteria [112].

Initially, consider the Sneddon-Lowengrub solution for the aperture of a pressure loaded crack in an infinite plate, under plane strain conditions,

$$w(x) = \frac{4a}{\pi E'} \int_0^1 p(sa) Z(x/a, s) ds \quad (2.82)$$

where

$$Z(r, s) = \log \left| \frac{\sqrt{1 - r^2} + \sqrt{1 - s^2}}{\sqrt{1 - r^2} - \sqrt{1 - s^2}} \right| \quad (2.83)$$

is a convolution kernel. The work done by the pressure load is then,

$$W_p = \int_{-a}^a p w dx = \int_{-a}^a p(y) \frac{4a}{\pi E'} \int_0^1 p(sa) Z(x/a, s) ds dy. \quad (2.84)$$

Clayperon's theorem [113] states that the potential energy is negative half of the work exerted in the boundary, which, in this case is only  $W_p$ . Hence

---

<sup>4</sup> assuming plane strain,  $E' = E/(1 - \nu^2)$

$$U = -\frac{1}{2}W_p = -\frac{1}{2} \int_{-a}^a p w dx = -\frac{4a^2}{\pi E'} \int_0^1 p(ar) \int_0^1 p(sa) Z(r, s) ds dr. \quad (2.85)$$

Let's write the energy release rate, assuming that the pressure field doesn't vary as the crack advances by a small amount  $da$ . That is,

$$p^{a+da}(x) = \begin{cases} p^a(x), & \text{if } x \leq a \\ 0, & \text{if } a \leq x \leq a + da \end{cases} \quad (2.86)$$

$$dU = U(a + da, p^{a+da}) - U(a + da, p^a), \quad (2.87)$$

$$dU = -\frac{4}{\pi E'} \int_0^{a+da} p^{a+da}(x) \int_0^{a+da} p^{a+da}(y) Z\left(\frac{x}{a+da}, \frac{y}{a+da}\right) dy dx + \frac{4}{\pi E'} \int_0^a p^a(x) \int_0^a$$

$$(2.88)$$

Using the definition of  $p^{a+da}$  given above,

$$dU = -\frac{4}{\pi E'} \int_0^a p^a(x) \int_0^a p^a(y) \left( Z\left(\frac{x}{a+da}, \frac{y}{a+da}\right) - Z(x/a, y/a) \right) dy dx. \quad (2.89)$$

By symmetry, both tips of the crack propagate with the same energy release rate, so, one can write,

$$2G = -\frac{dU}{da} = \frac{4}{\pi E'} \int_0^a p^a(x) \int_0^a p^a(y) \frac{1}{da} \left( Z\left(\frac{x}{a+da}, \frac{y}{a+da}\right) - Z(x/a, y/a) \right) dy dx.$$

$$(2.90)$$

The term between parenthesis can be re-written as,

$$\begin{aligned}
Z\left(\frac{x}{a+da}, \frac{y}{a+da}\right) - Z(x/a, y/a) &= \\
\log \left| \frac{\sqrt{(a+da)^2 - x^2} + \sqrt{(a+da)^2 - y^2}}{\sqrt{(a+da)^2 - x^2} - \sqrt{(a+da)^2 - y^2}} \right| - \log \left| \frac{\sqrt{a^2 - x^2} + \sqrt{a^2 - y^2}}{\sqrt{a^2 - x^2} - \sqrt{a^2 - y^2}} \right| \\
&= \log \left| \frac{\sqrt{(a+da)^2 - x^2} + \sqrt{(a+da)^2 - y^2}}{\sqrt{a^2 - x^2} + \sqrt{a^2 - y^2}} \right| \\
&\quad - \log \left| \frac{\sqrt{(a+da)^2 - x^2} - \sqrt{(a+da)^2 - y^2}}{\sqrt{a^2 - x^2} - \sqrt{a^2 - y^2}} \right|. \quad (2.91)
\end{aligned}$$

The second term contains a singularity, which can be removed if one re-writes it as,

$$\begin{aligned}
\log \left| \frac{\sqrt{(a+da)^2 - x^2} - \sqrt{(a+da)^2 - y^2}}{\sqrt{a^2 - x^2} - \sqrt{a^2 - y^2}} \right| &= \\
\log \left| \frac{\sqrt{(a+da)^2 - x^2} - \sqrt{(a+da)^2 - y^2}}{\sqrt{a^2 - x^2} - \sqrt{a^2 - y^2}} \frac{\sqrt{(a+da)^2 - x^2} + \sqrt{(a+da)^2 - y^2}}{\sqrt{a^2 - x^2} + \sqrt{a^2 - y^2}} \right| \\
&= \log \left| \frac{(a+da)^2 - x^2 - (a+da)^2 + y^2}{a^2 - x^2 - a^2 + y^2} \frac{\sqrt{a^2 - x^2} + \sqrt{a^2 - y^2}}{\sqrt{(a+da)^2 - x^2} - \sqrt{(a+da)^2 - y^2}} \right| \\
&\quad = -\log \left| \frac{\sqrt{(a+da)^2 - x^2} + \sqrt{(a+da)^2 - y^2}}{\sqrt{a^2 - x^2} + \sqrt{a^2 - y^2}} \right| \quad (2.92)
\end{aligned}$$

This expression can be plugged back into (2.91) to obtain,

$$\begin{aligned}
Z\left(\frac{x}{a+da}, \frac{y}{a+da}\right) - Z(x/a, y/a) &= \\
\log \left| \frac{\sqrt{(a+da)^2 - x^2} + \sqrt{(a+da)^2 - y^2}}{\sqrt{(a+da)^2 - x^2} - \sqrt{(a+da)^2 - y^2}} \right| - \log \left| \frac{\sqrt{a^2 - x^2} + \sqrt{a^2 - y^2}}{\sqrt{a^2 - x^2} - \sqrt{a^2 - y^2}} \right| \\
&= 2 \log \left| \frac{\sqrt{(a+da)^2 - x^2} + \sqrt{(a+da)^2 - y^2}}{\sqrt{a^2 - x^2} + \sqrt{a^2 - y^2}} \right|. \quad (2.93)
\end{aligned}$$

Hence,

$$\frac{1}{da} \left( Z\left(\frac{x}{a+da}, \frac{y}{a+da}\right) - Z(x/a, y/a) \right) = \frac{2}{da} \log \left| \frac{\sqrt{(a+da)^2 - x^2} + \sqrt{(a+da)^2 - y^2}}{\sqrt{a^2 - x^2} + \sqrt{a^2 - y^2}} \right|. \quad (2.94)$$

Now, the terms in the numerator can be expanded with a Taylor series,

$$\sqrt{(a+da)^2 - x^2} = \sqrt{a^2 - x^2} + \frac{a}{\sqrt{a^2 - x^2}} da + O(da^2), \quad (2.95)$$

leading to,

$$\begin{aligned} \frac{1}{da} \left( Z\left(\frac{x}{a+da}, \frac{y}{a+da}\right) - Z(x/a, y/a) \right) &= \\ &= \frac{2}{da} \log \left| \frac{\sqrt{a^2 - x^2} + \frac{a}{\sqrt{a^2 - x^2}} da + O(da^2) + \sqrt{a^2 - y^2} + \frac{a}{\sqrt{a^2 - y^2}} da + O(da^2)}{\sqrt{a^2 - x^2} + \sqrt{a^2 - y^2}} \right|, \end{aligned} \quad (2.96)$$

which, after using a Taylor expansion, simplifies to,

$$\frac{1}{da} \left( Z\left(\frac{x}{a+da}, \frac{y}{a+da}\right) - Z(x/a, y/a) \right) = \frac{2a}{\sqrt{a^2 - x^2} \sqrt{a^2 - y^2}} + O(da). \quad (2.97)$$

Now, we can finally go back to the energy release rate,

$$\begin{aligned} 2G = -\frac{dU}{da} &= \frac{4}{\pi E'} \int_0^a p^a(x) \int_0^a p^a(y) \frac{2a}{\sqrt{a^2 - x^2} \sqrt{a^2 - y^2}} dy dx = \\ &= \frac{8a}{\pi E'} \int_0^1 \frac{p^a(ar)}{\sqrt{1 - r^2}} \int_0^1 \frac{p^a(as)}{\sqrt{1 - s^2}} ds dr = \frac{8a}{\pi E'} \left( \int_0^1 \frac{p^a(as)}{\sqrt{1 - s^2}} ds \right)^2. \end{aligned} \quad (2.98)$$

From [114], the stress intensity factor under these same conditions is,

$$K_I = 2\sqrt{\frac{a}{\pi}} \left( \int_0^1 \frac{p^a(as)}{\sqrt{1-s^2}} ds \right) \quad (2.99)$$

From a simple inspection, one can see that  $G = K_I^2/E'$ , which guarantees the equivalence of the energy release rate criteria under the assumption in Figure 2.2a and the stress intensity factor condition. If instead, one assumes that the pressure load in the vicinity of a propagating crack behaves as in Figure 2.2b, this equivalence between the energetic criteria and the stress intensity factor may be violated.

# 3

## A Multi-Resolution Approach for Hydraulic Fracture Simulation

### 3.1 Introduction

A wide range of approaches for model-based simulations of hydraulic fracturing have been developed over the past several decades [2, 115]. These range from production-level reservoir modeling tools such as ResFrac[? ? ], to GEOS[? ? 116], PyFrac[? ], and others. Many of the models and associated codes assume fracture networks that remain planar, but in recent years strides have been made towards modeling cracks that evolve in arbitrary ways in response to fluid-driven loads. High-resolution models for complex fracture evolution generally fall into two categories: sharp interface models that explicitly model the fracture surface, and diffuse crack approaches that effectively smear the geometry over the underlying grid or mesh. Techniques that represent the crack as a sharp interface can be advantageous when the fracture configuration is relatively simple, but representing complex geometric evolution can be challenging [117, 118? ]. By contrast, diffuse crack models offer more flexibility for representing complex fracture evolution, but introduce other challenges such as

the lack of a well-defined fracture surface and increased computational expense[83]. In this work, we introduce a multi-resolution scheme for hydraulic fracturing simulation that makes use of both sharp and diffuse crack representations within a single framework. The objective is to establish a methodology that makes use of the advantageous aspects of both sharp and diffuse crack models while circumventing some of the drawbacks.

Over the past several decades, the phase-field model for fracture [48, 41, 47] has emerged as a promising approach for constructing robust simulations of complex crack evolution. The method has shown considerable success for simulating fracture evolution in quasi-brittle materials, and there have been several recent efforts to extend the approach to hydraulic fracturing. In what follows, we review some prior works of particular relevance to the current manuscript. For additional references in this topic, we refer the reader to the recent review by Heider [83].

The first attempts towards a phase-field model for hydraulic fracture began with extensions of the traditional phase-field model to pressurized cracks, as in Bourdin et al. [1] and Wheeler et al. [42]. Subsequently, fluid flow in the fractures, and also poromechanics were considered. Miehe et al. [119, 51] developed a thermodynamically consistent framework, from minimization principles, to couple poromechanics, fluid-flow and phase-field fracture. The flow problem was modeled via the Darcy's equation, containing a permeability coefficient that used the phase-field variable and the crack opening to mimic the cubic relationship from the lubrication theory in the crack region. Mikelic et al. [56, 120] developed a model that separated the domain into fracture and reservoir, by using the phase-field variable as an indicator function. They also considered the flow inside the fracture as a Darcy flow, but their model treated the fracture as a three-dimensional entity, which led to a different permeability tensor compared to [119, 51]. Yet another approach concerns the work of Wilson and Landis [54], who proposed a model that included fluid velocities as

primary variables. This allowed for a more detailed description of the flow within the fracture, which was modeled by a Brinkman-type equation [? ]. The phase-field parameter acted as an indicator of the flow regime, between Darcy flow (away from cracks) and Stokes flow (inside cracks). Finally, the recent work of Chukwudzie et al. [55] presented a different model, wherein the lubrication theory equations were included in the weak form by means of a  $\Gamma$ -convergent regularization.

The use of a phase-field to represent a fracture network in a diffuse manner certainly facilitates the representation of complex geometric evolution, including crack branching and merging. However, it also requires the use of meshes or grids that are capable of resolving the regularization length, making these approaches computationally expensive. One approach to improving the efficiency of the method is the use of adaptive mesh refinement, such as in [105? ? ? ]. In the specific case of hydraulic fracturing, another challenge concerns the crack opening or aperture, a field that is tightly coupled with the fluid pressure within fractures. In a phase-field setting, due to the lack of an explicit crack surface, extracting the aperture or accounting for its effects requires additional considerations. All of the aforementioned works present some way to account for the aperture within a diffuse setting, but the robustness of these approaches remains unclear [115]. For a review of the most frequently used methods to calculate the crack aperture from phase-field simulations, see the recent work of Yoshioka et al. [80].

Outside of the context of hydraulic fracturing, some researchers in the phase-field community have developed “hybrid” approaches, wherein the phase-field formulation was combined with a sharp crack representation. The motivation for these approaches varies, from “cutting” the mesh to remove artificial traction transmission and circumvent element distortion [121] to reducing the overall computational cost [122, 123]. In the work of Giovanardi et al. [122], phase-field subproblems in the vicinity of crack tips were used to propagate a global, discrete crack. The eXtended

Finite Element Method (XFEM)[124] was used to place fracture discontinuities in the displacement field within the background global mesh. More recently, Muixi et al. [123] created an approach that uses the phase-field method only at the crack tips, and XFEM in the rest of the domain. In contrast to [122], there is no overlap of the representations in crack tip areas.

The success of these hybrid approaches for purely mechanical cases opens the door for their extension to hydraulic fracturing. Such approaches are appealing because in principle they can circumvent the need for a complicated reconstruction of the crack opening from the phase-field. This area is relatively unexplored, although there have been some recent efforts that are similar in spirit, such as the recent work of Sun et al. [125]. They developed a Finite Element-Meshfree method to represent the crack surfaces in a discrete fashion. The computed displacement field was used to obtain a driving force which was employed within a phase-field evolution equation near the crack tips. This approach eliminated the need for the reconstruction of crack openings from the diffuse crack representation, but it also largely decoupled the phase field from the equations governing the force balance near the crack tips.

The approach presented in this work, which we refer to as a multi-resolution method, extends the concept of a hybrid phase-field method to hydraulic fracturing. It discretizes the problem at a global level using a sharp interface approach based on the Embedded Finite Element Method of Cusini et al. [126]. It then approaches the simulation of fracture evolution by coupling the global fields with a phase-field fracture problem posed over a subdomain in the vicinity of the crack front. This approach has several advantages. The crack aperture and flow inside the fracture are handled at the global scale using techniques that work well and are efficient when the crack geometry is known. Then the phase-field model is employed in the subdomain to effectively update the crack geometry. This framework lends itself to incorporation with a wide range of existing hydraulic fracturing solvers, as the

phase-field sub-problem is agnostic about the type of numerical treatment used in the global domain. In the current work, we adopt relatively simple assumptions regarding material behavior, such as small deformations and linear poroelasticity, as they allow us to verify our scheme against analytical solutions. However, in principle the approach could be extended to model crack growth in a much broader class of poroelastic materials, such as hydrogels [? ].

The paper is structured as follows. In Section 3.2, we present the governing equations and constitutive assumptions for both hydraulic fracturing and phase-field for fracture. In Section 3.3, we propose our multi-resolution framework and present numerical schemes to discretize both the hydrofracture and the phase-field subproblems. In Section 3.4, we apply our method to study hydraulic fracturing in some simple scenarios, in order to verify its accuracy. These include the well-known KGD[127, 128] problems and a case of non-planar fracture propagation around a stiff inclusion. Finally, in Section 5, we provide a summary and some concluding remarks.

## 3.2 Model formulation

In this section, we describe the models that are used to develop our multi-resolution scheme. We start by presenting the governing equations to model hydraulic fracture in poroelastic rock that forms the basis for the solver at the global scale. We then describe a phase-field model for fracture that forms the basis for the solver used in local subdomains near the crack tips.

### 3.2.1 Governing equations for hydraulic fracture

We consider a model that couples flow and elastic deformation in a porous media with evolving fracture surfaces. Consider the domain  $\Omega$  consisting of a porous rock, that is fully saturated with a single-phase Newtonian fluid. The external boundary is composed of both traction  $\partial\Omega_t$  and displacement  $\partial\Omega_u$  surfaces, viz.  $\partial\Omega = \partial\Omega_t \cup \partial\Omega_u$ .

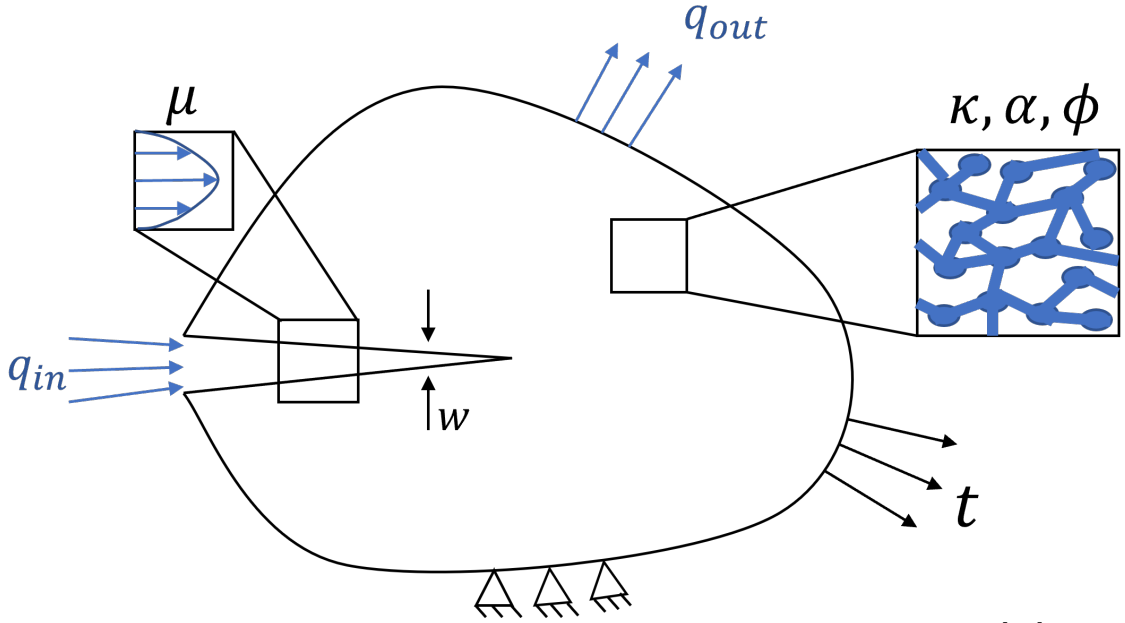


FIGURE 3.1. Schematic of a poroelastic rock with a fracture, inspired by [? ].

The domain contains fractures  $\Gamma$ , as shown in Figure 3.1. For simplicity, we assume quasi-static conditions and small-strain kinematics. Neglecting inertial effects, the balance of linear momentum reads

$$\nabla \cdot \boldsymbol{\sigma} + \mathbf{b} = \mathbf{0} \text{ on } \Omega \setminus \Gamma, \quad (3.1)$$

where  $\boldsymbol{\sigma}$  denotes the total Cauchy stress and  $\mathbf{b}$  the body force. The mechanical boundary conditions are given by

$$\boldsymbol{\sigma} \cdot \mathbf{n} = \mathbf{t} \text{ on } \partial\Omega_t, \quad (3.2)$$

$$\mathbf{u} = \bar{\mathbf{u}} \text{ on } \partial\Omega_u, \quad (3.3)$$

where  $\mathbf{n}$  denotes the normal direction at any point on  $\partial\Omega$ ,  $\mathbf{t}$  are the applied tractions, and  $\bar{\mathbf{u}}$  denotes the prescribed displacements.

Fluid flow within the cracks gives rise to pressure loads on the crack surfaces,

translating into the boundary condition

$$\boldsymbol{\sigma}^+ \cdot \mathbf{n}_\Gamma = -\boldsymbol{\sigma}^- \cdot \mathbf{n}_\Gamma = -p_f \mathbf{n}_\Gamma \text{ on } \Gamma, \quad (3.4)$$

where  $p_f$  is the pressure inside the crack and  $\mathbf{n}_\Gamma$  is the normal vector to  $\Gamma$  at any point. In this work, we assume that fractures are open and neglect contact conditions on crack faces. For additional considerations to account for closed fractures, see the model described in Cusini et al.[126].

In terms of the fluid flow, the fluid velocity  $\mathbf{v}_m$  in the matrix is governed by the mass balance

$$\frac{\partial(\rho\phi)}{\partial t} + \nabla \cdot (\rho\mathbf{v}_m) = Q_m + Q_{mf} \text{ on } \Omega \setminus \Gamma. \quad (3.5)$$

where  $\rho$  denotes the fluid density and  $\phi$  is the porosity, and  $Q_m$  is a prescribed source term in the matrix. The source term  $Q_{mf}$  accounts for the exchange of fluid between the matrix and the fractures. The boundary is partitioned into pressure  $\partial\Omega_p$  and flux  $\partial\Omega_q$  portions, such that  $\partial\Omega = \partial\Omega_p \cup \partial\Omega_q$ , and the following boundary conditions are applied,

$$\rho\mathbf{v}_m \cdot \mathbf{n} = \mathbf{q} \text{ on } \partial\Omega_q, \quad (3.6)$$

$$p_m = \bar{p}_m \text{ on } \partial\Omega_p, \quad (3.7)$$

where  $p_m$  denotes the pore-pressure and  $\bar{p}_m$  is a prescribed pressure.

In a comparable manner, the fluid velocity  $\mathbf{v}_f$  within fractures is governed by the mass balance

$$\frac{\partial(\rho w)}{\partial t} + \nabla_\Gamma \cdot (\rho w \mathbf{v}_f) = Q_f + Q_{fm} \text{ on } \Gamma, \quad (3.8)$$

where  $w$  denotes the normal fracture aperture,  $Q_f$  is a prescribed source term within the fracture, and  $Q_{fm}$  accounts for the exchange of fluid between the fracture and

the matrix<sup>1</sup>. In the above,  $\nabla_\Gamma$  indicates a gradient operator taken on the lower dimensional manifold  $\Gamma$ . Boundary conditions similar to (3.6) and (3.7) can also be applied.

Constitutive relationships are required to close the system and tie the stresses to the displacements  $\mathbf{u}$  and the fluid velocities to the pressures. In particular, we adopt the basic assumptions of Biot's theory of poroelasticity [130], Darcy's law for the flow in the matrix, and a lubrication theory approximation for the flow in fractures. This gives rise to the following set of constitutive relationships for the stress, porosity, and velocities:

$$\boldsymbol{\sigma} = \mathbb{C} : \boldsymbol{\epsilon}(\mathbf{u}) - \alpha p_m \mathbb{I} \text{ on } \Omega \setminus \Gamma, \quad (3.9)$$

$$\dot{\phi} = \alpha \nabla \cdot \dot{\mathbf{u}} + \frac{\dot{p}_m}{N} \text{ on } \Omega \setminus \Gamma, \quad (3.10)$$

$$\mathbf{v}_m = -\frac{\kappa}{\mu} \nabla p_m \text{ on } \Omega \setminus \Gamma, \quad (3.11)$$

$$\mathbf{v}_f = -\frac{w^2}{12\mu} \nabla_\Gamma p_f \text{ on } \Gamma. \quad (3.12)$$

In the above,  $p_m$  is the pore-pressure,  $\mathbb{C}$  is the fourth-order isotropic tensor of drained elastic moduli,  $\boldsymbol{\epsilon}(\mathbf{u})$  is the mechanical strain,  $\alpha$  is the Biot coefficient, and  $\mathbb{I}$  is the second-order identity tensor. The temporal evolution of the porosity is governed by the rate of dilatation and time rate of change in the pore pressure, as modulated by the modulus  $N$ . The fluid velocity in the matrix is related to the gradient of the pressure through the ratio of the intrinsic permeability  $\kappa$  to the viscosity  $\mu$ .

---

<sup>1</sup> the flux interactions  $Q_{fm}$  and  $Q_{mf}$  are modeled as in classical well models, following [129]. This ensures the balance of mass between the fractures and matrix  $\int_V Q_{mf} dV = - \int_\Gamma Q_{fm} d\Gamma$ .

The fluid is assumed to be linearly compressible. For both the fluid in the fractures and the matrix, this implies that the density is updated from its reference value  $\rho_{ref}$  based on the change in pressure according to

$$\rho = \rho_{ref} \left( 1 + \frac{p - p_{ref}}{K_F} \right) \text{ on } \Omega, \quad (3.13)$$

where  $p_{ref}$  denotes a reference value for the pressure, and  $K_F$  is the fluid bulk modulus.

Finally, the initial conditions for the displacements and pressures are given by

$$\mathbf{u}(\mathbf{x}, 0) = \mathbf{u}^0 \text{ on } \Omega \setminus \Gamma, \quad (3.14)$$

$$p_m(\mathbf{x}, 0) = p_m^0 \text{ on } \Omega \setminus \Gamma, \quad (3.15)$$

$$p_f(\mathbf{x}, 0) = p_f^0 \text{ on } \Gamma. \quad (3.16)$$

For a given crack geometry, the combination of equations (3.1), (3.5) and (3.8), with constitutive assumptions (3.9) - (3.13), boundary conditions (3.2)-(3.4),(3.6),(3.7) and initial conditions (3.14)-(3.16) leads to a system of equations whose solution can be approximated by many different numerical methods. What remains is a model to describe the evolution of the crack geometry.

In the context of standard sharp interface approaches for hydraulic fracture, the evolution of the crack geometry is typically governed by a set of criteria that dictate whether or not a crack front extends and, if so, in what orientation. For crack extension, a standard approach is to adopt Griffith's criteria [131], which states that crack propagation should occur when the energy release rate  $G$  reaches the critical value  $G_c$  for the material, i.e.  $G \leq G_c$ . In terms of changes to orientation, several

different criteria are typically employed, such as the maximum hoop stress criteria [? ? ?] or the maximum energy release rate condition [? ? ?]. Examples of works from the hydraulic fracture field employing such criteria include [? ? ?].

Although such methods have seen some success in simulating the propagation of hydraulically-driven cracks, even in three dimensions [117, 118?], they struggle as crack evolution becomes sufficiently complex. By contrast, regularized methods have seen far more success in treating complex geometric evolution. In the next subsection, we present the governing equations for a phase-field method for fracture, a regularized approach for representing fractures and their evolution. Phase-field for fracture models generally start from a single energetic postulate that generalizes Griffith's criteria, and which is able to describe the entire fracture propagation process.

### 3.2.2 The phase-field method for fracture

The phase-field method for fracture started as an approximation [41] to the variational approach for fracture by Francfort and Marigo [48] for the quasi-static propagation of fracture in brittle materials. This model essentially states that a crack should evolve in a way that minimizes a total energy functional, among all admissible states, which are those that contain the current crack set (so that no healing is possible). For the method adopted in this work, we follow the work of Chukwudozie et al. [55] and associate the following total energy to a crack configuration  $\Gamma$  in a poroelastic brittle solid  $\Omega$ : where the tractions applied to the boundary are denoted by  $\mathbf{t}$ , the normal to the crack is denoted by  $\mathbf{n}_\Gamma$  and  $\mathcal{H}^{n-1}(\Gamma)$  is the  $n - 1$  dimensional Hausdorff measure of  $\Gamma$ .

The strain energy density  $W(\boldsymbol{\epsilon}(\mathbf{u}), p_m)$  is postulated as,

$$W(\boldsymbol{\epsilon}(\mathbf{u}), p_m) = \frac{1}{2} \left( \boldsymbol{\epsilon}(\mathbf{u}) - \frac{\alpha}{nK} p_m \mathbb{I} \right) : \mathbb{C} : \left( \boldsymbol{\epsilon}(\mathbf{u}) - \frac{\alpha}{nK} p_m \mathbb{I} \right), \quad (3.17)$$

with  $K$  denoting the bulk modulus and  $n$  the system's dimension (2 or 3). The phase-field regularization, based on the Ambrosio-Tortorelli [13] functional is then performed by the introduction of the damage parameter  $d$  and the regularization length  $\ell$ ,

$$\begin{aligned} \mathcal{E}_\ell(\mathbf{u}, d, p_m, p_f) = & \int_{\Omega} \widetilde{W}(\boldsymbol{\epsilon}(\mathbf{u}), p_m, d) d\Omega - \int_{\partial\Omega_N} \mathbf{t} \cdot \mathbf{u} ds - \int_{\Omega} \mathbf{b} \cdot \mathbf{u} d\Omega + \int_{\Omega} p_f \mathbf{u} \cdot \nabla d d\Omega \\ & + \frac{G_c}{c_0} \int_{\Omega} \left( \frac{\zeta(d)}{\ell} + \ell \nabla d \cdot \nabla \zeta(d) \right) d\Omega, \end{aligned}$$

where the function  $\zeta(d)$  is the local dissipation function, which is usually taken as  $\zeta(d) = d$  or  $d^2$ . The constant  $c_0$  is given by  $c_0 = 4 \int_0^1 \sqrt{\zeta(z)} dz$  and the regularized strain energy is defined by,

$$\widetilde{W}(\boldsymbol{\epsilon}(\mathbf{u}), p_m, d) = \frac{1}{2} \left( (1-d)\boldsymbol{\epsilon}(\mathbf{u}) - \frac{\alpha}{nK} p_m \mathbb{I} \right) : \mathbb{C} : \left( (1-d)\boldsymbol{\epsilon}(\mathbf{u}) - \frac{\alpha}{nK} p_m \mathbb{I} \right), \quad (3.19)$$

which is consistent with an assumption of damage arising in the sub pore scale [55]. Finally, our regularized crack evolution problem is then stated as a minimization principle for the functional  $\mathcal{E}_\ell(\mathbf{u}, d, p_m, p_f)$ , with respect to the variables  $\mathbf{u}$  and  $d$ , with the added condition that the damage process is irreversible and that the damage variable  $d$  is bounded between the values of zero (undamaged state) and unity (fully broken state):

$$\mathbf{u}, d = \underset{\mathbf{u}, d}{\operatorname{argmin}} \mathcal{E}_\ell(\mathbf{u}, d, p_m, p_f), \text{ subject to } \dot{d} \geq 0, \text{ and } 0 \leq d \leq 1. \quad (3.20)$$

The following set of evolution equations can then be derived from the Karush–Kuhn–Tucker (KKT) [103, 104] conditions:

$$\nabla \cdot ((1-d)^2 \mathbb{C} : \boldsymbol{\epsilon}(\mathbf{u}) - (1-d)\alpha p_m \mathbb{I}) + \mathbf{b} = p_f \nabla d, \quad (3.21)$$

$$S_d := \frac{2G_c\ell}{c_0} \Delta d - \frac{G_c}{c_0\ell} \zeta'(d) - g'(d)W(\boldsymbol{\epsilon}(\mathbf{u}), 0) + \alpha p_m \nabla \cdot \mathbf{u} + \nabla \cdot (p_f \mathbf{u}) \leq 0, \quad (3.22)$$

$$\dot{d} \geq 0, \quad (3.23)$$

$$0 \leq d \leq 1, \quad (3.24)$$

$$S_d \dot{d} = 0, \quad (3.25)$$

with boundary conditions,  $\boldsymbol{\sigma} \cdot \mathbf{n} = \mathbf{t}$  on  $\partial\Omega_N$  and  $(2G_c\ell \nabla d + c_0 p_f \mathbf{u}) \cdot \mathbf{n} \geq 0$  on  $\partial\Omega$ . The damaged stress is defined as  $\boldsymbol{\sigma} = (1-d)^2 \mathbb{C} : \boldsymbol{\epsilon}(\mathbf{u}) - (1-d)\alpha p_m \mathbb{I}$ .

In some cases, it is useful to decompose the energy (3.19) into positive and negative parts, in order to provide asymmetry between tension and compression states. In most problems studied in this manuscript, we found this decomposition to be important, and, unless otherwise mentioned, the spectral decomposition introduced in Miehe et al. [92] is used. With this decomposition, the equations for the macro-scale force balance (3.21) and the micro-force balance (3.22) are modified as

$$\nabla \cdot ((1-d)^2 \mathbb{C} : \boldsymbol{\epsilon}^+(\mathbf{u}) + \mathbb{C} : \boldsymbol{\epsilon}^-(\mathbf{u}) - (1-d)\alpha p_m \mathbb{I}) + \mathbf{b} = p_f \nabla d, \quad (22a)$$

$$S_d := \frac{2G_c\ell}{c_0} \Delta d - \frac{G_c}{c_0\ell} \zeta'(d) - g'(d)W(\boldsymbol{\epsilon}^+(\mathbf{u}), 0) + \alpha p_m \nabla \cdot \mathbf{u} + \nabla \cdot (p_f \mathbf{u}) \leq 0, \quad (23a)$$

and the damaged stress becomes  $\boldsymbol{\sigma} = (1-d)^2 \mathbb{C} : \boldsymbol{\epsilon}^+(\mathbf{u}) + \mathbb{C} : \boldsymbol{\epsilon}^-(\mathbf{u}) - (1-d)ap_m\mathbb{I}$ . In the above,  $\boldsymbol{\epsilon}^+$  and  $\boldsymbol{\epsilon}^-$  denote the positive and negative parts of the strain tensor as described in [92].

Finally, to close this section, we note that the extent to which the solution to (3.20) approaches a particular sharp model in hydraulic fracture in the limit as the regularization length  $\ell \rightarrow 0$  has yet to be established. Nevertheless, the particular phase-field model adopted here contains all of the requisite components to allow for a proof of concept of the multi-resolution approach.

### 3.3 Multi-resolution method

#### 3.3.1 General overview

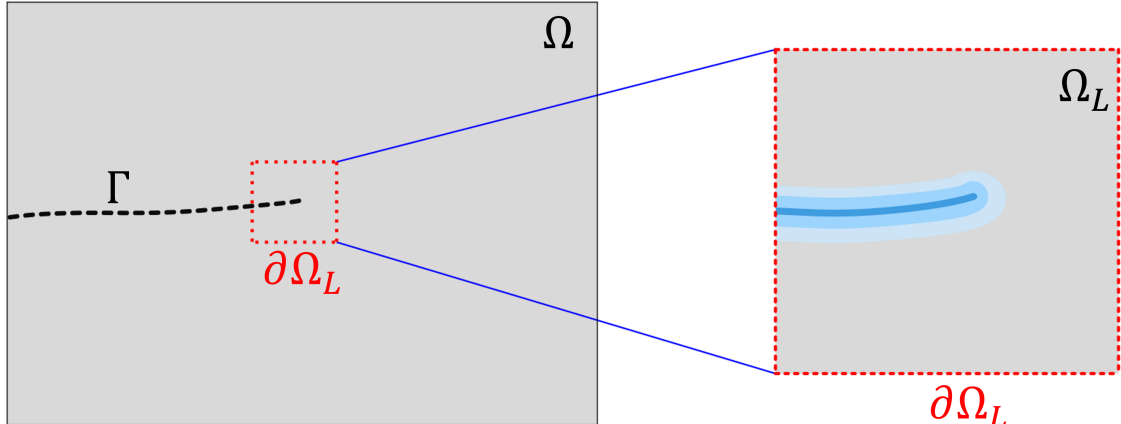


FIGURE 3.2. Global domain  $\Omega$  on the left and local domain  $\Omega_L$  on the right. The surface corresponding to the local domain boundary  $\partial\Omega_L$  is indicated within the global domain with the dashed red lines. The local domain is magnified to highlight the phase-field representation of the global crack  $\Gamma$ .

We propose a multi-resolution method to approximate the solution of the hydraulic fracture problem in porous media. It consists of coupling two problems between a global domain and a local subdomain, as shown in Figure 3.2. In the global domain problem, the governing equations (3.1)-(3.8) are discretized, and the crack is represented with a sharp geometry. The crack geometry is assumed to be

fixed during a solution step in the global domain, and relevant fields are calculated over the entire domain.

By contrast, the local subdomain concerns only a portion of the entire domain, namely in the vicinity of crack tips. It is encapsulated within the global domain as shown in Figure 3.2. In the local subdomain, a discretization of the variational principle (3.20) is used to simulate crack evolution. During a solution step in the local subdomain, the pressure fields within the fracture and matrix are assumed to be fixed.

The two problems are coupled in the following manner. The displacement and pressure fields are extracted from a solution step in the global domain and passed to the local subproblem in different ways. In particular, the global displacement fields are extracted along the surface  $\partial\Omega_L$ . These fields are then applied as Dirichlet boundary conditions for the local subproblem. The matrix pressure  $p_m$  and pressure in the fracture  $p_f$  are transferred as fields from the global domain to the local subdomain (see Section 3.3.3.2 for details), and assumed to be fixed for the local subproblem.

The aforementioned operations provide everything that is needed for the local subproblem from the global domain. Based on the imprint of the global crack geometry on the local subdomain, a regularized fracture surface is created (through an initial damage field) and then crack propagation is simulated in the local subdomain. Once an extension of the crack in a scale that can be represented in the global domain is identified, the sharp crack geometry in the global problem is updated accordingly.

In principle, the aforementioned multi-resolution approach can be implemented using a number of different discretization methods in the global domain and the local subdomain. In the sections that follow, we describe the particular choices used in this work as well as some important implementation details. The method is described in a two-dimensional context, but many aspects can be readily extended

to three-dimensional problems.

### 3.3.2 Global problem discretization

The global problem in our multi-resolution approach encompasses the physics of fluid flow in both the fractures and the pore structure of our domain, as well as the deformation of the solid media. The set of governing equations consists of (3.1)-(3.8), combined with constitutive assumptions (3.9)-(3.13) and appropriate boundary conditions.

In this work, we use the discretization method proposed by Cusini et al. [126] in the study of fluid flow in fractured porous media. The domain  $\Omega$  is partitioned with a mesh  $\mathcal{T}$ . Then, the intersection of the fracture network  $\Gamma$  with  $\mathcal{T}$  defines the fracture triangulation  $\mathcal{F}$ . These meshes are then used to define discrete counterparts  $\mathbf{u}_G^h$ ,  $p_m^h$  and  $p_f^h$  of the unknown fields  $\mathbf{u}$ ,  $p_m$  and  $p_f$ , as well as discrete approximations of equations (3.1), (3.5) and (3.8).

A finite element approximation is constructed for the displacement field and employed in a standard Galerkin approximation to the global force balance (3.1). The continuous part of the displacement field is approximated with a standard space  $\mathcal{U}$  of 4-node bilinear shape functions  $\{\boldsymbol{\eta}_a\}$ . In the subset of elements that are “cut” by the global crack geometry, a space  $\mathcal{W}$  of discontinuous enrichment functions  $\{\boldsymbol{\phi}_b\}$  is constructed using the formulation described in [132].

The full displacement field in the global problem is constructed using both continuous and discontinuous parts as

$$\mathbf{u}_G^h = \underbrace{\sum_{a=1}^{n_u} u_a \boldsymbol{\eta}_a}_{\text{continuous part}} + \underbrace{\sum_{b=1}^{n_w} w_b \boldsymbol{\phi}_b}_{\text{discontinuous part}}, \quad (3.26)$$

where  $\{u_a\}$ ,  $\{w_b\}$  are scalar degrees of freedom.

The flow equations (3.5) and (3.8) are discretized with a finite-volume method. Piecewise-constant pressure fields are constructed for  $p_m^h$  and  $p_f^h$  over the matrix mesh  $\mathcal{T}$  and the fracture mesh  $\mathcal{F}$ , respectively. Fluxes are computed using a two point flux approximation. The interaction between the flow in the fracture and matrix is effected via the embedded discrete fracture model (EDFM) [133, 129].

In terms of the temporal discretization, the parabolic nature of equations (3.5) and (3.8) gives rise to a stable time step for explicit schemes that scales with the cube of the mesh spacing [2, 115]. This upper bound is prohibitively small in most cases. Therefore, an implicit backward Euler method is used throughout. This gives rise to a fully-coupled system of nonlinear equations, whose solution is obtained with a Newton method, in a monolithic fashion.

One limitation of the construction (3.26) is that the discontinuous enrichment functions are not capable of representing a crack tip that terminates inside of an element. As such, any new extension of the crack geometry has to traverse from one side of a new element to another. The implementation of the fracture flow solver requires all cells to have non-zero volumes. Accordingly, new fracture cells are assigned a small aperture value ( $w_0$ ). The total discrete aperture of the cell is thus given by  $w_h = w_n + w_0$ , where  $w_n$  is the mechanical aperture that is consistent with the jump provided by the displacement field. The minimum opening  $w_0$  has been interpreted as a representation of the roughness of the fracture surfaces, providing a pathway for fluid flow even when the cracks are mechanically closed. See, for example [126].

### 3.3.3 Local problem initialization

#### 3.3.3.1 Construction of subdomain, submesh and damage-fixed nodes

A local subdomain of size  $L \times L$  is constructed by simply centering it on a global crack tip. The size  $L$  is selected to be an even integer multiplier of the global mesh

spacing, leading to a square bounding box that conforms to the background mesh. This choice is adopted for convenience in this work, although other constructions are possible, such as in [122].

To obtain the submesh  $\mathcal{T}_L$ , we start by considering the restriction of the global triangulation  $\mathcal{T}$  to the subdomain  $\Omega_L$ . The mesh for the local subdomain is constructed by uniformly refining the set of elements in this restriction. This facilitates the transfer of nodal data from the global to the local problem. The mesh size  $h_{local}$  in the local subdomain is chosen to be sufficiently small to resolve the damage band, of size  $\mathcal{O}(\ell)$ . In this work, we use  $\ell/h_{local} \approx 4$ .

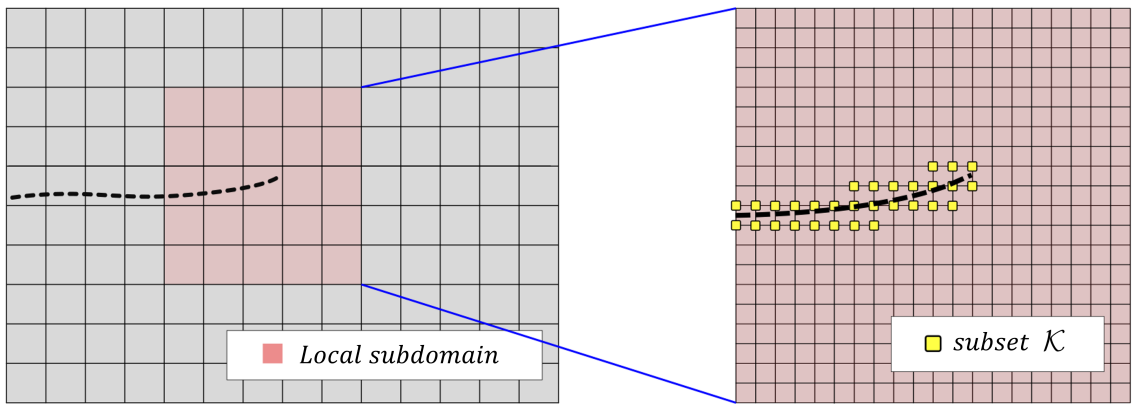


FIGURE 3.3. Global domain  $\Omega$  on the left and local domain  $\Omega_L$  on the right. The nodes in the subset  $\mathcal{K}$ , where  $d$  is set to 1 are colored in yellow.

The crack is represented by prescribing  $d = 1$  in a set  $\mathcal{K} \in \mathcal{T}_L$  of nodes in the local subdomain, as shown in Figure 3.3. This set is constructed in two steps. First, all elements of  $\mathcal{T}_L$  which are intersected by the global fracture triangulation  $\mathcal{F}$  are identified. Then,  $\mathcal{K}$  is defined to be the set of all nodes that belong to any of these intersected elements.

### 3.3.3.2 Transfer of global pressures to local mesh

Due to the different levels of resolution between the global and local problems, we find it advantageous to transfer the pressure fields in a particular manner. We note

that in the global problem, the fracture pressures  $p_f^h$  are available at the cell centers of 1D finite volumes, and the matrix pressures  $p_m^h$  are available at the cell centers of 2D finite volumes. These fields are transferred to quadrature points in the finite element mesh for the local subproblem using the transfer operators  $\Pi_f^{\Omega_L}$  and  $\Pi_m^{\Omega_L}$ .

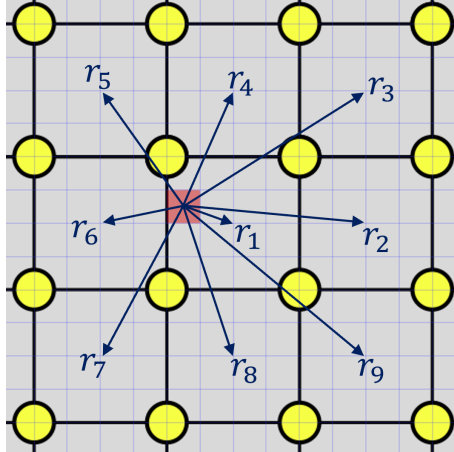


FIGURE 3.4. Illustration of global cells (in gray) in the neighborhood of a local element, indicated in pink. The matrix pressure at a quadrature point in the local element is calculated using an average of global pressures from neighboring cells  $\{i\}$ , with weights corresponding to the distances  $r_i$  between the quadrature point and the cell center.

The operator  $\Pi_f^{\Omega_L}$  that transfers the fracture pressure is straightforward, and inspired by a similar operation described in Santillán et al. [57]. Given any point  $\mathbf{x} \in \Omega_L$ , and a global fracture pressure field  $p_f^h$ ,  $\Pi_f^{\Omega_L} p_f^h(\mathbf{x})$  is obtained by finding the closest cell of  $\mathcal{F}$  to  $x$  and taking the value of  $p_f^h$  at this cell. More precisely,

$$\Pi_f^{\Omega_L} p_f^h(\mathbf{x}) = p_f^h(\arg \min_{c \in \mathcal{F}} \text{dist}(c, \mathbf{x})). \quad (3.27)$$

For the operator  $\Pi_m^{\Omega_L}$  that transfers the matrix pressure field, we use an averaging procedure. This has the effect of smoothing the matrix pressure field at the resolution of the local mesh. At a quadrature point  $\mathbf{x}_Q \in \Omega_L$ , the matrix pressure in the local domain is obtained from a weighted average of the pressures in the global cells that

surround the point. Specifically,

$$\Pi_m^{\Omega_L} p_m^h(\mathbf{x}_Q) = \frac{\sum_{i=1}^s r_i^{-1} p_m^h(c_i)}{\sum_{i=1}^s r_i^{-1}}, \quad (3.28)$$

where  $r_i$  denotes the distance between the quadrature point location and the center of global cell  $i$ , as indicated in Figure 3.4. In the sum, all cells that neighbor the global cell containing quadrature point  $\mathbf{x}_Q$  are used. In the particular case when a quadrature point happens to reside in the center of the local element and  $r_1 = 0$ , the above sum is replaced with  $\Pi_m^{\Omega_L} p_m^h(\mathbf{x}_Q) = p_m^h(c_1)$ .

### 3.3.4 Local problem discretization

With the local subdomain properly identified and initialized, we now describe the additional steps to discretize the displacement and damage fields in the local subdomain and solve for their approximations. The governing equations for the macro-force balance (3.21) and the damage evolution (3.22) are both treated with the finite element method. The damage and displacement fields are both approximated using four-node bilinear quadrilateral elements.

Let  $\Omega_L$  denote the local domain. From the finite-element approximation  $\mathbf{u}_G^h$  computed in the global problem, we extract  $\mathbf{u}_G^h|_{\partial\Omega_L}$  and use it to constrain the displacements on the boundary of the subproblem <sup>2</sup>. As such, the trial space  $\mathcal{U}^h$  is given by

$$\mathcal{U}^h = \{\mathbf{u}_L^h \in H^1(\Omega_L)^n \mid \mathbf{u}_L^h = \mathbf{u}_G^h \text{ on } \partial\Omega_L\}. \quad (3.29)$$

The function space  $\mathcal{D}^h$  of admissible damage fields is given by

---


$$\mathcal{D}^h = \{d^h \in H^1(\Omega_L) \mid d^h = 1 \text{ on } \mathcal{K}\}, \quad (3.30)$$

<sup>2</sup> In the multi-resolution method of Muixi et al. [123], the displacement boundary conditions near the crack base were released. We did not find this to be necessary in our approach.

where  $\mathcal{K}$  denotes the set of damage-fixed nodes that correspond to the global crack at the beginning of the load step, as described in subsection 3.3.3.1.

The test spaces are given by  $\mathbf{W}^h = H_0^1(\Omega_L)^n$  for the displacements and  $\mathcal{C}^h = \{c^h \in H^1(\Omega_L) \mid c^h = 0 \text{ on } \mathcal{K}\}$  for the damage field. The Galerkin approximation to the problem on the local subdomain is then:

### The spatially discrete form

Find  $\mathbf{u}_L^h \in \mathcal{U}^h$  and  $d^h \in \mathcal{D}^h$ , such that  $\forall \mathbf{w}^h \in \mathbf{W}^h$  and  $\forall c^h \in \mathcal{C}^h$ ,

$$(\nabla \mathbf{w}^h, \boldsymbol{\sigma}_L^h) - (\mathbf{w}^h, \Pi_f^{\Omega_L} p_f^h \nabla d^h) - (\mathbf{w}^h, \mathbf{b}) - \langle \mathbf{w}^h, \mathbf{t} \rangle_{\partial_t \Omega} = 0, \quad (3.31)$$

$$\begin{aligned} \frac{2G_c^h \ell}{c_0} (\nabla c^h, \nabla d^h) + \frac{G_c^h}{c_0 \ell} (c^h, \zeta'(d^h)) + (c^h, 2(d^h - 1) W(\boldsymbol{\epsilon}^+(\mathbf{u}_L^h), 0)) \\ - (c^h, \alpha \Pi_m^{\Omega_L} p_m^h \nabla \cdot \mathbf{u}_L^h) + (\nabla c^h, \Pi_f^{\Omega_L} p_f^h \mathbf{u}_L^h) = 0, \end{aligned} \quad (3.32)$$

where we have used  $(\cdot, \cdot)$  to denote the standard inner product in the  $L^2(\Omega)$  space, and  $\langle \cdot, \cdot \rangle$  to denote its restriction on the boundary. In the above,  $\boldsymbol{\sigma}_L^h$  denotes the discrete stress, given by

$$\boldsymbol{\sigma}_L^h = ((1 - d^h)^2 \mathbb{C} : \boldsymbol{\epsilon}(\mathbf{u}_L^h) - (1 - d^h) \alpha p_m^h \mathbb{I}). \quad (3.33)$$

We employ an alternating minimization scheme to solve the coupled system of equations (3.31)-(3.32). Convergence is measured with respect to the  $L_2$ -norms of the change in the damage  $d^h$  and displacement fields  $\mathbf{u}_L^h$ , using a relative tolerance of  $10^{-4}$ . With this approach, each of the equations becomes linear with respect to its primary variable, simplifying the solution process.

We note that (3.32) does not explicitly include the irreversibility constraint (3.25). Within the multi-resolution scheme, the Dirichlet condition  $d^h = 1$  on the crack set  $\mathcal{K}$  is sufficient to prevent the healing of the fracture surface relative to the initial global crack. It does not, however, enforce irreversibility of the damage throughout

the local subdomain, and it is possible that some crack healing could occur if regions are loaded and unloaded during a single time step. We did not find this to occur for the problems studied in this work, but it is possible that this could arise in more complex cases and the use of a more robust means of enforcing the constraint on the damage would be needed. Options include, for example, the active set solver described in [61].

In terms of the local dissipation function  $\zeta(d)$ , in this work we use  $\zeta(d) = d$  which corresponds to the AT-1 phase-field model of fracture. This is selected due to the fact that it gives rise to a compactly supported damage field and a fully elastic stage prior to damage initiation [? ]. When using the AT-1 model, it is necessary to explicitly enforce the constraint  $d^h \geq 0$ , as in some cases, this formulation can lead to negative damage values. In this work, this is effected by invoking a lower threshold on the active part of the strain energy  $W(\boldsymbol{\epsilon}^+(\mathbf{u}_L^h), 0) = 3G_c/8\ell$ , as in [51].

Finally, we note that phase-field models of fracture tend to give rise to a mesh and regularization length dependent critical fracture energy that is larger than  $G_c$  [11]. To account for this, we use a discrete value of  $G_c^h$  that is obtained as a function of the local mesh spacing and regularization length, as

$$G_c^h = G_c \left( 1 + \frac{h_{local}}{c_0 \ell} \right)^{-1}, \quad (3.34)$$

such that the effective critical fracture energy is very close to that of the material.

### 3.3.5 Crack propagation: translating local damage updates into global crack extensions

A key step of the algorithm concerns how changes to the damage in the local subdomain are translated into updates to the crack geometry in the global domain. We provide details of our algorithm for this procedure here. The scheme is presented in the context of a single crack tip that is propagating through the global domain.

Although we do not consider much more complex cases in this work, such as changes in crack topology (due to crack branching or merging), we note that such problems have been examined in other works employing hybrid phase-field approaches. This includes the recent work of Muixi et al. [123], albeit in a purely mechanical context.

At each step in the solution algorithm, in the global problem, we keep track of two geometric entities, namely the global crack tip and the global tip element (Figure 3.5a). The global crack tip is defined by the interior endpoint of the crack. The global tip element is the element that contains the tip on one of its sides, but is not yet “cut” by the crack. In essence, it is the global element just ahead of the propagating crack tip. In the local subproblem, we identify a local version of the crack tip that is obtained from the discrete damage field  $d^h$  (Figure 3.5b and 3.5c). The algorithm to extend the global crack geometry depends on the relative location of the global crack tip, global tip element, and local crack tip, as described below.

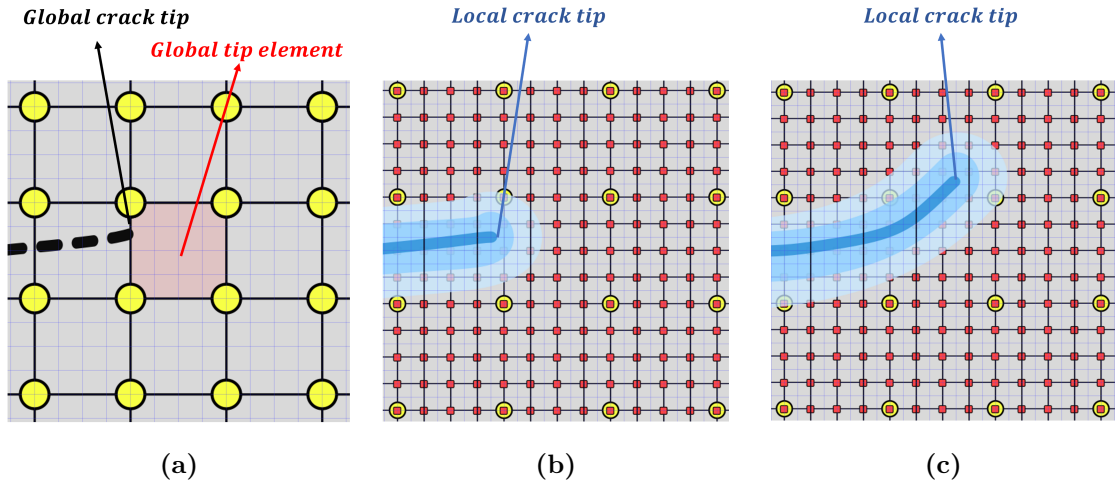


FIGURE 3.5. (a): Illustration of the global crack tip and global tip element. (b) Case when the local tip falls inside the tip element. (c) Case when the local tip falls outside the tip element.

The enrichment strategy described in Section 3.3.2 requires global elements that are completely cut by the crack geometry. As such, any extension of the crack geom-

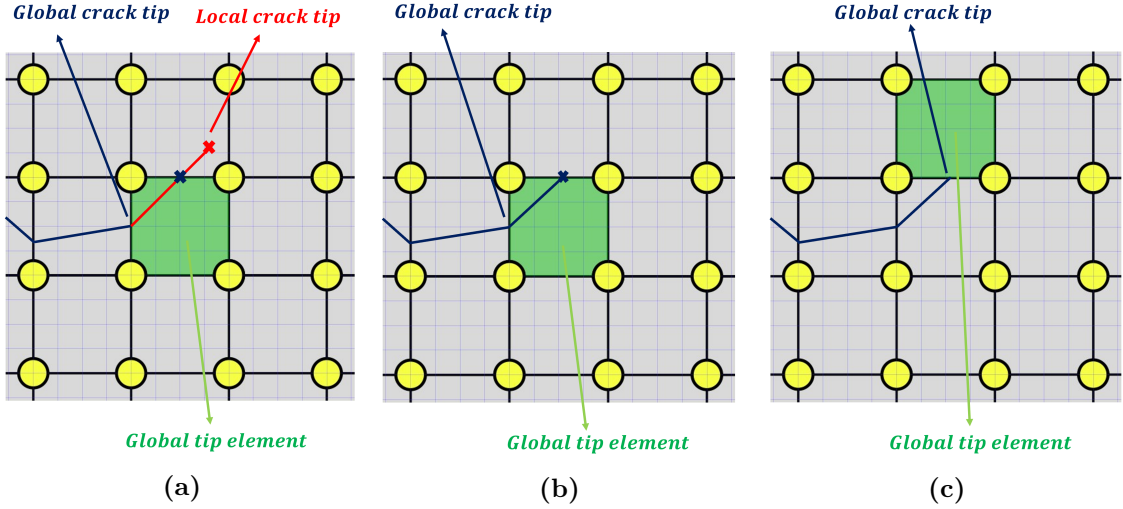


FIGURE 3.6. (a): Construction of the segment connecting global and local tips. (b) New crack segment to be added. (c) Update of the global crack tip and global tip element.

etry at the global scale must correspond to the global tip element being fractured. Accordingly, global crack propagation is triggered whenever the local tip falls outside the tip element. In this case, the new global tip is identified by connecting the current global tip and the local tip. Since the local tip is outside the tip element, a new segment will intersect the perimeter of the tip element exactly once (neglecting the obvious intersection at the current global tip). This process is illustrated in Figure 3.6. Any crack advance beyond this new tip location is neglected at this point, and the algorithm returns to a new global solve with an updated crack geometry.

In general, the problem of extracting a sharp crack front from a diffuse representation is not trivial. When the crack evolution involves complex topological changes, it is particularly difficult[? ]. In the numerical examples studied in this manuscript, we take advantage of the relatively simple fracture geometry and predicted crack patterns to simplify this process. In particular, we first identify all elements in the local subdomain with nodes whose damage values are all above a threshold  $d_{tr}$ . A similar approach was proposed in [122]. The local crack tip is taken to be the center

of the element in this set that is farthest from the base of the crack in the local subdomain. The threshold used for this process is taken to be  $d_{tr} = 1 - h_{local}/(2\ell)$ , which is based on the estimate for a damage field near a crack tip given in [80]. In essence, for a phase-field model of fracture, this threshold identifies nodes that are expected to correspond to the peaks of the discrete damage field. For a damage band resolved with a mesh spacing of  $\ell/h_{local} = 4$ , this gives rise to a threshold of  $d_{tr} = 0.875$ .

### 3.3.6 Algorithm summary

Having described the solution strategies for both the global and local problems and the transfer of various quantities, we now detail the algorithm (1) that couples the two problems together to simulate crack propagation. Figure 3.7 provides an illustration of the algorithm. Within each time step (outer loop), the algorithm employs an inner loop that allows the global problem to be updated as soon as any large enough change in the crack geometry is detected in the local subproblem. The inner loop is terminated when the propagation step, described in subsection 3.3.5 does not identify any crack advance. The construction with two nested loops can be viewed as an implicit treatment of the fracture front position, which, according to Lecampion et al. [115] tends to be more accurate and robust, permitting the use of larger time steps.

---

**Algorithm 1:** Solution algorithm for multi-resolution hydraulic fracture

---

Define initial and boundary conditions

$n = 1$

$n_F = endStep$

**while**  $n \leq n_F$  **do**

$\mathcal{F}_n^1 = \mathcal{F}_{n-1}$

**for**  $1 \leq k \leq maxIter^a$  **do**

(1) Solve **Global Problem** and obtain  $\mathbf{u}_G^{k,n}, p_m^{k,n}, p_f^{k,n}$

(2) Construct subdomain  $\Omega_L$  and submesh  $\mathcal{T}_L$ . Identify subset of cracked nodes  $\mathcal{K}$ .

(3) Prescribe local boundary conditions  $\mathbf{u}_L^h|_{\partial\Omega_L} = \mathbf{u}_G^{k,n}|_{\partial\Omega_L}$  and  $d^h = 1$  on  $\mathcal{K}$ .

(4) Construct local pressure fields  $p_m = \Pi_m^{\Omega_L}(p_m^{k,n})$  and  $p_f = \Pi_f^{\Omega_L}(p_f^{k,n})$

(5) Solve the **Local Problem** to obtain  $d^k$ .

(6) Use  $d^k$  and the propagation step (subsection 3.3.5) to update discrete fracture  $\mathcal{F}_n^k$ .

**if**  $\mathcal{F}_n^{k+1} = \mathcal{F}_n^k$  **then**

$n = n + 1$

$\mathcal{F}_n = \mathcal{F}_n^k$

$\mathbf{u}_G^n = \mathbf{u}_G^{k,n}$

$p_m^n = p_m^{k,n}$

$p_f^n = p_f^{k,n}$

break

**end**

**end**

**end**

---

<sup>a</sup> The index  $k$  is only a dummy variable for this loop that searches for the correct fracture geometry at a given time step.

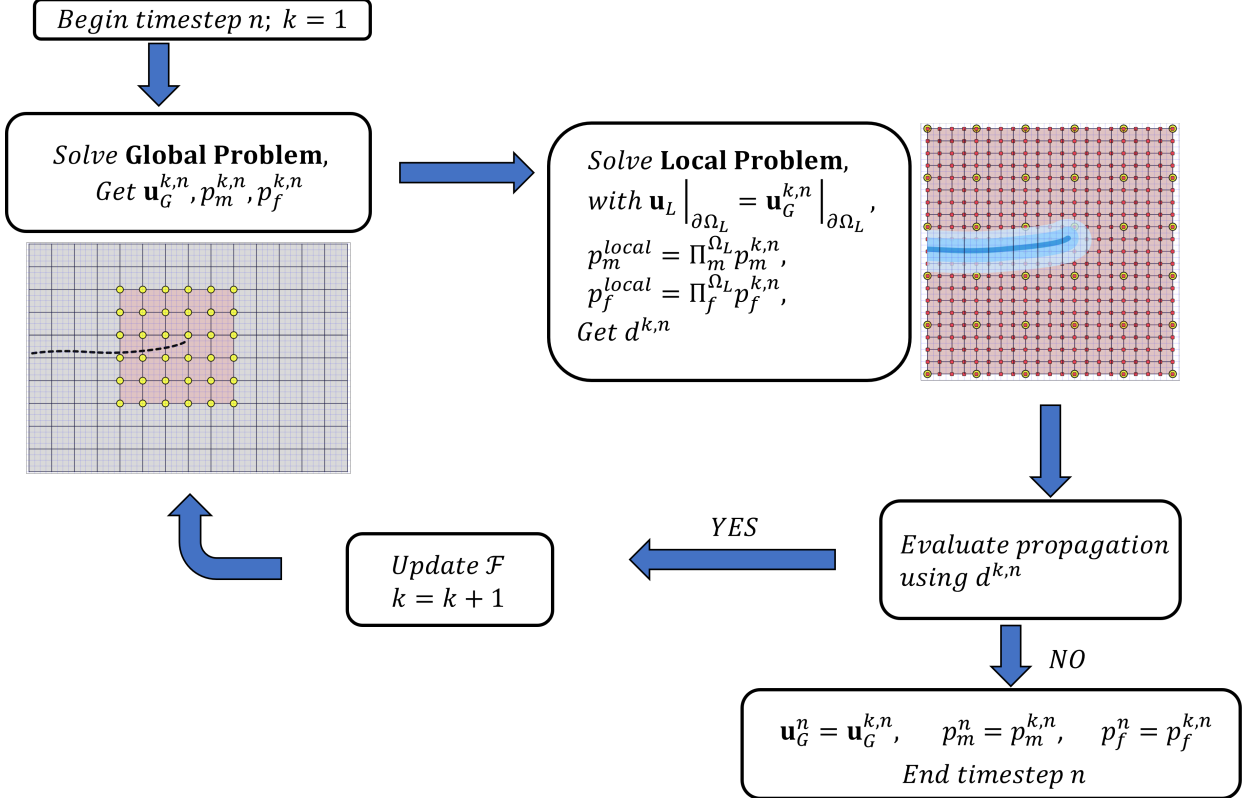


FIGURE 3.7. Multi-resolution solution algorithm.

### 3.4 Numerical Results

We now present the results from various benchmark problems in fluid-driven fracture propagation. The problems range from those in which flow is only present within the cracks to fully coupled problems involving flow in both the matrix and the evolving manifold that is the fracture geometry. With the sole exception of the toughness-dominated KGD problem, all of the results in this section employ the spectral split of the energy, as described in Section 3.2.2.

#### 3.4.1 KGD problems

We begin with the well-known Khristianovic, Geertsma and De Klerk (KGD) problems of hydraulic fracture [127, 128]. The problems concern the propagation of a planar fracture in an infinite, impermeable domain, under the injection of a viscous

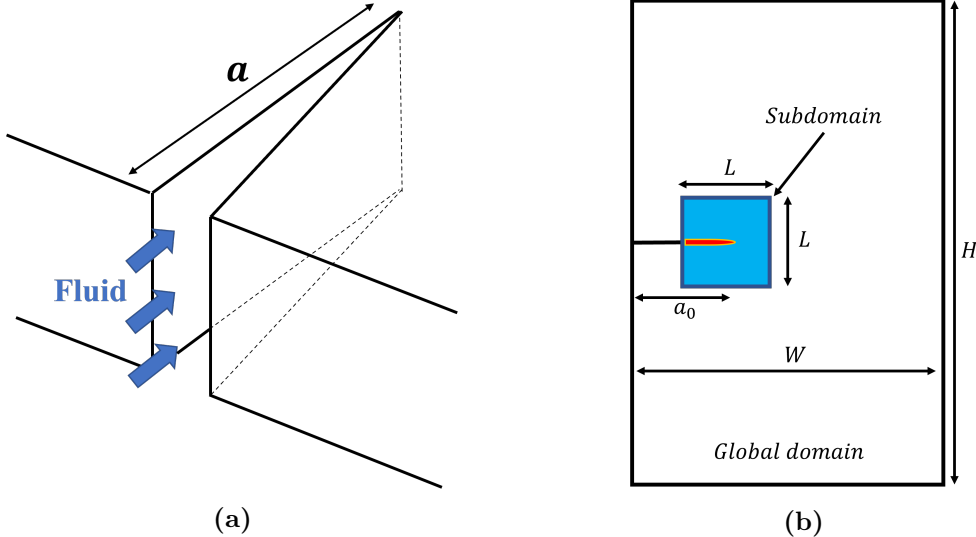


FIGURE 3.8. (a) Schematic of the KGD problem, inspired by [2]. (b) Computational domain for the KGD problem (not to scale).

fluid at a constant rate (Figure 3.8).

The response of the system can be characterized by the dimensionless group  $\mathcal{K}$  [93]:

$$\mathcal{K} = \frac{4G_c^{1/2}}{(6\pi^2 E' Q \mu)^{1/4}}, \quad (3.35)$$

where  $E' = E/(1 - \nu^2)$ . Values of  $\mathcal{K} > 4$  correspond to the “toughness dominated regime” in which crack growth is largely controlled by the fracture toughness of the media. By contrast, when  $\mathcal{K} < 1$ , the fracture toughness is relatively small and the fluid viscosity is the main factor controlling the speed of crack growth. In the following, we explore the performance of the multi-resolution algorithm to simulate problems in both regimes.

#### 3.4.1.1 Toughness-dominated regime

The toughness dominated regime is characterized by the creation of new fracture surfaces accounting for almost all of the energy dissipation. In this scenario, the fluid

can be considered to be inviscid, which leads to a constant pressure distribution over the entire crack. The assumption of inviscid flow reduces much of the complexity, allowing for the construction of a simple analytical solution for this problem. Here, we consider a problem in the toughness-dominated regime resulting from the material parameters and settings given in Table 3.1. Using these values in (3.35), we obtain  $\mathcal{K} = 6.54$ .

**Table 3.1.** Material properties and problem parameters for the toughness-dominated KGD problem

	Value	Unit
Young's modulus ( $E$ )	16.0	GPa
Poisson's ratio ( $\nu$ )	0.18	—
Fluid viscosity ( $\mu$ )	$1.0 \times 10^{-12}$	GPa . s
Energy release rate ( $G_c$ )	$1.85 \times 10^3$	N/m
Injection rate ( $Q$ )	$1.0 \times 10^{-3}$	m <sup>2</sup> /s
Initial crack size ( $a_0$ )	4	m

The analytical solution for this problem can be separated into two stages as a function of time. In the first stage, the pressure builds linearly with time and the crack does not propagate, as the pressure is below the critical threshold  $p_{cr} = (G_c E' / \pi a_0)^{1/2}$ . The pressure then reaches the critical value at  $t = t_{cr}$ , after which the crack begins to propagate. In the second stage the propagation is stable, since the amount of fluid injected is finite and crack propagation leads to a pressure drop as the total space available for the fluid to occupy increases.

The solution for the crack length and pressure in the crack can be written as

$$a(t) = \begin{cases} a_0, & t \leq t_{cr}, \\ \left( \frac{E'(Qt)^2}{\pi G_c} \right)^{1/3}, & t \geq t_{cr}, \end{cases} \quad (3.36)$$

$$p(t) = \begin{cases} \frac{t}{t_{cr}} p_{cr}, & t \leq t_{cr}, \\ \left( \frac{E' G_c^2}{\pi Q t} \right)^{1/3}, & t \geq t_{cr}, \end{cases} \quad (3.37)$$

where  $t_{cr} = (\pi G_c a_0^3 / Q^2 E')^{1/2}$ . A derivation of this solution can be found in Yoshioka [80].

For simulations using the multi-resolution scheme, a computational domain of size  $W \times H = 30 \text{ m} \times 240 \text{ m}$  is used (Figure 3.8b). According to [?], this domain size should be sufficiently large to yield a good approximation to an infinite plane. We first report results using a sub-domain size of  $L \times L = a_0 \times a_0$ . The sensitivity of the results to the choice of sub-domain size will be discussed later in this subsection.

In what follows, we report results from a refinement study. In particular, we report results for three different regularization lengths of decreasing value, beginning with  $\ell = a_0/15$ . As the regularization length is decreased, we maintain a mesh size in the subdomain of  $h_{local} = \ell/4$ . This allows the finite-element approximation to sufficiently resolve the regularized fracture band. We also note that the effective fracture toughness in the computational problem depends on  $h/\ell$  [80]. In the global domain, we maintain the mesh spacing at the ratio of  $h_{global} = 3h_{local}$ . For the coarsest global mesh, this translates into roughly 20 elements over the span of the initial crack geometry. This level of resolution is consistent with those found to be sufficient for resolving pressurized cracks using the Embedded Finite Element Method, in Cusini et al. [126].

The results obtained with the multi-resolution scheme are compared to the analytical solutions 3.36 and 3.37 in Figures 3.9a and 3.9b. We note the overall good match between the simulation results and the analytical solution, as well as the convergence of the results towards 3.36 and 3.37 when  $\ell$  decreases. Although this problem is relatively simple as the matrix is assumed to be impermeable, it does test

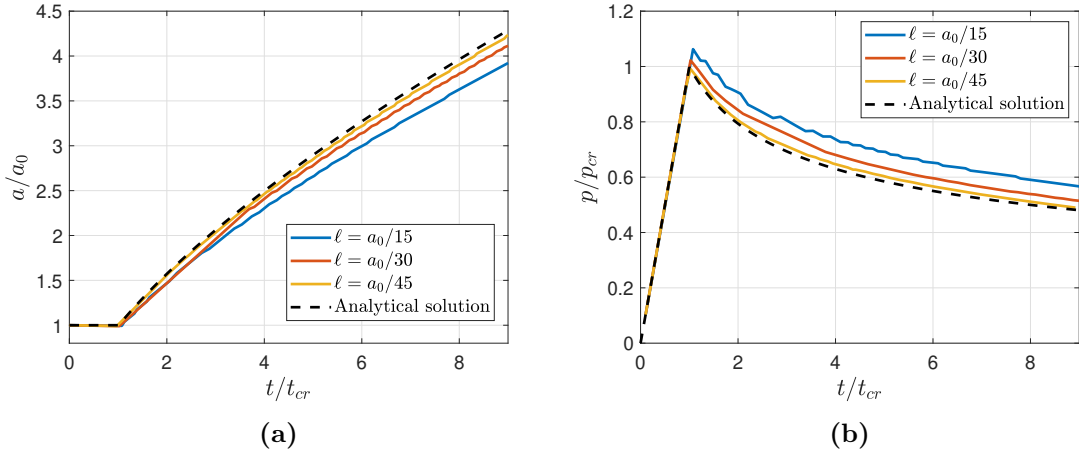


FIGURE 3.9. Comparison of numerical results and analytical solution for the toughness-dominated KGD problem: (a) crack length vs. time and (b) pressure vs. time.

the coupling between the global and the local domains and verifies that the phase-field method, even when used only in a vicinity of the crack tip, can still provide accurate predictions of fracture propagation. Although the spectral split was not employed for this problem, we did examine the results using it. Qualitatively they were found to be very similar, with slightly less accuracy in the calculated values of the critical pressure.

We now examine the sensitivity of the results to changes in the subdomain size. This is accomplished by fixing the sizes of the global and local meshes as well as the regularization length, and varying only  $L$  in Figure 3.8b. In particular, we fix the regularization length to  $\ell = 0.13$  m and vary the sub-domain size between  $15\ell$  and  $45\ell$ .

Figures 3.10a and 3.10b provide the results for the pressure and crack length as a function of time, for the various choices of subdomain size. Table 3.2 shows the error in the computation of the crack length relative to the analytical solution. The error is taken as an average over the time range, starting at the beginning of propagation.

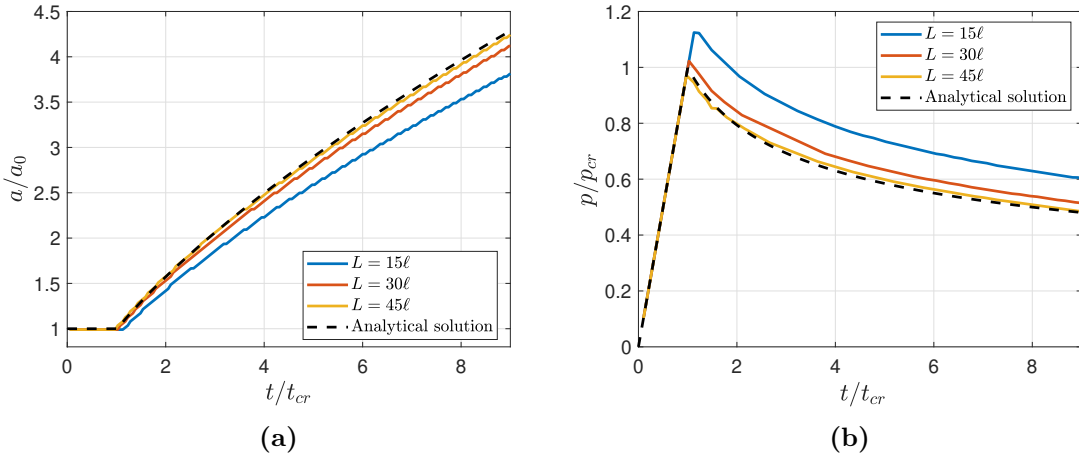


FIGURE 3.10. Study of the effects of subdomain size on the results of the toughness-dominated KGD problem: (a) influence on predicted crack length and (b) predicted pressure.

**Table 3.2.** Effect of subdomain size on the relative error in the crack length.

Subdomain size	Relative error
$L = 15\ell$	11.5%
$L = 30\ell$	3.3%
$L = 45\ell$	1.1%

The results indicate that the error reduces as the subdomain size is increased. In this particular study, both the global and subdomain meshes are fairly refined, and so the improvement in accuracy as  $L$  increases is not likely due simply to better resolution in the local subdomain. Rather, it may be due to the fact that the two problems are coupled through the global displacements applied to the subdomain boundary. As the subdomain size is increased, the boundary of the subdomain moves farther from the crack tip singularity, and one would expect a better correspondence between the displacement fields obtained from the global problem and those obtained using a phase-field approximation over the entire domain. Furthermore, as the global displacements are held fixed until the regularized crack advances sufficiently far, there is some sensitivity of the proximity of the regularized crack tip to the subdomain

boundary.

In more general cases, one would expect the subdomain mesh to be at quite a bit higher resolution than the global mesh. Since the phase-field problem also requires several iterations in the alternate minimization scheme, problems are expected to become much more computationally expensive as  $L$  is increased. As a result, a trade-off between accuracy and computational cost is to be expected. In general, one should select a subdomain size that strikes a balance between being large enough to capture the crack evolution and small enough to render the overall calculation efficient.

#### *3.4.1.2 Viscosity dominated KGD problem*

We now consider a case in which the choice of parameters gives rise to conditions wherein the energy dissipation is dominated by viscous dissipation. In particular, we consider the material properties and problem parameters provided in Table 3.3. Consistent with (3.35), these values give rise to  $\mathcal{K} = 0.57$ , a result that is clearly within the viscosity-dominated regime.

**Table 3.3.** Material properties and problem parameters for the viscosity-dominated KGD problem

	Value	Unit
Young's modulus ( $E$ )	0.17	GPa
Poisson's ratio ( $\nu$ )	0.20	—
Fluid viscosity ( $\mu$ )	$1.0 \times 10^{-10}$	GPa . s
Energy release rate ( $G_c$ )	21	N/m
Injection rate ( $Q$ )	$1.0 \times 10^{-3}$	m <sup>2</sup> /s
Initial crack size ( $a_0$ )	4.0	m

In this scenario, the toughness of the medium can be neglected, and the fracture evolution is effectively dictated by the motion of the fluid front. In this case, the pressure varies with time and space over the length of the fracture surface. Although this problem does not include a pressure field in the matrix, it bears emphasis that it does require the transfer of the pressure field in the fracture from the global scale

to the phase-field problem in the subdomain. As such, it serves as a test of that aspect of the multi-resolution scheme. The presence of dynamic terms in the fluid equation also implies the need for a discretization with sufficiently accurate temporal resolution, and in what follows we examine the sensitivity of the results to the choice of the time step size.

Once again, consider a computational domain with dimensions  $W \times H = 30 \text{ m} \times 240 \text{ m}$ . The sub-domain size is taken as  $L \times L = a_0 \times a_0$ , and the regularization length is taken to be  $\ell = a_0/15$ . In contrast to what we observed for the toughness regime, we note that the results to the viscosity-dominated problem were found to be largely insensitive to the choice of the regularization length, provided that  $\ell < a_0/10$ . This is not surprising, given that the phase-field subproblem only serves to propagate a crack that has effectively zero toughness.

In what follows, we report results using mesh spacings in the local and global domains of  $h_{local} = \ell/4$  and  $h_{global} = 3h_{local}$ . As an initial condition, the pressure field is prescribed to match the analytical solution. We report on the temporal convergence of results obtained using fixed time steps, beginning with  $dt_0 = 0.5\text{s}$ . As (discrete) negative pressures arose in our simulations, the phase-field model was modified to account for a tension-compression asymmetry. In particular, consistent with the model described in Miehe et al. [92], the strain energy density was split into active and inactive parts, and only the “tensile” part was degraded with the damage.

Figure 3.11 compares the analytical solutions for the crack length and inlet pressure to the model-based simulation results for a sequence of decreasing time steps. The initial time ( $t_0 = 8.5 \text{ s}$ ), initial inlet pressure ( $p_0 = 40 \text{ kPa}$ ) and initial crack size ( $a_0 = 4 \text{ m}$ ) were used to render the results dimensionless. The particular values of  $t_0$  and  $p_0$  were chosen in order to make our initial state a snapshot of the analytical solution. Overall, the good agreement between the results indicates that the

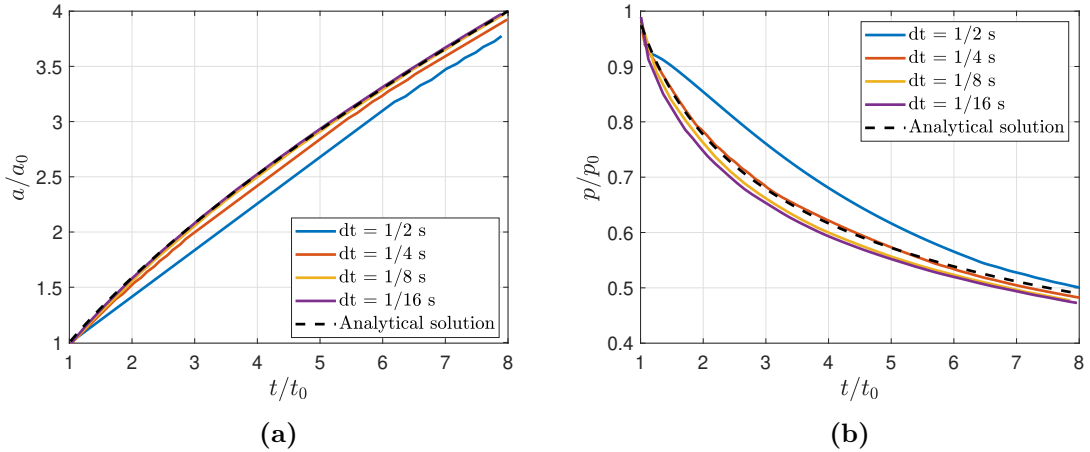


FIGURE 3.11. Numerical results and analytical solution for the viscosity-dominated KGD problem: (a) crack length vs. time; and (b) inlet pressure vs. time.

multi-resolution scheme is capable of handling a viscosity-dominated case.

The results for the crack length show an excellent agreement with the analytical solution as the time step is decreased. The results for the inlet pressure (Figure 3.11b) appear to converge to a trajectory that is slightly offset from the analytical solution as the time step is decreased. This relatively small discrepancy can be explained by the presence of a minimum aperture that is assigned to the newly-initialized finite volumes in the flow solver. As explained in [116], this is necessary to preserve the stability of the scheme when new crack segments are added. The recent work by Jin et al. [?] proposes a method for removing this parameter by employing partially fractured elements. The incorporation of similar modifications in the context of the multi-resolution scheme is the subject of future work.

### 3.4.2 Poroelastic problem with coupled matrix-fracture flow

We now examine a problem in which the matrix is permeable and there is a coupling between the fluid flow in the fracture, fluid flow in the matrix, and crack propagation. A schematic of the problem is shown in Figure 3.12. It corresponds to a rectangular

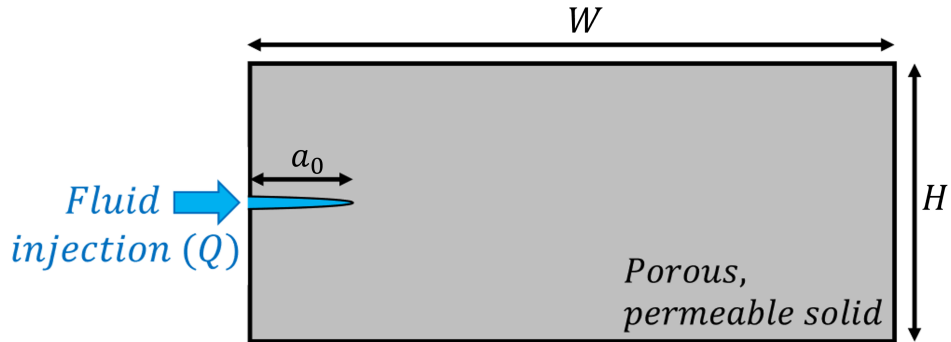


FIGURE 3.12. Geometry and notation for the coupled poroelastic-fracture problem.

domain subject to the injection of a viscous fluid at the mouth of an initial fracture. The fluid injection rate  $Q$  is assumed to be constant, and the displacement in the normal direction is fixed on all sides of the domain.

Although this problem is relatively simple, to our knowledge an analytical solution is not available. In what follows, we therefore compare our results to those that are obtained using an existing phase-field method for hydraulic fracture. In particular, we compare our results to those obtained using the method described by Miehe and Mauthe [119, 51]. This is arguably one of the simpler methods available for this class of problems, combining the equations for phase-field fracture, Biot's theory of linear poroelasticity in the matrix, and lubrication theory for fluid flow within fractures.

The model assumes that a Darcy model of flow holds in the matrix, with isotropic permeability. In the fractures, a lubrication flow model is assumed. The transition between the two flow regimes is effected through the use of a permeability tensor that varies as a function of the crack aperture and orientation. In particular, the permeability tensor  $\kappa$  is given by

$$\kappa = \kappa_0 + d^\xi \frac{w_n^2}{12} (\mathbf{I} - \mathbf{n}^d \otimes \mathbf{n}^d), \quad (3.38)$$

$$w_n = h(\mathbf{n}^d \cdot \boldsymbol{\epsilon} \cdot \mathbf{n}^d), \quad (3.39)$$

in which the normalized gradient  $\mathbf{n}^d = \nabla d / |\nabla d|$  approximates the normal to the crack plane. In the above,  $\kappa_0$  is an isotropic part of the permeability that accounts for the undamaged permeability of the matrix,  $w_n$  is the crack's normal aperture, and  $\xi$  is a weighting exponent. The weighting exponent concentrates the effects of the second term in 3.38 to areas where  $d \approx 1$ . Consistent with the work of Miehe and Mauthe [119, 51], we use  $\xi = 50$ .

**Table 3.4.** Material properties for poroelastic problem

	Value	Unit
Young's modulus ( $E$ )	16.0	GPa
Poisson's ratio ( $\nu$ )	0.18	—
Fluid viscosity ( $\mu$ )	$1.0 \times 10^{-12}$	GPa . s
Energy release rate ( $G_c$ )	3.67	N/m
Biot coefficient ( $\alpha$ )	0.79	—
Rock permeability ( $\kappa_0$ )	$1.0 \times 10^{-13}$	m <sup>2</sup>

**Table 3.5.** Problem settings

	Value	Unit
Phase-Field reg. length ( $\ell$ )	0.2	m
Subdomain size ( $L$ )	4.0	m
Domain width ( $W$ )	30	m
Domain height ( $H$ )	10	m
Initial crack size ( $a_0$ )	4.0	m
Injection rate ( $Q$ )	$1.0 \times 10^{-3}$	m <sup>2</sup> /s

The material properties used in this problem are given in Table 3.4, while the problem and model parameters are provided in Table 3.5. The results reported in this section rely on the use of an eigen-decomposition of the strain energy, as described in Miehe et al. [92]. The subdomain size for the multi-resolution method was chosen to be proportional to the initial crack size, or  $a_0 \times a_0$ . The problem

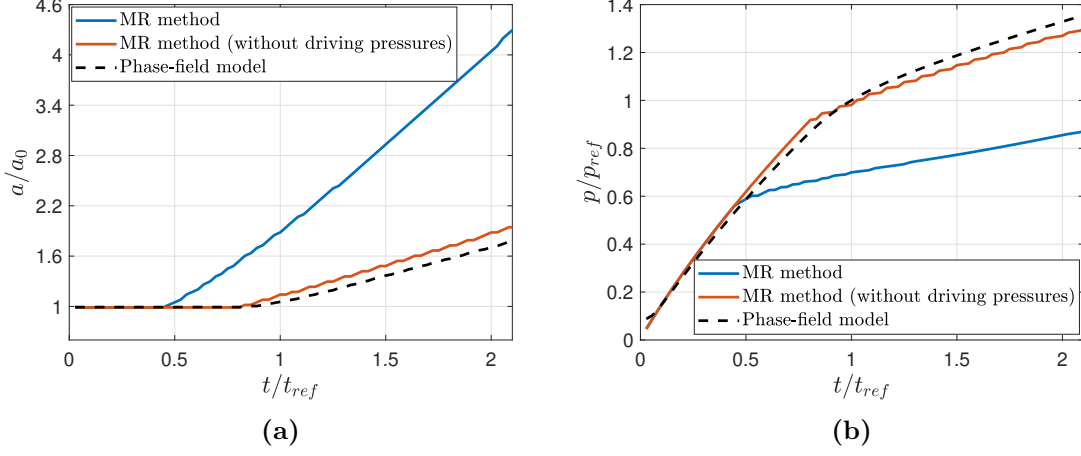


FIGURE 3.13. Results from the fully coupled poroelastic-fracture problem for the multi-resolution method (with and without driving pressures) and a standard phase-field model: (a) crack size over time, (b) inlet pressure. The time for crack propagation ( $t_{ref}$ ) in the phase-field model and the corresponding inlet pressure ( $p_{ref}$ ) are used as references for the dimensionless charts above.

was discretized spatially using a uniform mesh in the local domain with  $h_{local} = \ell/4$ , while  $h_{global} = 3h_{local}$  was used in the global domain. For the temporal discretization, a uniform time step of  $dt = 0.125$  s was used. This level of spatial and temporal discretization was found to yield results that were sufficiently converged.

An important difference between the phase-field formulation used in Miehe and Mauthe [119, 51] and that employed in the current multi-resolution method concerns the use of pressure-dependent driving forces. We draw the reader's attention to the terms involving the pressure fields  $p_m$  and  $p_f$  in the evolution equation (3.22) for the damage field. In our studies of the KGD problem, we found these terms necessary to include in order to obtain sufficiently accurate simulations. We refer to these terms as “driving pressures” as the pressure fields contribute directly to the evolution of the damage field. Importantly, the phase-field formulation of Miehe and Mauthe [119, 51] does not include these terms in the damage evolution equation. Accordingly, in what follows we find it useful to compare results from Miehe and Mauthe [119, 51] to those obtained using our multi-resolution method with and without the driving pressures.

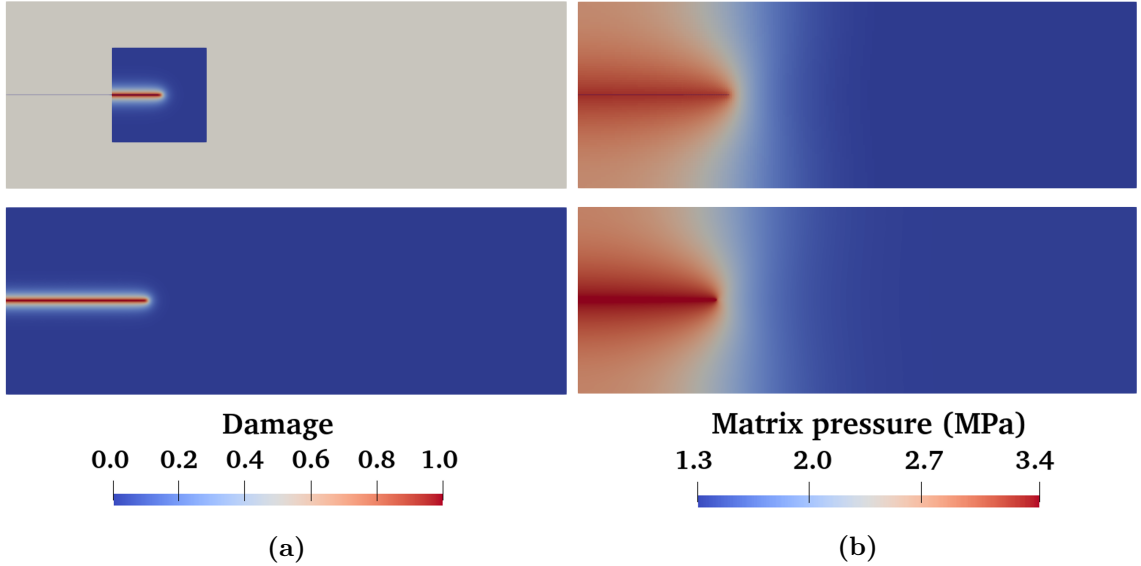


FIGURE 3.14. Fields from the coupled poroelastic-fracture problem, taken at the end of the simulation, contrasting results from the multi-resolution scheme without the driving pressures (top row) to those obtained using a standard phase-field model of fracture in poroelastic media (bottom row). (a) Contour plots of the damage field. (b) Contour plots of the pressure field.

Results for the crack length and inlet pressure as a function of time are provided in Figure 3.13. Contour plots of the damage and pressure fields for the multi-resolution scheme and the full phase-field formulation are provided in Figure 3.14. Despite the numerous differences in the models, the results obtained with the multi-resolution compare very favorably to those obtained using our implementation of the phase-field fracture model [51]. This is particularly the case when the driving pressures are removed from the multi-resolution method, such that the two phase-field models are as close as possible. At early times the crack remains stationary, as the pressure at the inlet increases. At some point the pressure near the crack tip reaches a magnitude that is sufficient to give rise to crack propagation. After crack propagation begins, the rate of pressure increase begins to decrease with time, as crack growth allows for additional fluid to be accommodated within the fracture. Clearly the phase-field subproblem with a frozen pressure field that acts effectively as a body force is still

capable of simulating crack propagation, even when there is flow in the crack and the matrix. It bears emphasis that the multi-resolution scheme does not need to rely on estimations such as 3.38,3.39 to extract an approximation to the aperture from the regularized crack geometry.

### 3.4.3 Propagation around an inclusion

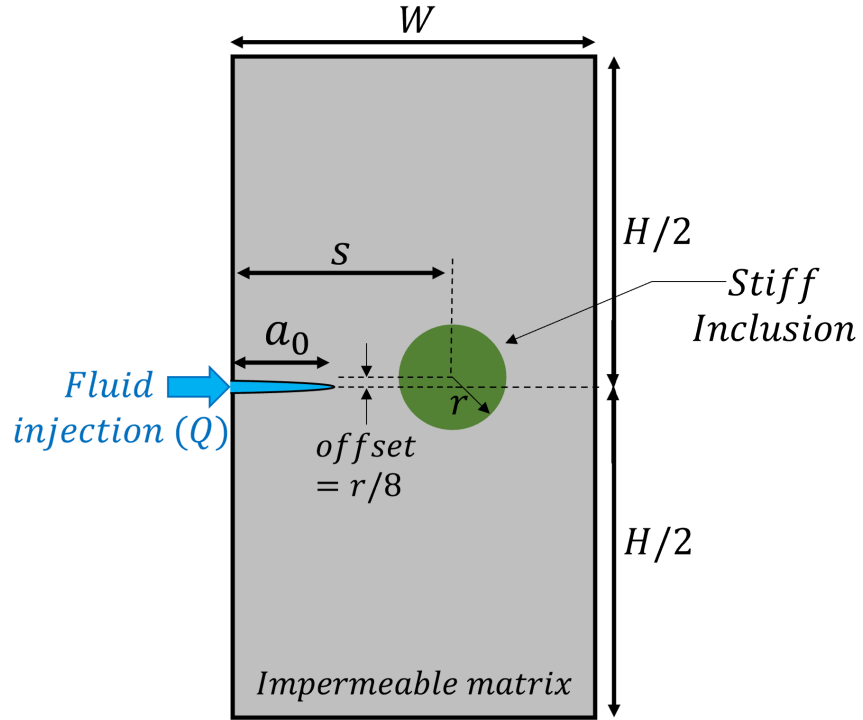


FIGURE 3.15. Geometry for the inclusion problem.

We now consider a problem that gives rise to a non-planar crack evolution. Specifically, we investigate the effects of a stiff inclusion on the trajectory of a hydraulically-driven fracture in an impermeable medium. The problem setup is shown in Figure 3.15. A circular inclusion of radius  $r$  is placed in a rectangular domain, at a distance  $s$  from the left boundary, and slightly offset from the axis of symmetry. The inclusion is assumed to have properties that are identical to the matrix, with the exception of the Young's modulus. An initial crack of size  $a_0$  is placed in the left boundary and

a fluid is injected at a constant rate  $Q$ . The complete set of material properties and geometric parameters are listed in Tables 3.6 and 3.7.

**Table 3.6.** Material properties for inclusion problem

	Value	Unit
Young's modulus ( $E$ )	9.0	GPa
Poisson's ratio ( $\nu$ )	0.25	—
Fluid viscosity ( $\mu$ )	$1.0 \times 10^{-12}$	GPa . s
Energy release rate ( $G_c$ )	$2.5 \times 10^6$	N/m

**Table 3.7.** Problem settings

	Value	Unit
Phase-Field reg. length ( $\ell$ )	0.4	m
Subdomain size ( $L$ )	4.0	m
Domain width ( $W$ )	20	m
Domain height ( $H$ )	40	m
Initial crack size ( $a_0$ )	4.0	m
Injection rate ( $Q$ )	$1.2 \times 10^{-1}$	$m^2/s$

Simulations using the multi-resolution scheme were conducted for three different values of inclusion stiffness, with  $h_{local} = \ell/6$  in the local domain, and  $h_{global} = 3h_{local}$  in the global domain. The objective was to test how the stiffness of the inclusion influenced the crack trajectory. Consider the following two limiting cases. When the inclusion is just slightly stiffer than the matrix, one would expect the crack trajectory to remain straight. At the other extreme, when the inclusion is much stiffer, one would expect the crack to propagate around it.

The crack paths predicted by the multi-resolution scheme are shown in Figure 3.16. The deformed meshes are shown with displacements exaggerated to highlight the crack trajectories. As expected, for an inclusion with much higher stiffness, the crack propagates around it. By contrast, when the stiffness of the inclusion is relatively close to that of the matrix (2X case), the trajectory remains nearly straight. Interestingly, for an intermediate value, where the inclusion is 7 times stiffer than

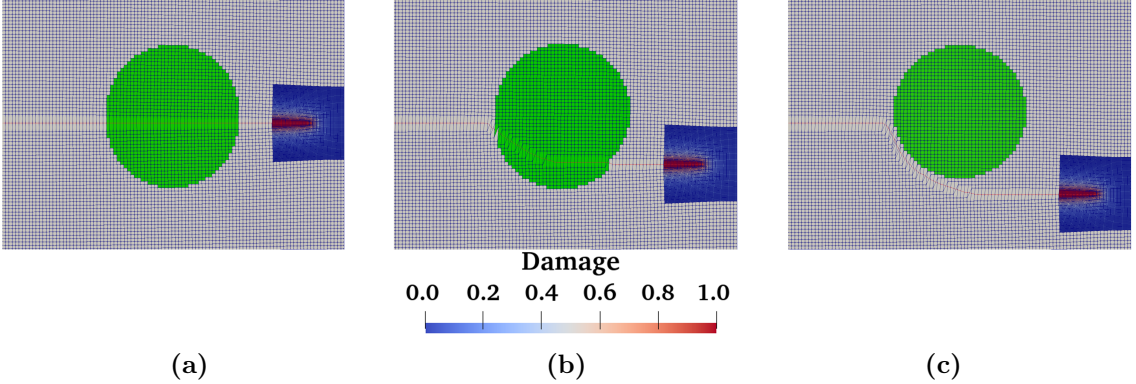


FIGURE 3.16. Crack paths for the inclusion problem: (a) 2X stiffer inclusion; (b) 7X stiffer inclusion; and (c) 15X stiffer inclusion.

the matrix, the crack trajectory gets deflected, but still goes through the inclusion.

The pressures at the injection point are plotted as a function of time in Figure 3.17. Due to the very high toughness of the material, they are almost uniform over the crack. For this problem, we did not observe much sensitivity of the results to the choice of time step size. By analyzing these curves, we can identify several different stages for this problem. At early times before any crack propagation begins, we observe a linear increase in pressure with time. Then, as we reach a certain pressure, which we denote as  $p_{ref} = 60$  MPa, straight crack propagation starts and proceeds until the tip approaches the inclusion. Due to the higher stiffness of the inclusion, the crack arrests and pressure builds up again until it reaches a level that is sufficient to allow propagation to continue. This is accompanied by a pressure drop that is most pronounced for the higher-stiffness inclusion cases.

This problem highlights several capabilities of the multi-resolution scheme, such as the simple handling of crack curving as well as changes in the crack speed, including crack arrest. Although we are not aware of any analytical solution for problems like this, the results we have obtained appear to make sense qualitatively.

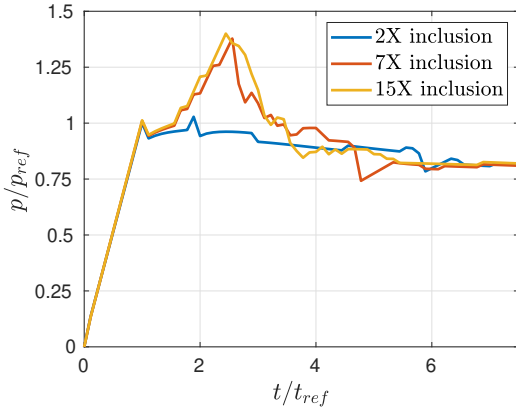


FIGURE 3.17. Inlet pressure as a function of time for the three inclusion problems, corresponding to inclusions with different stiffnesses. The reference values of the pressure  $p_{ref}$  and time  $t_{ref}$  were defined as the minimum pressure that led to fracture growth and the associated time, considering the simulated injection rate.

### 3.5 Summary and conclusions

This manuscript presents a new approach for developing model-based simulations of hydraulic fracturing. The method relies on a global problem that captures flow and deformation fields, and a local problem that captures crack growth with the aid of a phase-field method. The two problems are coupled through the transfer of displacement and pressure fields, as well as updates to the crack geometry. This multi-resolution approach allows the phase-field method to be used as a tool to update the crack geometry without the need to explicitly reconstruct the crack aperture from the diffuse representation.

The accuracy of the multi-resolution approach is evaluated through several numerical examples. These include the well-known KGD problem, for which a good agreement with analytical solutions is obtained in both the toughness and viscosity regimes. A problem with a curved crack trajectory around a stiff inclusion also demonstrates the overall robustness of the approach. Several areas for future work present themselves. These include, for example, an enhancement of the algorithm to identify the sharp crack tip from the diffuse damage field; treatment of problems

involving crack branching and merging; three-dimensional geometries and crack nucleation in arbitrary locations.

# 4

## Extending the Multi-Resolution Approach to Three Dimensions

### 4.1 Introduction

In this chapter, a phase-field model for cohesive fracture is used to simulate pervasive cracking in thin films. A new strain energy split is proposed to enforce frictionless contact conditions in the vicinity of diffuse fracture surfaces. In contrast to existing splits that have been proposed, our approach completely prevents tractions from being transmitted across fully damaged surfaces that are loaded in tension. Spatial variations of material properties are incorporated into our model, and we demonstrate, through forward analysis and by solving an inverse problem, how crack network morphology can be influenced by stochastic spatially varying material properties.

To prevent crack growth under compression, phase-field models of fracture typically employ some form of tension-compression asymmetric split in the strain energy. Two popular approaches are the spectral decomposition [134? ] and the volumetric-deviatoric decomposition [135]. Both the spectral decomposition and the

volumetric-deviatoric decomposition are variational and can be fit within the current variational framework. Although these variational approaches represent crack growth reasonably well for a broad range of problems, they do not completely preclude the transmission of tractions across fully damaged surfaces. In part, this is by design. The decompositions are designed to allow compressive tractions to be transmitted across fully damaged surfaces. But since they are developed from the full stress or strain as opposed to the surface tractions, they can also allow unwanted tensile or shear tractions to be transmitted. This can give rise to spurious macro-scale responses in some situations. Strobl and Seelig [136] proposed constitutive relations that satisfy the boundary conditions on diffuse crack surfaces by taking into account the crack orientation. Although the use of such a constitutive model violated the fundamental variational structure of phase-field models, it was shown to yield better results in some fracture problems [137]. A similar approach was presented by Fei and Choo [138, 139] to extend the model to better account for frictional contact conditions at crack surfaces. Finally, we mention the recent work of Lo et al. [140], in which the standard spectral split was modified to better guard against crack growth in compression.

In this chapter, we propose a variational strain energy split that enforces frictionless contact conditions. Importantly, the split effectively prevents the transmission of tractions across fully-damaged surfaces that are loaded in tension. The proposed split leads to a decomposition that is shown to be important in mode II and mixed-mode fracture problems. The new phase-field model is then applied to study the classical problem of the fracture of thin films bonded to thick substrates. Due to the accumulation of inelastic strain and the stiffness mismatch between the film and the substrate, cracks form either transversely through the thickness of the film, referred to as “channeling”, or at the interface, referred to as “debonding”. Film-substrate systems exist across a wide span of application problems, from technological systems such as

nuclear fuel pellet–cladding interactions (PCI) [141, 142, 143, 144, 145] to more common civil infrastructure examples such as pavement asphalts [146, 147, 148, 149, 150]. The study of fracture in these systems is driven by an interest in both understanding the underlying mechanisms and in preventing crack nucleation and evolution. In the current work, we confine attention to transverse channeling cracks in the film. When a system of cracks nucleate, branch and coalesce, complicated crack networks appear in the thin films. Hutchinson and Suo [151] provides a comprehensive review of crack patterns in film-substrate systems.

The fracture of thin films bonded to substrates has been studied using model-based simulations based on a wide range of methodologies. These problems are challenging to simulate because they involve pervasive crack nucleation, branching, and coalescence. Phenomenological spring models were developed and employed by Crosby and Bradley [152], Leung and Néda [153] and Sadhukhan et al. [154]. Zhang et al. [155] applied a cohesive zone method to study the film-substrate interface debonding, and Sánchez et al. [156] proposed a mesh fragmentation technique to simulate three-dimensional crack morphologies. Although such techniques are known to produce mesh-dependent results, the resulting crack networks were found to be satisfactory. Liang et al. [157], Sukumar and Prévost [158] and Huang et al. [159] modeled thin film cracking using the eXtended Finite Element Method (XFEM) which allowed for the cracks to evolve independently of the finite-element mesh.

The aforementioned analytical and numerical efforts have provided a great deal of insight into the factors controlling the fracture of thin films. In particular, the mechanical properties that govern the spacing between cracks have been studied by Hutchinson and Suo [151], Xia and Hutchinson [160] and most recently by Yin et al. [161]. In contrast, the connection between spatial variations in material properties and the morphology of the resulting crack patterns has received fairly little attention. This is despite experimental evidence that crack morphologies are sensitive to

spatial variations in material properties, see, e.g. Kitsunezaki et al. [162, 163], Halász et al. [164], Kitsunezaki et al. [165] and Nakahara et al. [166]. To our knowledge, while some previous model-based simulations of thin-film fracture have incorporated random material properties, they have not specifically considered spatial fluctuations and the construction of proper stochastic models. More broadly, the literature on probabilistic modeling for fracture simulations remains scarce. In [167], variability in fracture strength was estimated from multiscale simulations, and spatially varying mesoscale properties were subsequently integrated into an asynchronous spacetime discontinuous Galerkin finite element based fracture model to study the impact on fragmentation. The integration of apparent elasticity coefficients in a multiscale-informed phase-field formulation was investigated in [168], with the aim of reproducing variability in the macroscopic response. The fracture toughness was modeled as deterministic and homogeneous, and was identified by solving an inverse problem. In [169], a continuum mapping of the meso-scale structure to the packing fraction at the macro-scale was employed to introduce a random component to phase-field simulations of surfactant-induced fracture of particle rafts. In this chapter, we construct a probabilistic model for the critical fracture energy and the fracture toughness, modeled as (potentially correlated) random fields, and examine their influence on the random morphology of the resulting fracture patterns.

Our model-based simulations of thin-film fracture for systems with spatially-variable material properties are facilitated in this work through the adoption of an extension of phase-field models to cohesive fracture [170, 14, 85]. Phase-field models for cohesive fracture incorporate the original proposition by Xia and Hutchinson [160] regarding a “critical fracture energy”. The regularization length is decoupled from the material properties in these approaches, and the critical strength and the fracture toughness of the material are no longer strongly correlated. This independence permits simulations of drying in systems with realistic material properties for typi-

cal clays or soils, for example, without compromising the magnitude of the critical strength or requiring regularization lengths that are larger than the specimen dimensions. It also allows systems with spatially-variable fracture properties to be studied using a spatially-constant regularization length, greatly improving the fidelity of the numerical calculations.

This chapter is organized as follows. Section 4.2 the constitutive choices and stochastic models for fracture properties. In Section 4.3, several numerical examples of benchmark problems in quasi-static fracture mechanics are provided to illustrate the efficacy of the new approach to enforcing frictionless contact conditions. The main results of this work are provided in ??, where the new model is used to study the formation of crack networks in thin films and in soil desiccation problems. In particular, model-based simulations are used to examine how the fragment statistics and fracture morphologies are influenced by spatial variations in the fracture properties. Comparisons with both theory and experimental observations are provided.

## 4.2 Theory

## 4.3 Verification

# Bibliography

- [1] Blaise Bourdin, Chukwudi P Chukwudzie, Keita Yoshioka, et al. A variational approach to the numerical simulation of hydraulic fracturing. In *SPE Annual Technical Conference and Exhibition*. Society of Petroleum Engineers, 2012.
- [2] J Adachi, E Siebrits, A Peirce, and J Desroches. Computer simulation of hydraulic fractures. *International Journal of Rock Mechanics and Mining Sciences*, 44(5):739–757, 2007.
- [3] I. BABUŠKA and J. M. MELENK. The partition of unity method. *International Journal for Numerical Methods in Engineering*, 40(4):727–758, 1997.
- [4] Nicolas Moës, John Dolbow, and Ted Belytschko. A finite element method for crack growth without remeshing. *International Journal for Numerical Methods in Engineering*, 46(1):131–150, 1999. ISSN 1097-0207.
- [5] A. Needleman. Micromechanical modelling of interfacial decohesion. *Ultramicroscopy*, 40:203–214, 1992.
- [6] M. Ortiz and A. Pandolfi. Finite-deformation irreversible cohesive element for three-dimensional crack-propagation analysis. *International Journal for Numerical Methods in Engineering*, 44:1267–1282, 1999.
- [7] Masayuki Kamaya, Yoshihiro Kawamura, and Takayuki Kitamura. Three-dimensional local stress analysis on grain boundaries in polycrystalline material. *International Journal of Solids and Structures*, 44(10):3267 – 3277, 2007. ISSN 0020-7683.
- [8] Masayuki Kamaya and Mitsuhiro Itakura. Simulation for intergranular stress corrosion cracking based on a three-dimensional polycrystalline model. *Engineering Fracture Mechanics*, 76(3):386 – 401, 2009. ISSN 0013-7944.
- [9] G.A. Francfort and J.J. Marigo. Revisiting brittle fracture as an energy minimization problem. *Journal of the Mechanics and Physics of Solids*, 46(8):1319–1342, 1998.

- [10] B. Bourdin, G.A. Francfort, and J.J. Marigo. Numerical experiments in revisited brittle fracture. *Journal of the Mechanics and Physics of Solids*, 48(4):797–826, 2000.
- [11] Blaise Bourdin, Gilles A Francfort, and Jean-Jacques Marigo. The variational approach to fracture. *Journal of elasticity*, 91(1-3):5–148, 2008.
- [12] Kim Pham and Jean-Jacques Marigo. From the onset of damage to rupture: construction of responses with damage localization for a general class of gradient damage models. *Continuum Mechanics and Thermodynamics*, 25(2-4):147–171, 2013.
- [13] Luigi Ambrosio and Vincenzo Maria Tortorelli. Approximation of functional depending on jumps by elliptic functional via t-convergence. *Communications on Pure and Applied Mathematics*, 43(8):999–1036, 1990.
- [14] Jian-Ying Wu. A unified phase-field theory for the mechanics of damage and quasi-brittle failure. *Journal of the Mechanics and Physics of Solids*, 103:72–99, 2017.
- [15] A. Karma, D. A. Kessler, and H. Levine. Phase-field model of mode III dynamic fracture. *Physical Review Letters*, 87(4):045501–1–4, 2001.
- [16] A. Karma and A. E. Lobkovsky. Unsteady crack motion and branching in a phase-field model of brittle fracture. *Physical Review Letters*, 93(10):245510, 2004.
- [17] H. Henry and H. Levine. Dynamic instabilities of fracture under biaxial strain using a phase field model. *Physical Review Letters*, 93(10):105504, 2004.
- [18] R. Spatschek, C. M. Guganberger, and E. Brener. Phase field modeling of fracture and stress-induced phase transitions. *Physical Review E*, 75:066111, 2007.
- [19] H. Amor, J. J. Marigo, and C. Maurini. Regularized formulation of the variational brittle fracture with unilateral contact: Numerical experiments. *Journal of the Mechanics and Physics of Solids*, 57(8):1209–1229, 2009.
- [20] Maurice Anthony Biot. Thermoelasticity and irreversible thermodynamics. *Journal of applied physics*, 27(3):240–253, 1956.
- [21] George Herrmann. On variational principles in thermoelasticity and heat conduction. *Quarterly of Applied Mathematics*, 21(2):151–155, 1963.
- [22] M Ben-Amoz. On a variational theorem in coupled thermoelasticity. 1965.

- [23] John Tinsley Oden and Junuthula Narasimha Reddy. *Variational methods in theoretical mechanics*. Springer Science Business Media, 2012.
- [24] A Molinari and M Ortiz. Global viscoelastic behavior of heterogeneous thermoelastic materials. *International journal of solids and structures*, 23(9):1285–1300, 1987.
- [25] Gautam Batra. On a principle of virtual work for thermo-elastic bodies. *Journal of elasticity*, 21(2):131–146, 1989.
- [26] Seishiro Matsubara and Kenjiro Terada. A variationally consistent formulation of the thermo-mechanically coupled problem with non-associative viscoplasticity for glassy amorphous polymers. *International Journal of Solids and Structures*, 212:152–168, 2021.
- [27] Qiang Yang, Laurent Stainier, and Michael Ortiz. A variational formulation of the coupled thermo-mechanical boundary-value problem for general dissipative solids. *Journal of the Mechanics and Physics of Solids*, 54(2):401–424, 2006.
- [28] Gianni Dal Maso. *An introduction to  $\Gamma$ -convergence*, volume 8. Springer Science Business Media, 2012.
- [29] Andrea Braides et al. *Approximation of free-discontinuity problems*. Number 1694. Springer Science & Business Media, 1998.
- [30] Ronald F Gariepy. Functions of bounded variation and free discontinuity problems (oxford mathematical monographs) by luigi ambrosio, nicolo fucso and diego pallara: 434 pp., £ 55.00, isbn 0-19-850254-1 (clarendon press, oxford, 2000). *Bulletin of the London Mathematical Society*, 33(4):492–512, 2001.
- [31] Satish Balay, Shrirang Abhyankar, Mark F. Adams, Jed Brown, Peter Brune, Kris Buschelman, Lisandro Dalcin, Alp Dener, Victor Eijkhout, William D. Gropp, Dmitry Karpeyev, Dinesh Kaushik, Matthew G. Knepley, Dave A. May, Lois Curfman McInnes, Richard Tran Mills, Todd Munson, Karl Rupp, Patrick Sanan, Barry F. Smith, Stefano Zampini, Hong Zhang, and Hong Zhang. PETSc Web page. <https://www.mcs.anl.gov/petsc>, 2019. URL <https://www.mcs.anl.gov/petsc>.
- [32] Steve Benson, Lois Curfman McInnes, Jorge J More, and Jason Sarich. Tao users manual. Technical report, Argonne National Lab., IL (US), 2003.
- [33] Michael A Heroux, Roscoe A Bartlett, Vicki E Howle, Robert J Hoekstra, Jonathan J Hu, Tamara G Kolda, Richard B Lehoucq, Kevin R Long, Roger P Pawłowski, Eric T Phipps, et al. An overview of the trilinos project. *ACM Transactions on Mathematical Software (TOMS)*, 31(3):397–423, 2005.
- [34] Desmond J Higham and Nicholas J Higham. *MATLAB guide*. SIAM, 2016.

- [35] Quanshu Li, Huilin Xing, Jianjun Liu, and Xiangchon Liu. A review on hydraulic fracturing of unconventional reservoir. *Petroleum*, 1(1):8–15, 2015.
- [36] R Mair, M Bickle, D Goodman, B Koppelman, J Roberts, R Selley, Z Shipton, H Thomas, A Walker, E Woods, et al. Shale gas extraction in the UK: a review of hydraulic fracturing. *technical report*, 2012.
- [37] Akira Shinmura and Victor E Saouma. Fluid fracture interaction in pressurized reinforced concrete vessels. *Materials and Structures*, 30(2):72–80, 1997.
- [38] Yang Wang and Jinsheng Jia. Experimental study on the influence of hydraulic fracturing on high concrete gravity dams. *Engineering Structures*, 132:508–517, 2017.
- [39] Nathan Capps, Colby Jensen, Fabiola Cappia, Jason Harp, Kurt Terrani, Nicolas Woolstenhulme, and Daniel Wachs. A critical review of high burnup fuel fragmentation, relocation, and dispersal under loss-of-coolant accident conditions. *Journal of Nuclear Materials*, 546:152750, 2021.
- [40] JA Turnbull, SK Yagnik, M Hirai, DM Staicu, and CT Walker. An assessment of the fuel pulverization threshold during LOCA-type temperature transients. *Nuclear Science and Engineering*, 179(4):477–485, 2015.
- [41] Blaise Bourdin, Gilles A Francfort, and Jean-Jacques Marigo. Numerical experiments in revisited brittle fracture. *Journal of the Mechanics and Physics of Solids*, 48(4):797–826, 2000.
- [42] Mary F Wheeler, Thomas Wick, and W Wollner. An augmented-lagrangian method for the phase-field approach for pressurized fractures. *Computer Methods in Applied Mechanics and Engineering*, 271:69–85, 2014.
- [43] Andro Mikelić, Mary F Wheeler, and Thomas Wick. A quasi-static phase-field approach to pressurized fractures. *Nonlinearity*, 28(5):1371, 2015.
- [44] Christian Peco, Wei Chen, Yingjie Liu, MM Bandi, John E Dolbow, and Eliot Fried. Influence of surface tension in the surfactant-driven fracture of closely-packed particulate monolayers. *Soft Matter*, 13(35):5832–5841, 2017.
- [45] Wen Jiang, Tianchen Hu, Larry K Aagesen, Sudipta Biswas, and Kyle A Gamble. A phase-field model of quasi-brittle fracture for pressurized cracks: Application to UO<sub>2</sub> high-burnup microstructure fragmentation. *Theoretical and Applied Fracture Mechanics*, 119:103348, 2022.
- [46] Tianchen Hu. *A Variational Framework for Phase-Field Fracture Modeling with Applications to Fragmentation, Desiccation, Ductile Failure, and Spallation*. PhD thesis, Duke University, 2021.

- [47] Alain Karma, David A Kessler, and Herbert Levine. Phase-field model of mode iii dynamic fracture. *Physical Review Letters*, 87(4):045501, 2001.
- [48] Gilles A Francfort and J-J Marigo. Revisiting brittle fracture as an energy minimization problem. *Journal of the Mechanics and Physics of Solids*, 46(8):1319–1342, 1998.
- [49] Roberto Alessi, Jean-Jacques Marigo, and Stefano Vidoli. Gradient damage models coupled with plasticity and nucleation of cohesive cracks. *Archive for Rational Mechanics and Analysis*, 214(2):575–615, 2014.
- [50] Marreddy Ambati, Tymofiy Gerasimov, and Laura De Lorenzis. Phase-field modeling of ductile fracture. *Computational Mechanics*, 55(5):1017–1040, 2015.
- [51] Christian Miehe and Steffen Mauthe. Phase field modeling of fracture in multi-physics problems. part iii. crack driving forces in hydro-poro-elasticity and hydraulic fracturing of fluid-saturated porous media. *Computer Methods in Applied Mechanics and Engineering*, 304:619–655, 2016.
- [52] Michael J Borden, Thomas JR Hughes, Chad M Landis, Amin Anvari, and Isaac J Lee. A phase-field formulation for fracture in ductile materials: Finite deformation balance law derivation, plastic degradation, and stress triaxiality effects. *Computer Methods in Applied Mechanics and Engineering*, 312:130–166, 2016.
- [53] Tianchen Hu, Brandon Talamini, Andrew J Stershic, Michael R Tupek, and John E Dolbow. A variational phase-field model for ductile fracture with coalescence dissipation. *Computational Mechanics*, 68(2):311–335, 2021.
- [54] Zachary A Wilson and Chad M Landis. Phase-field modeling of hydraulic fracture. *Journal of the Mechanics and Physics of Solids*, 96:264–290, 2016.
- [55] Chukwudi Chukwudozie, Blaise Bourdin, and Keita Yoshioka. A variational phase-field model for hydraulic fracturing in porous media. *Computer Methods in Applied Mechanics and Engineering*, 347:957–982, 2019.
- [56] A Mikelić, Mary F Wheeler, and Thomas Wick. Phase-field modeling of a fluid-driven fracture in a poroelastic medium. *Computational Geosciences*, 19(6):1171–1195, 2015.
- [57] David Santillán, Ruben Juanes, and Luis Cueto-Felgueroso. Phase field model of hydraulic fracturing in poroelastic media: Fracture propagation, arrest, and branching under fluid injection and extraction. *Journal of Geophysical Research: Solid Earth*, 123(3):2127–2155, 2018.

- [58] Corrado Maurini, B Bourdin, G Gauthier, and Veronique Lazarus. Crack patterns obtained by unidirectional drying of a colloidal suspension in a capillary tube: experiments and numerical simulations using a two-dimensional variational approach. *International Journal of Fracture*, 184(1-2):75–91, 2013.
- [59] Yousef Heider and WaiChing Sun. A phase field framework for capillary-induced fracture in unsaturated porous media: Drying-induced vs. hydraulic cracking. *Computer Methods in Applied Mechanics and Engineering*, 359: 112647, 2020.
- [60] Tuanny Cajuhi, Lorenzo Sanavia, and Laura De Lorenzis. Phase-field modeling of fracture in variably saturated porous media. *Computational Mechanics*, 61 (3):299–318, 2018.
- [61] Hu Tianchen, Johann Guilleminot, and John Dolbow. A phase-field model of fracture with frictionless contact and random fracture properties: Application to thin-film fracture and soil desiccation. *Computer Methods in Applied Mechanics and Engineering*, 368, 2020.
- [62] Blaise Bourdin, Christopher J Larsen, and Casey L Richardson. A time-discrete model for dynamic fracture based on crack regularization. *International Journal of Fracture*, 168(2):133–143, 2011.
- [63] Michael J Borden, Clemens V Verhoosel, Michael A Scott, Thomas JR Hughes, and Chad M Landis. A phase-field description of dynamic brittle fracture. *Computer Methods in Applied Mechanics and Engineering*, 217:77–95, 2012.
- [64] M Hofacker and C30082661352 Miehe. A phase field model of dynamic fracture: Robust field updates for the analysis of complex crack patterns. *International Journal for Numerical Methods in Engineering*, 93(3):276–301, 2013.
- [65] Alexander Schlüter, Adrian Willenbücher, Charlotte Kuhn, and Ralf Müller. Phase field approximation of dynamic brittle fracture. *Computational Mechanics*, 54(5):1141–1161, 2014.
- [66] Tianyi Li, Jean-Jacques Marigo, Daniel Guilbaud, and Serguei Potapov. Gradient damage modeling of brittle fracture in an explicit dynamics context. *International Journal for Numerical Methods in Engineering*, 108(11):1381–1405, 2016.
- [67] David Kamensky, Georgios Moutsanidis, and Yuri Bazilevs. Hyperbolic phase field modeling of brittle fracture: Part i—theory and simulations. *Journal of the Mechanics and Physics of Solids*, 121:81–98, 2018.

- [68] Georgios Moutsanidis, David Kamensky, JS Chen, and Yuri Bazilevs. Hyperbolic phase field modeling of brittle fracture: Part ii—immersed iga–rkpm coupling for air-blast–structure interaction. *Journal of the Mechanics and Physics of Solids*, 121:114–132, 2018.
- [69] Chi Wu, Jianguang Fang, Zhongpu Zhang, Ali Entezari, Guangyong Sun, Michael V Swain, and Qing Li. Fracture modeling of brittle biomaterials by the phase-field method. *Engineering Fracture Mechanics*, 224:106752, 2020.
- [70] Arun Raina and Christian Miehe. A phase-field model for fracture in biological tissues. *Biomechanics and modeling in mechanobiology*, 15(3):479–496, 2016.
- [71] Sindhu Nagaraja, Kay Leichsenring, Marreddy Ambati, Laura De Lorenzis, and Markus Böhl. On a phase-field approach to model fracture of small intestine walls. *Acta Biomaterialia*, 130:317–331, 2021.
- [72] Osman Güttekin, Hüsnü Dal, and Gerhard A Holzapfel. A phase-field approach to model fracture of arterial walls: theory and finite element analysis. *Computer Methods in Applied Mechanics and Engineering*, 312:542–566, 2016.
- [73] Osman Güttekin, Hüsnü Dal, and Gerhard A Holzapfel. Numerical aspects of anisotropic failure in soft biological tissues favor energy-based criteria: A rate-dependent anisotropic crack phase-field model. *Computer Methods in Applied Mechanics and Engineering*, 331:23–52, 2018.
- [74] Marreddy Ambati, Tymofiy Gerasimov, and Laura De Lorenzis. A review on phase-field models of brittle fracture and a new fast hybrid formulation. *Computational Mechanics*, 55(2):383–405, 2015.
- [75] Jian-Ying Wu, Vinh Phu Nguyen, Chi Thanh Nguyen, Danas Sutula, Sina Sinaie, and Stéphane PA Bordas. Phase-field modeling of fracture. In *Advances in Applied Mechanics*, volume 53, pages 1–183. Elsevier, 2020.
- [76] GA Francfort. Variational fracture: twenty years after. *International Journal of Fracture*, pages 1–11, 2021.
- [77] Erwan Tanné, Blaise Bourdin, and Keita Yoshioka. On the loss of symmetry in toughness dominated hydraulic fractures. *International Journal of Fracture*, 237(1-2):189–202, 2022.
- [78] Patrick Zulian, Alena Kopaničáková, Maria Giuseppina Chiara Nestola, Andreas Fink, Nur Aiman Fadel, Joost VandeVondele, and Rolf Krause. Large scale simulation of pressure induced phase-field fracture propagation using utopia. *CCF transactions on high performance computing*, 3(4):407–426, 2021.

- [79] Keita Yoshioka, Francesco Parisio, Dmitri Naumov, Renchao Lu, Olaf Kolditz, and Thomas Nagel. Comparative verification of discrete and smeared numerical approaches for the simulation of hydraulic fracturing. *GEM-International Journal on Geomathematics*, 10(1):13, 2019.
- [80] Keita Yoshioka, Dmitri Naumov, and Olaf Kolditz. On crack opening computation in variational phase-field models for fracture. *Computer Methods in Applied Mechanics and Engineering*, 369:113210, 2020.
- [81] Y Heider and B Markert. A phase-field modeling approach of hydraulic fracture in saturated porous media. *Mechanics Research Communications*, 80:38–46, 2017.
- [82] Hui Li, Hongwu Lei, Zhenjun Yang, Jianying Wu, Xiaoxian Zhang, and Shouding Li. A hydro-mechanical-damage fully coupled cohesive phase field model for complicated fracking simulations in poroelastic media. *Computer Methods in Applied Mechanics and Engineering*, 399:115451, 2022.
- [83] Yousef Heider. A review on phase-field modeling of hydraulic fracturing. *Engineering Fracture Mechanics*, 253:107881, 2021.
- [84] Eric Lorentz, Sam Cuvilliez, and Kyrylo Kazymyrenko. Convergence of a gradient damage model toward a cohesive zone model. *Comptes Rendus Mécanique*, 339(1):20–26, 2011.
- [85] Rudy JM Geelen, Yingjie Liu, Tianchen Hu, Michael R Tupek, and John E Dolbow. A phase-field formulation for dynamic cohesive fracture. *Computer Methods in Applied Mechanics and Engineering*, 348:680–711, 2019.
- [86] Paul Sicsic and Jean-Jacques Marigo. From gradient damage laws to griffith’s theory of crack propagation. *Journal of Elasticity*, 113(1):55–74, 2013.
- [87] Roberto Ballarini and Gianni Royer-Carfagni. Closed-path j-integral analysis of bridged and phase-field cracks. *Journal of Applied Mechanics*, 83(6), 2016.
- [88] MZ Hossain, C-J Hsueh, B Bourdin, and K Bhattacharya. Effective toughness of heterogeneous media. *Journal of the Mechanics and Physics of Solids*, 71:15–32, 2014.
- [89] Fang Zhong Li, C Fong Shih, and A Needleman. A comparison of methods for calculating energy release rates. *Engineering Fracture Mechanics*, 21(2):405–421, 1985.
- [90] CF Shih, B Moran, and T Nakamura. Energy release rate along a three-dimensional crack front in a thermally stressed body. *International Journal of Fracture*, 30(2):79–102, 1986.

- [91] Hanen Amor, Jean-Jacques Marigo, and Corrado Maurini. Regularized formulation of the variational brittle fracture with unilateral contact: Numerical experiments. *Journal of the Mechanics and Physics of Solids*, 57(8):1209–1229, 2009.
- [92] Christian Miehe, Martina Hofacker, and Fabian Welschinger. A phase field model for rate-independent crack propagation: Robust algorithmic implementation based on operator splits. *Computer Methods in Applied Mechanics and Engineering*, 199(45-48):2765–2778, 2010.
- [93] Emmanuel Detournay. Mechanics of hydraulic fractures. *Annual Review of Fluid Mechanics*, 48:311–339, 2016.
- [94] D Garagash and E Detournay. The tip region of a fluid-driven fracture in an elastic medium. *Journal of Applied Mechanics*, 67(1):183–192, 2000.
- [95] Emmanuel Detournay. Propagation regimes of fluid-driven fractures in impermeable rocks. *International Journal of Geomechanics*, 4(1):35–45, 2004.
- [96] Dmitry I Garagash and Emmanuel Detournay. Plane-strain propagation of a fluid-driven fracture: small toughness solution. *Journal of Applied Mechanics*, 72(6):916–928, 2005.
- [97] Andrew P Bunger, Emmanuel Detournay, and Dmitry I Garagash. Toughness-dominated hydraulic fracture with leak-off. *International Journal of Fracture*, 134(2):175–190, 2005.
- [98] Wen Jiang, Tianchen Hu, Larry K Aagesen, and Yongfeng Zhang. Three-dimensional phase-field modeling of porosity dependent intergranular fracture in UO<sub>2</sub>. *Computational Materials Science*, 171:109269, 2020.
- [99] Eric Lorentz and V Godard. Gradient damage models: Toward full-scale computations. *Computer Methods in Applied Mechanics and Engineering*, 200(21-22):1927–1944, 2011.
- [100] James R Rice et al. Mathematical analysis in the mechanics of fracture. *Fracture: an advanced treatise*, 2:191–311, 1968.
- [101] James R Rice. A path independent integral and the approximate analysis of strain concentration by notches and cracks. *Journal of Applied Mechanics*, 35 (2):379–386, 1968.
- [102] A. Karlsson and J. Backlund. J-integral at loaded crack surfaces. *International Journal of Fracture*, 14:311–318, 1978.
- [103] W. Karush. Minima of functions of several variables with inequalities as side constraints. *M. Sc. Dissertation. Dept. of Mathematics, Univ. of Chicago*, 1939.

- [104] H. W. Kuhn and A. W. Tucker. Nonlinear Programming. In *Proceedings of the Second Berkeley Symposium on Mathematical Statistics and Probability*, pages 481–492. University of California Press, 1951.
- [105] Timo Heister, Mary F Wheeler, and Thomas Wick. A primal-dual active set method and predictor-corrector mesh adaptivity for computing fracture propagation using a phase-field approach. *Computer Methods in Applied Mechanics and Engineering*, 290:466–495, 2015.
- [106] Tianchen Hu, Johann Guilleminot, and John E Dolbow. A phase-field model of fracture with frictionless contact and random fracture properties: Application to thin-film fracture and soil desiccation. *Computer Methods in Applied Mechanics and Engineering*, 368:113106, 2020.
- [107] Tianchen Hu. RACCOON - a parallel finite-element code specialized in phase-field for fracture, 2020. URL <https://hugary1995.github.io/raccoon/index.html>.
- [108] Derek Gaston, Chris Newman, Glen Hansen, and Damien Lebrun-Grandie. Moose: A parallel computational framework for coupled systems of nonlinear equations. *Nuclear Engineering and Design*, 239(10):1768–1778, 2009.
- [109] Cody J Permann, Derek R Gaston, David Andrš, Robert W Carlsen, Fande Kong, Alexander D Lindsay, Jason M Miller, John W Peterson, Andrew E Slaughter, Roy H Stogner, et al. Moose: Enabling massively parallel multi-physics simulation. *SoftwareX*, 11:100430, 2020.
- [110] Alexander D Lindsay, Derek R Gaston, Cody J Permann, Jason M Miller, David Andrš, Andrew E Slaughter, Fande Kong, Joshua Hansel, Robert W Carlsen, Casey Icenhour, et al. 2.0-moose: Enabling massively parallel multi-physics simulation. *SoftwareX*, 20:101202, 2022.
- [111] Ferdinand Stoeckhert, Michael Molenda, Sebastian Brenne, and Michael Alber. Fracture propagation in sandstone and slate—laboratory experiments, acoustic emissions and fracture mechanics. *Journal of Rock Mechanics and Geotechnical Engineering*, 7(3):237–249, 2015.
- [112] G. R. Irwin. Analysis of Stresses and Strains Near the End of a Crack Traversing a Plate. *Journal of Applied Mechanics*, 24(3):361–364, 1957.
- [113] R. Fosdick and L. Truskinovsky. About Clapeyron’s Theorem in Linear Elasticity. *Journal of Elasticity*, 72:145–172, 2003.
- [114] Zdenek P Bazant and Jaime Planas. *Fracture and size effect in concrete and other quasibrittle materials*. Routledge, 2019.

- [115] Brice Lecampion, Andrew Bunger, and Xi Zhang. Numerical methods for hydraulic fracture propagation: a review of recent trends. *Journal of Natural Gas Science and Engineering*, 49:66–83, 2018.
- [116] Randolph R Settgast, Pengcheng Fu, Stuart DC Walsh, Joshua A White, Chandrasekhar Annavarapu, and Frederick J Ryerson. A fully coupled method for massively parallel simulation of hydraulically driven fractures in 3-dimensions. *International Journal for Numerical and Analytical Methods in Geomechanics*, 41(5):627–653, 2017.
- [117] P Gupta and Carlos Armando Duarte. Simulation of non-planar three-dimensional hydraulic fracture propagation. *International Journal for Numerical and Analytical Methods in Geomechanics*, 38(13):1397–1430, 2014.
- [118] P Gupta and Carlos Armando Duarte. Coupled hydromechanical-fracture simulations of nonplanar three-dimensional hydraulic fracture propagation. *International Journal for Numerical and Analytical Methods in Geomechanics*, 42(1):143–180, 2018.
- [119] Christian Miehe, Steffen Mauthe, and Stephan Teichtmeister. Minimization principles for the coupled problem of darcy–biot-type fluid transport in porous media linked to phase field modeling of fracture. *Journal of the Mechanics and Physics of Solids*, 82:186–217, 2015.
- [120] Andro Mikelic, Mary F Wheeler, and Thomas Wick. A phase-field method for propagating fluid-filled fractures coupled to a surrounding porous medium. *Multiscale Modeling & Simulation*, 13(1):367–398, 2015.
- [121] Rudy JM Geelen, Yingjie Liu, John E Dolbow, and Antonio Rodríguez-Ferran. An optimization-based phase-field method for continuous-discontinuous crack propagation. *International Journal for Numerical Methods in Engineering*, 116(1):1–20, 2018.
- [122] Bianca Giovanardi, Anna Scotti, and Luca Formaggia. A hybrid xfem–phase field (xfield) method for crack propagation in brittle elastic materials. *Computer Methods in Applied Mechanics and Engineering*, 320:396–420, 2017.
- [123] Alba Muixí, Onofre Marco, Antonio Rodríguez-Ferran, and Sonia Fernández-Méndez. A combined xfem phase-field computational model for crack growth without remeshing. *Computational Mechanics*, 67(1):231–249, 2021.
- [124] Nicolas Moës, John Dolbow, and Ted Belytschko. A finite element method for crack growth without remeshing. *International Journal for Numerical Methods in Engineering*, 46(1):131–150, 1999.

- [125] Yuan Sun, Zhiyuan Liu, and Xuhai Tang. A hybrid femm-phase field method for fluid-driven fracture propagation in three dimension. *Engineering Analysis with Boundary Elements*, 113:40–54, 2020.
- [126] Matteo Cusini, Joshua A White, Nicola Castelletto, and Randolph R Settgast. Simulation of coupled multiphase flow and geomechanics in porous media with embedded discrete fractures. *International Journal for Numerical and Analytical Methods in Geomechanics*, 45(5):563–584, 2021.
- [127] J Geertsma and F De Klerk. A rapid method of predicting width and extent of hydraulically induced fractures. *Journal of Petroleum Technology*, 21(12):1571–1581, 1969.
- [128] A Khristianovic Zheltov. 3. formation of vertical fractures by means of highly viscous liquid. In *4th World Petroleum Congress*. OnePetro, 1955.
- [129] Hadi Hajibeygi, Dimitris Karvounis, and Patrick Jenny. A hierarchical fracture model for the iterative multiscale finite volume method. *Journal of Computational Physics*, 230(24):8729–8743, 2011.
- [130] Maurice A Biot. General theory of three-dimensional consolidation. *Journal of Applied Physics*, 12(2):155–164, 1941.
- [131] Alan Arnold Griffith. Vi. the phenomena of rupture and flow in solids. *Philosophical Transactions of the Royal Society of London. Series A*, 221(582-593):163–198, 1921.
- [132] Christian Linder and Francisco Armero. Finite elements with embedded strong discontinuities for the modeling of failure in solids. *International Journal for Numerical Methods in Engineering*, 72(12):1391–1433, 2007.
- [133] Seong H Lee, MF Lough, and CL Jensen. Hierarchical modeling of flow in naturally fractured formations with multiple length scales. *Water Resources Research*, 37(3):443–455, 2001.
- [134] C. Miehe, F. Welschinger, and M. Hofacker. Thermodynamically consistent phase-field models of fracture: Variational principles and multi-field FE implementations. *International Journal for Numerical Methods in Engineering*, 83:1273–1311, 2010.
- [135] Hanen Amor, Jean-Jacques Marigo, and Corrado Maurini. Regularized formulation of the variational brittle fracture with unilateral contact: Numerical experiments. *Journal of the Mechanics and Physics of Solids*, 57(8):1209 – 1229, 2009. ISSN 0022-5096.
- [136] Michael Strobl and Thomas Seelig. A novel treatment of crack boundary conditions in phase field models of fracture. *Pamm*, 15(1):155–156, 2015.

- [137] Michael Strobl and Thomas Seelig. On constitutive assumptions in phase field approaches to brittle fracture. *Procedia Structural Integrity*, 2:3705–3712, 2016.
- [138] Fan Fei and Jinyun Choo. A phase-field method for modeling cracks with frictional contact. *arXiv preprint arXiv:1905.10547*, 2019.
- [139] Fan Fei and Jinyun Choo. A phase-field model of geologic shear fracture, 2020.
- [140] Yu-Sheng Lo, Michael Borden, K. Ravi-Chandar, and Chad M. Landis. A phase-field model for fatigue crack growth. *Journal of the Mechanics and Physics of Solids*, 132(103684), 2019.
- [141] JTA Roberts, E Smith, N Fuhrman, and D Cubicciotti. On the pellet-cladding interaction phenomenon. *Nuclear Technology*, 35(1):131–144, 1977.
- [142] Bruno Michel, Jérôme Sercombe, Gilles Thouvenin, and Rémy Chatelet. 3d fuel cracking modelling in pellet cladding mechanical interaction. *Engineering fracture mechanics*, 75(11):3581–3598, 2008.
- [143] Lars Olof Jernkvist. A model for predicting pellet-cladding interaction-induced fuel rod failure. *Nuclear engineering and design*, 156(3):393–399, 1995.
- [144] Fumihsisa Nagase and Toyoshi Fuketa. Effect of pre-hydriding on thermal shock resistance of zircaloy-4 cladding under simulated loss-of-coolant accident conditions. *Journal of nuclear science and technology*, 41(7):723–730, 2004.
- [145] Michael Billone, Yong Yan, Tatiana Burtseva, Robert Daum, et al. Cladding embrittlement during postulated loss-of-coolant accidents. Technical report, Argonne National Lab.(ANL), Argonne, IL (United States), 2008.
- [146] Mohamed M El-Basyouny and Matthew Witczak. Calibration of alligator fatigue cracking model for 2002 design guide. *Transportation research record*, 1919(1):76–86, 2005.
- [147] Sherif M El-Badawy, Myung Goo Jeong, and Mohamed El-Basyouny. Methodology to predict alligator fatigue cracking distress based on asphalt concrete dynamic modulus. *Transportation Research Record*, 2095(1):115–124, 2009.
- [148] T Saar and O Talvik. Automatic asphalt pavement crack detection and classification using neural networks. In *2010 12th Biennial Baltic Electronics Conference*, pages 345–348. IEEE, 2010.
- [149] Joe W Button and Robert L Lytton. Guidelines for using geosynthetics with hot-mix asphalt overlays to reduce reflective cracking. *Transportation Research Record*, 2004(1):111–119, 2007.

- [150] Yetkin Yildirim, Ahmed Qatan, Jorge Prozzi, et al. *Field manual for crack sealing in asphalt pavements.*, 2006.
- [151] John W Hutchinson and Zhigang Suo. Mixed mode cracking in layered materials. In *Advances in applied mechanics*, volume 29, pages 63–191. Elsevier, 1991.
- [152] Kevin M Crosby and R Mark Bradley. Fragmentation of thin films bonded to solid substrates: Simulations and a mean-field theory. *Physical Review E*, 55(5):6084, 1997.
- [153] Kwan-tai Leung and Zoltan Néda. Pattern formation and selection in quasistatic fracture. *Physical review letters*, 85(3):662, 2000.
- [154] Supti Sadhukhan, Tapati Dutta, and Sujata Tarafdar. Crack formation in composites through a spring model. *Physica A: Statistical Mechanics and its Applications*, 390(4):731–740, 2011.
- [155] Jingwen Zhang, Yuyang Lu, Linghui He, Lizhong Yang, and Yong Ni. Modeling progressive interfacial debonding of a mud-crack film on elastic substrates. *Engineering Fracture Mechanics*, 177:123–132, 2017.
- [156] Marcelo Sánchez, Osvaldo L Manzoli, and Leonardo JN Guimar˜aes. Modeling 3-d desiccation soil crack networks using a mesh fragmentation technique. *Computers and Geotechnics*, 62:27–39, 2014.
- [157] J Liang, R Huang, Jean-Herve Prevost, and Z Suo. Evolving crack patterns in thin films with the extended finite element method. *International Journal of Solids and Structures*, 40(10):2343–2354, 2003.
- [158] N Sukumar and J-H Prévost. Modeling quasi-static crack growth with the extended finite element method part i: Computer implementation. *International journal of solids and structures*, 40(26):7513–7537, 2003.
- [159] Rui Huang, N Sukumar, and J-H Prévost. Modeling quasi-static crack growth with the extended finite element method part ii: Numerical applications. *International Journal of Solids and Structures*, 40(26):7539–7552, 2003.
- [160] Z Cedric Xia and John W Hutchinson. Crack patterns in thin films. *Journal of the Mechanics and Physics of Solids*, 48(6-7):1107–1131, 2000.
- [161] HM Yin, GH Paulino, and William G Buttlar. An explicit elastic solution for a brittle film with periodic cracks. *International Journal of Fracture*, 153(1):39, 2008.

- [162] So Kitsunezaki, Akio Nakahara, and Yousuke Matsuo. Shaking-induced stress anisotropy in the memory effect of paste. *EPL (Europhysics Letters)*, 114(6):64002, 2016.
- [163] So Kitsunezaki, Yousuke Matsuo, and Akio Nakahara. Stress development up to crack formation in drying paste. *Journal of Chemical Engineering of Japan*, 50(10):775–779, 2017.
- [164] Zoltán Halász, Akio Nakahara, So Kitsunezaki, and Ferenc Kun. Effect of disorder on shrinkage-induced fragmentation of a thin brittle layer. *Physical Review E*, 96(3):033006, 2017.
- [165] So Kitsunezaki, Arina Sasaki, Akihiro Nishimoto, Tsuyoshi Mizuguchi, Yousuke Matsuo, and Akio Nakahara. Memory effect and anisotropy of particle arrangements in granular paste. *The European Physical Journal E*, 40(10):88, 2017.
- [166] Akio Nakahara, Tomoki Hiraoka, Rokuya Hayashi, Yousuke Matsuo, and So Kitsunezaki. Mechanism of memory effect of paste which dominates desiccation crack patterns. *Philosophical Transactions of the Royal Society A*, 377(2136):20170395, 2018.
- [167] Katherine A. Acton, Sarah C. Baxter, Bahador Bahmani, Philip L. Clarke, and Reza Abedi. Voronoi tessellation based statistical volume element characterization for use in fracture modeling. *Computer Methods in Applied Mechanics and Engineering*, 336:135 – 155, 2018.
- [168] Darith-Anthony Hun, Johann Guilleminot, Julien Yvonnet, and Michel Bornert. Stochastic multiscale modeling of crack propagation in random heterogeneous media. *International Journal for Numerical Methods in Engineering*, 119(13):1325–1344, 2019.
- [169] C. Peco, Y. Liu, C. Rhea, and J.E. Dolbow. Models and simulations of surfactant-driven fracture in particle rafts. *International Journal of Solids and Structures*, 156:194–209, 2019.
- [170] Jian-Ying Wu and Miguel Cervera. A thermodynamically consistent plastic-damage framework for localized failure in quasi-brittle solids: Material model and strain localization analysis. *International Journal of Solids and Structures*, 88:227–247, 2016.

# Biography

Andre Costa earned his B.S. degree in Mechanical Engineering from Universidade Federal de Minas Gerais. He joined the Department of Mechanical Engineering and Materials Science at Duke University in 2018 as a graduate research assistant. He received his Ph.D. degree in 2023. He will be working as something somewhere.